LIBRARY
Michigan State
University

PLACE IN RETURN BOX to remove this checkout from your record.
TO AVOID FINES return on or before date due.

DATE DUE	DATE DUE	DATE DUE
5 87 JUN 1 2 1992		

MSU Is An Affirmative Action/Equal Opportunity Institution
c:\circ\datedue.pm3-p.1

IDENTIFICATION OF MATERIAL CHARACTERISTICS OF LAYERED STRUCTURES BY ULTRASONIC INTERROGATION

By

Chih-Yeh King

A DISSERTATION

Submitted to
Michigan State University
in partial fulfillment of the requirements
for the degree of

DOCTOR OF PHILOSOPHY

Department of Electrical Engineering

1993

ABSTRACT

IDENTIFICATION OF MATERIAL CHARACTERISTICS OF LAYERED STRUCTURES BY ULTRASONIC INTERROGATION

By

Chih-Yeh King

In this research, the theory and approximations of scattered fields are studied, and mode retraction techniques that can be applied to improve the accuracy of ultrasonic identification with the reflection waveform are developed. Since conventional interrogating algorithms are not valid when dealing with a thin layer, more sophisticated algorithms are needed.

First, a wave transmission matrix uses a linearized version of the wave propagation equation and gives an especially simple reconstruction algorithm. This research reviews inverse problem methodology as applied to the backward scattering field, and investigates the quality of the reconstructions when the assumptions behind these approaches are violated. The experimental results show that the evaluation procedures, using a spectral Prony method, are valid only when the wave number is linearly dependent on the frequency, and that the specified band-pass spectrum is valid when the incident wave is excited by a Gaussian-pulse shaped acoustic plane wave.

Better identification is based on a higher mode assumption about the reflection waveform. The advantage of this research is that the information obtained is based solely on the echo return from the successive acoustic interfaces without using the signature of the incident wave which is difficult to capture experimentally. An additional feature of this research is that the results can be used to determine more than one material characteristic from a single trace of reflection waveform.

ACKNOWLEDGEMENTS

Foremost thanks are due Dr. Bong Ho, my academic adviser, for his guidance throughout this work. Gratitude must also be expressed to Dr. H. Roland Zapp, Dr. John R. Deller and Dr. David Yen, for their sincere interest and encouraging advice.

Furthermore, I must thank my wife, Wan - Li Ding, for her support and taking care of my parents and our children during these years of my graduate study.

TABLE OF CONTENTS

LIST OF TABLES

LIST OF FIGURES

CHAPTER 1

INTRODUCTION

The word *interrogation* generally refers to a type of verbal questioning. In physics, ultrasonic interrogation refers to a procedure used to collect data about the internal structure of an object and to then mathematically generate an image of some otherwise hidden properties of the object.

Identification, on the other hand, extracts material properties from the echo return which consists of incident pulse convolved with the transfer function of the object being investigated. Conventionally, only a single feature such as the interface reflection coefficient, acoustic impedance, attenuation constant, or velocity of propagation is used for material discrimination. For a more complex structure, however, it is desirable to utilize as many features as possible so that a higher precision of identification can be achieved. Thus we require more sophisticated techniques than the one used for traditional identification. These new techniques for advanced identification are the subject of this work.

Techniques for the estimation of reflection coefficients at different interfaces have typically involved the manipulation of the echo amplitude in the time domain [1 - 2]. Spectral analyses are commonly used for the estimation of attenuation properties of materials [3 - 6].

However, these techniques suffer from the following shortcomings:

(a) Amplitude detection processes have inherent limitations such as the loss of phase information, inability to cope with dispersive media, and low resolution.

(b) Spectral resolution is restricted to the reciprocal of the sample spacing in the discrete Fourier transformation [7].

The reconstruction of the geometry and composition of material characteristics based on the measurement of the ultrasound field reflected from a layered structure is known as the *inverse reflecting* problem [8]. The concept of an inverse problem has also been used in other areas, such as aerodynamics, fluid mechanics, speech and image processing, and electromagnetics [9 - 11]. Since a true inverse problem in acoustics is extremely difficult to solve due to the scattering effect and the mode conversion at the interfaces, one needs to use a simplified model with reasonable assumptions to obtain meaningful results for identifying material characteristics.

This work is presented in four parts: the derivation of the wave equation and the first order reconstruction algorithm, the development of the modified *Spectral Prony Algorithm* (SPA) technique which utilizes unique features in the frequency domain of the reflected response of a layered structure, the evaluation of the ultrasonic field within an inhomogeneous and arbitrarily shaped object to complete the theoretical background, and finally an experiment verification of the proposed techniques.

It is first hypothesized that the frequency domain scattered field response of a acoustic medium can be defined entirely as a function of medium geometry and properties. Then, for a layered structure, the medium function approximately comprises a set of natural modes which uniquely determine the structure. The SPA is a specified phase detection technique constructed in such a way that, upon interaction with a certain structure, results in a reflected waveform contain only a pre-specified component of the natural mode spectrum.

The advantages of the SPA technique are twofold. First, it can be used to estimate several material characteristics in a single measurement. The information obtained from this technique is solely based on the echo return from the successive interfaces, rather than the signature of the incident pulse which is difficult to capture experimentally. Second, the diffraction effect can be reduced greatly when the reflections from the interfaces are used as references for successive estimation.

In Chapter 2, the acoustic wave equation is developed. This vector equation forms the basis of all work to be described. In addition, the Born and Rytov approximations are introduced and a linearized model for the scattered field as a function of the object is derived.

Chapter 3 presents a brief overview of some of the more relevant identification schemes developed by other researchers, and underscores the need for the SPA technique. A wave transmission matrix is used to find an expression for the reflected field of a layered structure. This forms the basis of the SPA technique which is useful to extract more than one property.

The SPA concept is introduced in Chapter 4, and expanded upon in detail. Material in this chapter also includes other extraction schemes and provides numerical results to prove that the proposed method is preferred. Chapter 5 presents a theoretical analysis of SPA reconstruction and includes methods of SPA synthesis and interpretation. Since the mathematical approximations and the experimental limitations contribute in different ways to the error in the final outcomes, an overview is also given in this chapter. The mathematical approximations are only valid for some regions of objects, as described in Chapter 2, and the experimental limitations are entirely caused by the limited availability of data. In addition, some signal processing issues will be discussed and experimental results presented.

In certain applications, it is desirable to gain knowledge of the field distribution inside a medium. For example, in hyperthermia treatment of tumors, the induced temperature profile is directly related to the ultrasonic field distribution. Therefore, Chapter 6 follows the wave equations addressed in Chapter 2 and develops a specific algorithm to avoid the singularity of the integration of the Green's function so that the uniqueness of the ultrasonic field is preserved within the medium. In order to complete this important topic, some inhomogeneous models for solving the given problem are also investigated.

Finally, Chapter 7 introduces experimental validation of both the identification of material characteristics of the waveform reflected from thin plexiglass layers, and of the SPA concept itself. Verification of the SPA concept is provided by using the reflection waveform of some multi-layered structures.

CHAPTER 2

PROPAGATION OF ULTRASONIC FIELDS

2.1 Introduction

Characteristic identification from scattered energy cannot be modeled by a set of equations considering forward propagation wave only. Ultrasonic and electromagnetic waves do not travel along straight rays in an inhomogeneous medium with finite boundaries. The backward flow of energy can be described with the wave equation under the assumption that the operating wavelengths are small compared with the physical dimensions of the system. It will be shown that the scattering identifications can be approximated by a non-scattering identification.

First, let us consider the propagation of waves in homogeneous media. The wave equation is a second order linear differential equation. The field intensity at any given location can be obtained by solving the wave equation.

The problem is not to identify a homogeneous media but rather to identify one that is inhomogeneous in nature. To solve the inhomogeneous wave equation, one of two approximations, the Born [19] or the Rytov [20], needed to be used. With these two approximations, expressions for the inhomogeneous scattered field can be obtained.

The theory to be developed will be applicable to both two- and three-dimensional structures. Even in a three-dimensional case, a two-dimensional model can often be used if the structure varies slowly in the third direction. This assumption, for example, is often made in the evaluation of electromagnetic fields distribution [12]. The theory of ultrasonic identification of materials will be presented almost entirely for the two-dimensional case. The reason is that the ideas behind the theory are often easier to reconstruct the material characteristics in two-dimensional case by using spatial transformation technique. In addition, technology has yet to make it practical to implement and to evaluate the results of three-dimension methods. This limitation will certainly be eliminated in the near future, and where the differences are significant, both the two- and three-dimensional solutions will be expected.

2.2 Homogeneous Wave Equation

In a homogeneous medium the propagation of compressional ultrasonic waves can be modeled with the scalar Helmholtz equation [13]. For a temporal frequency of ω radians per second, a scalar potential $\Phi(\vec{r})$ satisfies the equation

$$\nabla^2 \Phi(\vec{r}) + k_o^2 \Phi(\vec{r}) = 0 \ . \tag{2.1}$$

For homogeneous media, the wave number k_o is a constant related to the wavelength λ of the wave by

$$k_o = \frac{2\pi}{\lambda} \ . \tag{2.2}$$

The wavelength λ is related to the temporal frequency of the wave by the propagation speed in the media υ_c or

$$\lambda = \frac{2\pi}{\omega}\upsilon_c \ . \tag{2.3}$$

Furthermore, the compressional ultrasonic field $\vec{u}(\vec{r})$ at position $\vec{r}$ is denoted as

$$\vec{u}(\vec{r}) = -\nabla\Phi(\vec{r}) \ . \tag{2.4}$$

The technique developed in this research are based on harmonic ultrasonic fields, the time dependence of the fields will be suppressed in this work. Thus, all fields should be multiplied by $e^{-j\omega t}$ to find the measured field as a function of time. For ultrasonic fields, $\vec{u}(\vec{r})$ is the displacement field at position $\vec{r}$. Since the time dependence of the fields has been suppressed, $\vec{u}(\vec{r})$ represents the complex amplitude of the field. As a function of time and space, the field is given by

$$\vec{u}(\vec{r}, t) = \mathrm{Re}\left\{ -\nabla\Phi(\vec{r})e^{-j\omega t} \right\} \ . \tag{2.5}$$

The vector gradient operator, "∇", can be expanded into its two dimensional representation and Eq. (2.1) becomes

$$\frac{\partial^2\Phi(\vec{r})}{\partial x^2} + \frac{\partial^2\Phi(\vec{r})}{\partial y^2} + k_o{}^2\Phi(\vec{r}) = 0 \ . \tag{2.6}$$

As a trial solution let

$$\Phi(\vec{r}) = e^{j\vec{k}\cdot\vec{r}} \tag{2.7}$$

where the vector $\vec{k} = (k_x \ , k_y)$ is the two-dimensional propagation vector and $\Phi(\vec{r})$ represents a two-dimensional plane wave of propagation factor $|\vec{k}|$. This form of $\Phi(\vec{r})$ represents the basic function for the two-dimensional Fourier transform [14]. Using this equation, any two-dimensional function can be represented as a weighted sum of plane waves. Calculating the derivatives as indicated in Eq. (2.6), it can be seen that any plane wave that satisfies the condition

$$|\vec{k}| = k_x^2 + k_y^2 = k_o^2 \tag{2.8}$$

is a valid solution to the wave equation. The homogeneous wave equation is a linear differential equation, so the general solution can be written as a weighted sum of each possible plane wave solution. In two dimensions, at a temporal frequency of ω, the potential, $\Phi(\vec{r})$ is given by

$$\Phi(\vec{r}) = \frac{1}{2\pi}\int_{-\infty}^{\infty} A(k_y)e^{j(k_x x + k_y y)}\,dk_y + \frac{1}{2\pi}\int_{-\infty}^{\infty} B(k_y)e^{j(-k_x x + k_y y)}\,dk_y \ , \tag{2.9}$$

and by Eq. (2.8)

$$k_x = \sqrt{k_o^2 - k_y^2} \ . \tag{2.10}$$

The form of this equation might be surprising to the reader for two reasons.

(1) The integral has been split into two parts. The coefficients of waves traveling to the right are represented by $A(k_y)$ and those traveling to the left by $B(k_y)$.

(2) In addition, the limits of the integrals are $-\infty$ and ∞. For k_y^2 greater than k_o^2 the radical in Eq. (2.10) becomes imaginary and the plane wave becomes an evanescent wave.

These are valid solutions to the wave equation, but, because k_x is imaginary, the exponential has a real or attenuating component. This real component that causes the evanescent waves which decay rapidly within several wavelengths [13], and they can often be ignored.

The limited range of valid solutions to the wave equation allows (under certain conditions) an expression to be written for the field in all of 2-D plane given the amplitude of the field along a line. The three-dimensional version of this idea gives the field in 3-D space, if the field is known at all points on a plane.

Let us consider a plane acoustic wave travelling in the direction shown in Figure 2.1. By calculating the one-dimensional Fourier transform of the field along the direction of propagation, the field can be decomposed into a number of one-dimensional components. Each of these one-dimensional components can then be attributed to one of the valid wave solutions to the homogeneous wave equation. Referring to Eq. (2.9), there will exist two solutions that satisfy the wave equation with a value of k_y. If the incident field has been defined to propagate toward the right, then a one-dimensional Fourier component at a value of k_y can be attributed to a two-dimensional wave with a propagation vector of ($\sqrt{k_o^2 - k_y^2}$, k_y). This can be formulated on a more precise mathematical basis, if the one-dimensional Fourier transform of the field is compared with the general form of the wave equation. When only the forward travelling wave is considered, the general solut ion to the wave equation becomes

$$\Phi(\vec{r}) = \frac{1}{2\pi} \int_{-\infty}^{\infty} A(k_y) e^{j(k_x x + k_y y)} dk_y \quad . \tag{2.11}$$

Now, if the origin of the wave propagation is chosen to coincide with $x = 0$, then the expression for the field becomes

$$\Phi(0, y) = \frac{1}{2\pi} \int_{-\infty}^{\infty} A(k_y) e^{jk_y y} dk_y \quad . \tag{2.12}$$

This equation establishes the link between the one-dimensional Fourier transform of the field along the line to the two-dimensional field. The coefficients $A(k_y)$ are given by the one-dimensional Fourier transform of the field

$$A(k_y) = FT\left\{\Phi(0, y)\right\} \quad . \tag{2.13}$$

where *FT* denotes the Fourier transform.

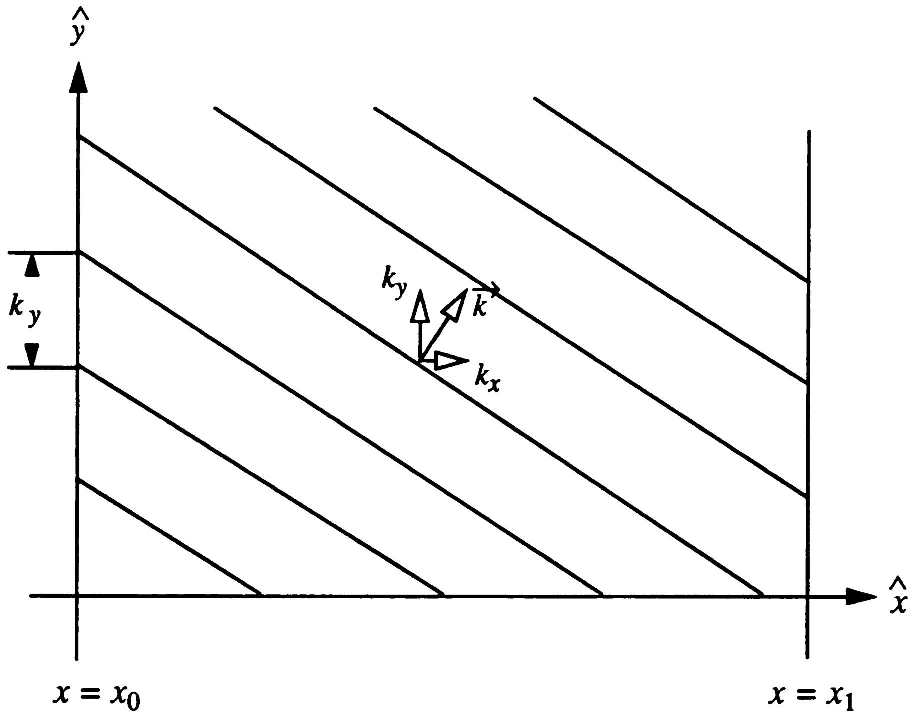

Figure 2.1 : A plane wave with direction cosines $(\sqrt{k_o^2 - k_y^2}, k_y)$ is propagating along the $\vec{k}$ direction.

If the propagation vector is known, then all the sources for the field potential $\Phi(x=x_o, y) = \Phi_o e^{j(k_x x_o + k_y y)}$ can be decomposed into plane wave components. For a compressional plane wave, the ultrasonic field $\vec{u}$ can be expressed as

$$\vec{u}(x=x_o, y) = -\nabla\Phi(x=x_o, y) = \hat{y}\ U_o e^{j(k_x x_o + k_y y)} \tag{2.14}$$

where $U_o = jk_y \Phi_o$.

The field undergoes a phase shift as it arrives at $x = x_1$, and the acoustic field can be written as

$$\begin{aligned} \vec{u}(x=x_1, y) &= -\nabla\Phi(x=x_1, y) \\ &= \hat{y}\ U_o e^{j(k_x x_o + k_y y)}\ e^{jk_x(x_1 - x_o)} = \vec{u}(x=x_o, y)\ e^{jk_x(x_1 - x_o)} \ . \end{aligned} \tag{2.15}$$

Thus, the complex amplitude of the plane wave at $x = x_1$ is related to its complex amplitude at $x = x_o$ by a factor $e^{jk_x(x_1 - x_o)}$.

The process of evaluating the field at $x = x_1$ is as follows:

(1) Obtain the Fourier decomposition of Φ as a function of k_y by taking the Fourier transform of $\Phi(x_o, y)$.

(2) Obtain the plane wave expression at $x = x_1$ by multiplying by the phase factor $e^{jk_x(x_1 - x_o)}$, where as before $k_x = \sqrt{k_o^2 - k_y^2}$.

(3) Obtain the field potential $\Phi(x, y)$ by taking the inverse Fourier transform of the plane wave decomposition.

2.3 Inhomogeneous Wave Equation

Considering an inclusion occupying a volume V_s in space, embedded in a homogeneous background medium (see Figure 2.2), the incident wave induces a scattered force [15]. This force, $\vec{f}_s$ is calculated for an observation point that arises from the spatial variations in density (ρ) and lame parameters (λ and μ)

$$\vec{f}_s(\vec{r}) = \omega^2\delta\rho(\vec{r})\vec{u}(\vec{r}) + \left[\delta\lambda(\vec{r}) + 2\delta\mu(\vec{r})\right]\nabla\left[\nabla \cdot \vec{u}(\vec{r})\right] \tag{2.16}$$
$$- \delta\mu(\vec{r})\nabla\times\nabla\times\vec{u}(\vec{r})$$

where ω is the temporal frequency and $\delta\rho(\vec{r})$, $\delta\lambda(\vec{r})$, $\delta\mu(\vec{r})$ are the position-dependent incremental changes in elastic parameters with respect to the background. They are

$$\delta\rho(\vec{r}) = \rho(\vec{r}) - \rho_o \ , \tag{2.17a}$$

$$\delta\lambda(\vec{r}) = \lambda(\vec{r}) - \lambda_o \ , \tag{2.17b}$$

$$\text{and} \qquad \delta\mu(\vec{r}) = \mu(\vec{r}) - \mu_o \ , \tag{2.17c}$$

with ρ_o, λ_o, and μ_o being the density, bulk modulus, and shear modulus of the background respectively. These incremental changes are proportional to the elastic parameter contrasts between the background and inhomogeneous media.

A more general form of the compressional wave equation can be written as

$$\nabla^2\Phi(\vec{r}) + k_o^2\Phi(\vec{r}) = \frac{-1}{\omega^2\rho_o}\nabla \cdot \vec{f}_s(\vec{r}) \tag{2.18}$$

where $k_o = \dfrac{\omega}{\upsilon_c}$, and $\upsilon_c = \sqrt{\dfrac{\lambda_o + 2\mu_o}{\rho_o}}$ is the propagation speed in the background.

The term on the right-hand side of Eq. (2.18), is the forcing function of the differential equation $\left[\nabla^2 + k_o^2\right]\Phi(\vec{r})$. Note that Eq. (2.18) is a scalar wave equation. As a result, all depolarization effects can be ignored. It has been shown [16] that the depolarization effects can be ignored when the compressional waves propagate through a viscous compressible fluid. If this condition is not met, the forcing function would be of a much more complicated form [17].

The potential field $\Phi(\vec{r})$ contains two components -- the incident field $\Phi_o(\vec{r})$ and the scattered field $\Phi_s(\vec{r})$. The incident field satisfies the homogeneous wave equation

$$\left[\nabla^2 + k_o^2\right]\Phi_o(\vec{r}) = 0 \ , \tag{2.19}$$

and the scattered field $\Phi_s(\vec{r})$ is primarily based on medium inhomogeneities,

$$\Phi_s(\vec{r}) = \Phi(\vec{r}) - \Phi_o(\vec{r}) \ . \tag{2.20}$$

The wave equation then becomes

$$\left[\nabla^2 + k_o^2\right]\Phi_s(\vec{r}) = \frac{-1}{\omega^2\rho_o}\nabla\cdot\vec{f}_s(\vec{r}) \ . \tag{2.21}$$

The scalar Helmholtz Eq. (2.21) cannot be used to solve $\Phi_s(\vec{r})$ directly. However, a solution can be obtained through the use of the Green's function technique [18]. The Green's function, which is a solution of the differential equation

$$\left[\nabla^2 + k_o^2\right]G(\vec{r}|\vec{r}\,') = -\,\delta(\vec{r}-\vec{r}\,') \tag{2.22}$$

is written in free-space as

$$G(\vec{r}|\vec{r}\,') = \frac{e^{jk_oR}}{4\pi R} \quad ; \ R = |\vec{r}-\vec{r}\,'| \ . \tag{2.23}$$

In two-dimensional problems, the solution of Eq. (2.22) can be written in terms of a zero-order Hankel function of the first kind and can be expressed as

$$G(\vec{r}|\vec{r}\,') = \frac{j}{4}H_o^{(1)}(k_oR) \ . \tag{2.24}$$

Notice that the Green's function $G(\vec{r}|\vec{r}\,')$ is a function of the difference between the field point and source point $\vec{r}-\vec{r}\,'$, so the function is often represented as $G(\vec{r}-\vec{r}\,')$. Since the forcing function in Eq. (2.22) represents a point source, the Green's function can be considered as a single point scatterer.

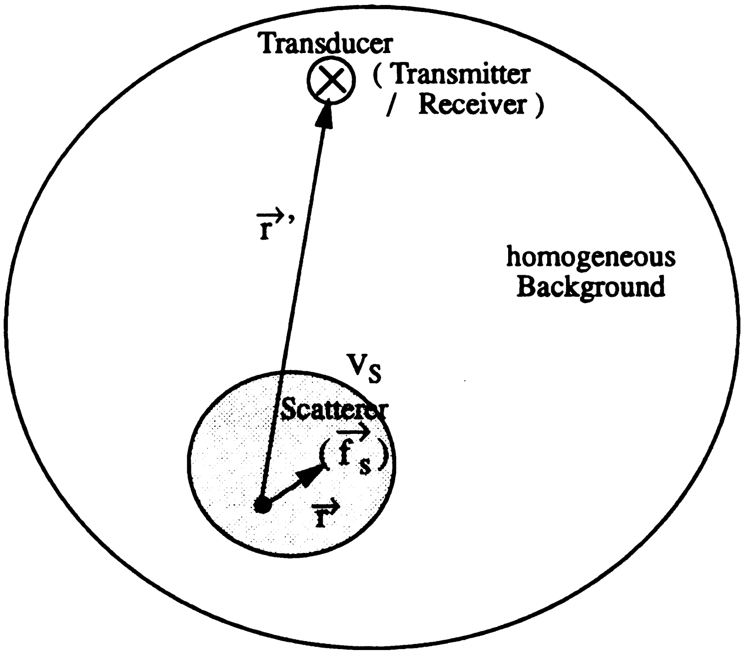

Figure 2.2 : General scattering configuration .

It is possible to represent the forcing function of the wave equation as an array of impulses such that

$$\nabla \cdot \vec{f}_s(\vec{r}) = \int \nabla' \cdot \vec{f}_s(\vec{r}\,')\delta(\vec{r}-\vec{r}\,')dv' \quad . \tag{2.25}$$

In this expression, the forcing function of the inhomogeneous wave equation becomes a summation of impulses weighted by $\nabla \cdot \vec{f}_s(\vec{r})$ and shifted by $\vec{r}\,'$. Green's function represents the solution of the wave equation for a single impulse response. The eventual field solution can be obtained by summing the scattered fields due to each individual point scatterer.

Following the approach, the total field due to the impulse $\nabla' \cdot \vec{f}_s(\vec{r}\,')\delta(\vec{r}-\vec{r}\,')$ can be written as the summation of scalar and shifted versions of the impulse response $G(\vec{r})$. This is a convolution process and the total field resulting from all sources on the right hand side of Eq. (2.21) is obtained from the following superposition:

$$\Phi_s(\vec{r}) = \frac{1}{\omega^2\rho_o}\int_V \nabla' \cdot \vec{f}_s(\vec{r}\,')G(\vec{r}|\vec{r}\,')dv' \quad . \tag{2.26}$$

Recall that of Eq. (2.4), the compressional ultrasonic scattered field $\vec{u}^s(\vec{r})$ at a position $\vec{r}$ can be expressed as

$$\begin{aligned} \vec{u}^s(\vec{r}) &= -\nabla\Phi_s(\vec{r}) \\ &= -\frac{1}{\omega^2\rho_o}\left[\nabla\int_V \nabla' \cdot \vec{f}_s(\vec{r}\,')G(\vec{r}|\vec{r}\,')dv'\right] \end{aligned} \tag{2.27}$$

where $G(\vec{r}|\vec{r}\,') = \dfrac{e^{jk_o|\vec{r}-\vec{r}\,'|}}{4\pi|\vec{r}-\vec{r}\,'|}$. Since the integration is with respect to the source coordinate, the unprimed gradient operation can be put inside the integral,

$$\vec{u}^s(\vec{r}) = -\frac{1}{\omega^2\rho_o}\left[\int_V \nabla' \cdot \vec{f}_s(\vec{r}\,')\nabla G(\vec{r}|\vec{r}\,')dv'\right] \quad . \tag{2.28}$$

If the observation point $\vec{r}$ is outside the inhomogeneous volume, V_s, then the point $\vec{r}\,'$ will not pass through $\vec{r}$ when carrying out the integration. To carry out the integration, we need to use the dyadic identity [12]

$$\nabla' \cdot \left[\vec{f}_s(\vec{r}\,')\,\nabla G(\vec{r}|\vec{r}\,')\right] = \left[\nabla' \cdot \vec{f}_s(\vec{r}\,')\right]\nabla G(\vec{r}|\vec{r}\,') + \vec{f}_s(\vec{r}\,') \cdot \nabla'\nabla G(\vec{r}|\vec{r}\,') \tag{2.29}$$

and the symmetry property of the Green's function

$$\nabla' G(\vec{r}|\vec{r}\,') = -\nabla G(\vec{r}|\vec{r}\,') \ . \tag{2.30}$$

If one substitutes equation Eq. (2.29) and Eq. (2.30) into Eq. (2.28), the scattered ultrasonic field becomes

$$\vec{u}^s(\vec{r}) = -\frac{1}{\omega^2\rho_o}\left[\int_V \nabla' \cdot \left[\vec{f}_s(\vec{r}\,')\,\nabla G(\vec{r}|\vec{r}\,')\right]dv' - \int_V \vec{f}_s(\vec{r}\,') \cdot \nabla\nabla G(\vec{r}|\vec{r}\,')dv'\right] . \tag{2.31}$$

Defining $\overleftrightarrow{G}(\vec{r}|\vec{r}\,') = \frac{1}{\omega^2\rho_o}\nabla\nabla G(\vec{r}|\vec{r}\,')$, Eq. (2.31) is rewritten as

$$\vec{u}^s(\vec{r}) = -\int_S \left[\hat{n} \cdot \vec{f}_s(\vec{r}\,')\right]\nabla G(\vec{r}|\vec{r}\,')ds' + \int_V \vec{f}_s(\vec{r}\,') \cdot \overleftrightarrow{G}(\vec{r}|\vec{r}\,')dv' \ . \tag{2.32}$$

In general, it will be assumed that the volume V_s has a finite size; therefore $\vec{f}_s(\vec{r})$ is zero outside the volume. Thus, the first surface integration of Eq. (2.32) vanishes at a specified point $\vec{r}$ outside V_s, and Eq. (2.32) reduces to

$$\vec{u}^s(\vec{r}) = \int_V \vec{f}_s(\vec{r}\,') \cdot \overleftrightarrow{G}(\vec{r}|\vec{r}\,')dv' \ . \tag{2.33}$$

From the conservation of momentum, $\vec{f}(\vec{r})\,\Delta t = -\rho(\vec{r})\,\Delta\left[\frac{d\vec{u}(\vec{r},t)}{dt}\right]$, and when

$\Delta t \rightarrow 0$, the scattered force $\vec{f}_s(\vec{r})$ is

$$\vec{f}_s(\vec{r}) = -\,\delta\rho(\vec{r})\left[\frac{d^2\vec{u}(\vec{r},t)}{dt^2}\right] \tag{2.34}$$

$$= \omega^2\delta\rho(\vec{r})\vec{u}(\vec{r})$$

$$= m(\vec{r})\vec{u}(\vec{r})$$

where $m(\vec{r}) = \omega^2\delta\rho(\vec{r})$ represents all inhomogeneities of the medium. With this scattered force expression, the scattered field becomes

$$\vec{u}^s(\vec{r}) = \int_V m(\vec{r}\,')\vec{u}(\vec{r}\,')\cdot\overleftrightarrow{G}(\vec{r}|\vec{r}\,')dv' \quad . \tag{2.35}$$

At first glance it appears that this is the solution for the scattered field. However, notice that the scattered field $\vec{u}^s(\vec{r})$ is expressed in terms of the total field, $\vec{u}(\vec{r}) = \vec{u}^i(\vec{r}) + \vec{u}^s(\vec{r})$. In order to solve the scattered field, some approximations must be made.

2.4 Approximations for Solving the Scattered Field

In the last section, an inhomogeneous integral equation was derived for finding the scattered field $\vec{u}^s(\vec{r})$ as a function of the inhomogeneities of the medium. This equation cannot be solved in a straightforward manner. However, a solution can be obtained by using some approximations. These approximations, the Born [19] and the Rytov [20], are valid under different condition, but the forms of the resulting solutions are quite similar. These approximations are the foundation of solving the ultrasonic scattering problem.

Mathematically speaking, Eq. (2.35) is a Fredholm equation of the second kind [21]. A number of mathematicians have presented work describing the solution of scattering integrals [22, 23]. We will adopt these approximations to the ultrasonic scattering problem with some modifications for reducing computation time.

2.4.1 The Born Approximation

The Born approximation is the simpler of the two approaches. Recall that the total field $\vec{u}(\vec{r})$ is expressed as the sum of the incident field $\vec{u}^i(\vec{r})$ and a small scattered field $\vec{u}^s(\vec{r})$,

$$\vec{u}(\vec{r}) = \vec{u}^i(\vec{r}) + \vec{u}^s(\vec{r}) \ . \tag{2.36}$$

The integral of Eq. (2.35) is then

$$\vec{u}^s(\vec{r}) = \int_V m(\vec{r}\,')\vec{u}^i(\vec{r}\,') \cdot \overleftrightarrow{G}(\vec{r} \mid \vec{r}\,')dv' \ . \tag{2.37}$$

$$+ \int_V m(\vec{r}\,')\vec{u}^s(\vec{r}\,') \cdot \overleftrightarrow{G}(\vec{r} \mid \vec{r}\,')dv' \ ,$$

If the scattered field $\vec{u}^s(\vec{r})$ is small compared to $\vec{u}^i(\vec{r})$, then the effects of the second integral can be ignored and the following approximation can be made:

$$\vec{u}^s(\vec{r}) \approx \vec{u}^B(\vec{r}) = \int_V m(\vec{r}\,')\vec{u}^i(\vec{r}\,') \cdot \overleftrightarrow{G}(\vec{r} \mid \vec{r}\,')dv' \ . \tag{2.38}$$

As a result, under the Born approximation, the magnitude of the scattered field

$$\vec{u}^s(\vec{r}) = \vec{u}(\vec{r}) - \vec{u}^i(\vec{r}) \tag{2.39}$$

is smaller than the magnitude of the incident field $\vec{u}^i(\vec{r})$.

If the medium is homogeneous, it is possible to express this condition as a function of the size of the medium and its refractive index. Let the incident wave $\vec{u}^i(\vec{r})$ be a plane wave propagating in the direction of the vector, $\vec{k}_o = \hat{k}_o k_o$. For a large medium, the field inside the medium will not be adequately approximated by the incident field

$$\vec{u}(\vec{r}) \neq \vec{u}^i(\vec{r}) = \hat{k}_o A_o \ e^{j\vec{k}_o \cdot \vec{r}} \ . \tag{2.40}$$

In addition, the refractive index n_δ is a variable as well. The field inside the medium has the following variation

$$\vec{u}(\vec{r}) = \hat{k}A_m e^{j(1+n_\delta)\vec{k}_o \cdot \vec{r}} \quad . \tag{2.41}$$

The phase difference between the incident field and the field inside the medium can be obtained by integrating the refractive index over the length of the medium. For a homogeneous layer of thickness d, the total phase shift through the layer is

$$\text{Phase Change} = 2\pi n_\delta \frac{d}{\lambda} \tag{2.42}$$

where λ is the wavelength of the incident wave. For the Born approximation to be valid, a necessary condition is that the change in phase between the incident field and the wave propagating through the layer be less than π [24]. This condition can be expressed mathematically as

$$d n_\delta < \frac{\lambda}{2} \quad . \tag{2.43}$$

2.4.2 The Rytov Approximation

The Rytov approximation is another approximation for obtaining the scattered field and is valid under slightly different restrictions. The assumption is that the total field has a complex phase [20]

$$\vec{u}(\vec{r}) = \hat{k}\, A_o e^{\phi(\vec{r})} \quad . \tag{2.44}$$

Recall that the wave equation for the ultrasonic field is

$$\nabla^2 \vec{u}(\vec{r}) + k_0^2(\vec{r})\vec{u}(\vec{r}) = -m(\vec{r})\vec{u}(\vec{r}) \quad . \tag{2.45}$$

In order to evaluate the complex phase, we substitute Eq. (2.44) into Eq. (2.45)and get the wave equation as

$$\nabla \cdot \left[\nabla\phi(\vec{r}) e^{\phi(\vec{r})} \right] + k_o^2(\vec{r}) e^{\phi(\vec{r})} = -m(\vec{r}) e^{\phi(\vec{r})} \tag{2.46}$$

or simply

$$\left[\nabla\phi(\vec{r}) \right]^2 + \nabla^2\phi(\vec{r}) + k_o^2 = -m(\vec{r}) \ . \tag{2.47}$$

The total phase function ϕ is the sum of the phase of the incident field ϕ_o and the scattered phase ϕ_s,

$$\phi(\vec{r}) = \phi_o(\vec{r}) + \phi_s(\vec{r}) \ . \tag{2.48}$$

Substituting Eq. (2.48) into Eq. (2.47), one has

$$\begin{aligned} \left[\nabla\phi_o(\vec{r}) \right]^2 + 2\nabla\phi_o(\vec{r}) \cdot \nabla\phi_s(\vec{r}) + \left[\nabla\phi_s(\vec{r}) \right]^2 + \nabla^2\phi_o(\vec{r}) \\ + \nabla^2\phi_s(\vec{r}) + k_o^2 + m(\vec{r}) = 0 \ . \end{aligned} \tag{2.49}$$

The incident field satisfies the homogeneous wave equation,

$$\left[\nabla\phi_o(\vec{r}) \right]^2 + \nabla^2\phi_o(\vec{r}) + k_o^2 = 0 \ . \tag{2.50}$$

With this consideration, the over-all wave equation becomes

$$2\nabla\phi_o(\vec{r}) \cdot \nabla\phi_s(\vec{r}) + \nabla^2\phi_s(\vec{r}) = -\left[\nabla\phi_s(\vec{r}) \right]^2 - m(\vec{r}) \ . \tag{2.51}$$

It can be linearized by considering the following relationship,

$$\nabla^2\left[u^i(\vec{r})\phi_s(\vec{r}) \right] = \nabla \cdot \left[\nabla u^i(\vec{r})\phi_s(\vec{r}) + u^i(\vec{r})\nabla\phi_s(\vec{r}) \right] \ . \tag{2.52}$$

Expanding the right-hand side of this equation, we have

$$\begin{aligned} \nabla^2\left[u^i(\vec{r})\phi_s(\vec{r}) \right] = \left[\nabla^2 u^i(\vec{r}) \right]\phi_s(\vec{r}) + 2\nabla u^i(\vec{r}) \cdot \nabla\phi_s(\vec{r}) \\ + u^i(\vec{r})\nabla^2\phi_s(\vec{r}) \ . \end{aligned} \tag{2.53}$$

Using a plane wave for the incident field,

$$\vec{u}^{i}(\vec{r}) = \hat{k}\, A_o e^{j\vec{k}_o\cdot\vec{r}} \quad . \tag{2.54}$$

The Laplacian of the incident field is

$$\nabla^2 u^i(\vec{r}) = -k_o^2\, u^i(\vec{r}) \quad . \tag{2.55}$$

Finally, the inhomogeneous wave equation becomes

$$\left[\nabla^2 + k_o^2\right]\vec{u}^{\,i}(\vec{r})\phi_s(\vec{r}) = -\vec{u}^{\,i}(\vec{r})\left[\left[\nabla\phi_s(\vec{r})\right]^2 + m(\vec{r})\right] \quad . \tag{2.56}$$

The solution of this differential equation can be expressed in the form of an integral equation,

$$\vec{u}^{i}(\vec{r})\phi_s(\vec{r}) = \int_V \vec{u}^{i}(\vec{r}\,')\left[\left[\nabla\phi_s(\vec{r}\,')\right]^2 + m(\vec{r}\,')\right]\cdot\overleftrightarrow{G}(\vec{r}|\vec{r}\,')dv' \quad . \tag{2.57}$$

When the field of interest is in the far-zone region, the ultrasonic field can be treated as a constant quantity. The terms in the brackets of the above equation can then be approximated by

$$\left[\nabla\phi_s(\vec{r})\right]^2 + m(\vec{r}\,') \approx m(\vec{r}\,') \quad . \tag{2.58}$$

With this approximation, Eq. (2.57) becomes

$$\vec{u}^{i}(\vec{r})\phi_s(\vec{r}) = \int_V m(\vec{r}\,')\vec{u}^{i}(\vec{r}\,')\cdot\overleftrightarrow{G}(\vec{r}|\vec{r}\,')dv' \quad . \tag{2.59}$$

Thus, the complex phase of the scattered field becomes

$$\phi_s(\vec{r}) = \frac{1}{\vec{u}^{i}(\vec{r})}\int_V m(\vec{r}\,')\vec{u}^{i}(\vec{r}\,')\cdot\overleftrightarrow{G}(\vec{r}|\vec{r}\,')dv' \quad . \tag{2.60}$$

Substituting the expression for $\vec{u}^{B}(\vec{r})$ in Eq. (2.38), the Rytov approximation can be written as

$$\phi_s(\vec{r}) = \frac{\vec{u}^{B}(\vec{r})}{\vec{u}^{i}(\vec{r})} \quad . \tag{2.61}$$

In the far-zone region, Eq. (2.58) is valid. Furthermore, $m(\vec{r})$ can be put in terms of the change of the refractive index

$$m(\vec{r}) = k_o^2\left[2n_\delta(\vec{r}) + n_\delta^2(\vec{r})\right] . \tag{2.62}$$

For small variation of n_δ,

$$m(\vec{r}) \approx 2k_o^2 n_\delta(\vec{r}) , \tag{2.63}$$

and the Rytov approximation is valid, however, the following condition must be satisfied,

$$n_\delta(\vec{r}) \gg \frac{\left[\nabla\phi_s(\vec{r})\right]^2}{k_o^2} . \tag{2.64}$$

This can be considered by observing that to the assumption of Eq. (2.58), the scattered phase $\phi_s(\vec{r})$ is linearly dependent on the refractive change; therefore, the second term in Eq. (2.62) above can be safely ignored for a small refractive change. The term $\nabla\phi_s(\vec{r})$ is the change of the complex scattered phase per unit distance, while k_o is the wave number, the alternate form of the Rytov approximation is

$$n_\delta(\vec{r}) \gg \left[\frac{\nabla\phi_s(\vec{r})\lambda}{2\pi}\right]^2 . \tag{2.65}$$

In this result, the change in scattered phase $\phi_s(\vec{r})$ over one wavelength has a dominant effect on the solution of the scattered field.

Evaluation of $\vec{u}^{\,B}(\vec{r})$ for the Rytov case is not as straightforward as in the case of Born approximation. Recall that the total field is

$$\vec{u}(\vec{r}) = \vec{u}^{\,i}(\vec{r}) + \vec{u}^{\,s}(\vec{r}) = \hat{k}\left[A_o e^{\phi_o(\vec{r}) + \phi_s(\vec{r})}\right] . \tag{2.66}$$

after rearranging the exponential terms, one has

$$\vec{u}^{\,s}(\vec{r}) = \hat{k}\left[A_o e^{\phi_o(\vec{r})}\left[e^{\phi_s(\vec{r})} - 1\right]\right] = \vec{u}^{\,i}(\vec{r})\left[e^{\phi_s(\vec{r})} - 1\right] . \tag{2.67}$$

The scattered phase $\phi_s(\vec{r})$ now is

$$\phi_s(\vec{r}) = ln\left[\frac{\vec{u}^s(\vec{r})}{\vec{u}^i(\vec{r})} + 1\right] \ . \tag{2.68}$$

From Eq. (2.61), the field $u^B(\vec{r})$ for the Rytov approximation becomes

$$\vec{u}^B(\vec{r}) = \vec{u}^i(\vec{r})\ ln\left[\frac{\vec{u}^s(\vec{r})}{\vec{u}^i(\vec{r})} + 1\right] \ . \tag{2.69}$$

Since the natural logarithm is a multiple-valued function, one must be careful in choosing its value over a given region. For continuous functions, there is no ambiguity about the solution since only one value will satisfy the continuity requirement. On the other hand, for sampled signals, the choice becomes more difficult and one must resort to a phase-wrapping algorithm for choosing the proper phase.

Under the Rytov approximation, the total compressional field is expressed as

$$u(\vec{r}) = A_o e^{\phi_o(\vec{r}) + \phi_s(\vec{r})} \ . \tag{2.70}$$

Substituting the scattered phase Eq. (2.61), and the incident field Eq. (2.54), into this expression,

$$\begin{aligned} u(\vec{r}) &= A_o e^{j\vec{k}_o \cdot \vec{r} + u^B(\vec{r}) \cdot A_o^{-1} exp(-j\vec{k}_o \cdot \vec{r})} \\ &= u^i(\vec{r})\ e^{u^B(\vec{r}) \cdot A_o^{-1} exp(-j\vec{k}_o \cdot \vec{r})} \ . \end{aligned} \tag{2.71}$$

The first exponential can be expanded into a power series. When $u^B(\vec{r})$ is small, the total field can be linearized,

$$\begin{aligned} u(\vec{r}) &= u^i(\vec{r})\left[1 + u^B(\vec{r}) \cdot A_o^{-1} e^{-j\vec{k}_o \cdot \vec{r}}\right] \\ &= u^i(\vec{r}) + u^B(\vec{r}) \ . \end{aligned} \tag{2.72}$$

When the magnitude of the scattered field is small, the Rytov solution approaches the Born solution in Eq. (2.38).

The similarity between the expressions for the Born and the Rytov solutions will form the basis of the reconstruction algorithm to be considered in this work. In the Born approximation, the complex amplitude of the scattered field is measured, and this measurement is used as an estimate of the function $\vec{u}^B(\vec{r})$, while in the Rytov case, $\vec{u}^B(\vec{r})$ is estimated from the complex phase of the scattered field. Since the Rytov approximation is considered more complex [19] than the Born approximation, it might provide a better estimation of $\vec{u}^B(\vec{r})$.

CHAPTER 3

ULTRASONIC IDENTIFICATION OF THE LAYERED STRUCTURE

3.1 Introduction

The identification of material characteristics in its basic form is an inverse problem -- the reconstruction of the geometry and composition of a medium from measurements of scattered ultrasonic radiation [26]. The medium can then be identified or discriminated from other media or classes of media by comparison to known properties and compositions [27].

In a less rigid sense, identification of material characteristics involves the extraction of features from the measured scattered ultrasonic field which correspond uniquely to an individual medium [28]. Identification is then accomplished by comparing these features.

Ultrasonic material features for a layered structure medium are closely related to attenuation coefficients, wave velocities in the medium, and reflectivity at each interface. These features can take advantage of all the information contained in the scattered field such as the amplitude, phase and frequency content.

Whereas the solution of a true inverse problem requires an infinite amount of information (i.e. a measurement of the scattered field at all frequencies) [29], in practice, only a single feature can ordinarily be acquired for the identification of different materials [30].

In Section 3.2, a short overview of some of the more recent methods conceived for ultrasonic material identification is presented. This review is not exhaustive. The goal is to place the identification technique of this thesis in a proper perspective. The two schemes suggested in Sections 3.3 and 3.4 will be compared. It will also be shown that they are evaluations of the ultrasound field at a specified position. Finally, the wave transmission matrix and an ultrasound field integral equation of the ultrasound scattering field, resulting from a surface force induced by the incident field, will be described in Section 3.5. However, the main focus will be on overcoming two drawbacks in ultrasonic identification of materials:

(1) The derivation is simply based on the surface reflection force at the planar surface of the medium rather than calculated by the complex integration of the 3-D dyadic Green function which is difficult to compute mathematically.

(2) The parameter reconstruction can be reduced greatly when the scattered model of the medium is evaluated by using this approach.

3.2 Ultrasonic Identification Schemes

The identification schemes reviewed in this section can be generally divided into two fundamental groups. The first involves the use of the amplitude of echo signals, the second utilizes the frequency response of the medium.

[A] Reflection Techniques

- Correlation Algorithm -- In the case of time-harmonic excitation, it is convenient to consider a layered structure as a "transmission line" [31]. The ultrasonic wave backscattered from the perfectly homogeneous medium can be related to the incident pulse wave through

$$u^s(t) = h(t) * u^i(t) \tag{3.1}$$

where " * " denotes the convolution operation and $h(t)$ is the 1-D impulse response. This equation describes the delays in propagation between the incident and reflected waves, and is a function of the layer thicknesses and wave numbers. The impulse response $h(t)$ of an echo return is in the form of

$$h(t) = \sum_{n=1}^{N} a_n \delta(t - \tau_n) \tag{3.2}$$

where τ_n, properly scaled, corresponds to the locations of the reflecting interfaces. Thus, the mapping is one-to-one and the reflection coefficients can be exactly evaluated by using the correlation theorem [32]

$$C_{u^s u^i}(\tau) = \sum_{n=1}^{N} a_n \; C_{u^i u^i}(\tau_n) \tag{3.3}$$

where " C " denotes the correlation function.

- Deconvolution Algorithm -- The discrete component of the reflected signals in the opposite direction of the incident ultrasound wave can be written as [33]

$$u^s(n) = \sum_{k=1}^{P} a(k) u^s(n-k) + r(n) \tag{3.4}$$

where P is the order of the model and $r(n)$ is an aperiodic pulse train, corresponding to the reflectivity

$$r(n) = \sum_{i=1}^{I} b(i) \delta(i - P_i) \tag{3.5}$$

where $b(i)$ is the i^{th} coefficient and P_i is related to the i^{th} interface. Then the common autoregressive model used in many digital signal processing applications [34] can be adopted to reconstruct the system $r(n)$. However, ultrasound identification by reconstructing the reflection coefficients is impractical since measurements could be deteriorated due to the refraction effect. Rather, the reflection property of any interface can be characterized by its dispersion.

[B] Frequency Response Techniques

Quite a large number of ultrasound identification schemes have been developed based on the frequency response of the medium. Two of these will be considered in this section.

- Spectral Difference Algorithm -- A very interesting ultrasound identification scheme which simply describes the attenuation factor, $\alpha(f) = \alpha \cdot f$, has linear frequency dependence [35]. Then the frequency domain response of the biological tissue, illuminated by an incident wave, can be denoted as [36]

$$|H(f)|^2 = e^{-\alpha(f) \cdot 2D} = e^{-2\alpha f D} \tag{3.6}$$

where $2D$ is the double thickness of the tissue. Using this relationship, the attenuation factor α can be evaluated by

$$\alpha = \frac{-\log\left[|H(f)|^2\right]}{2fD} \quad . \tag{3.7}$$

- Phase Spectrum Algorithm -- An ultrasonic wave propagating in an unbounded medium in a positive direction can be expressed as [4]

$$u(x,t) = Ae^{j(\omega t - kx - \phi)} e^{-\alpha x} \tag{3.8}$$

where A is amplitude, ω is temporal frequency, k denotes the wave number, ϕ is the related phase, and α denotes the attenuation.

It can be shown [5] that any permissible propagating waveform combines with all reverberations can be expressed as

$$u(x,t) = \frac{1}{2\pi}\int_{-\infty}^{+\infty}\left[\int_{-\infty}^{+\infty} A(\omega,t)e^{-\phi}d\phi\right] e^{j(\omega t-kx)}e^{-\alpha x}d\omega \ . \tag{3.9}$$

For a referred point $x = 0$, Eq. (3.9) becomes

$$u(0,t) = \frac{1}{2\pi}\int_{-\infty}^{+\infty}\left[\int_{-\infty}^{+\infty} A(\omega,t)e^{-\phi}d\phi\right] e^{j\omega t}d\omega \ . \tag{3.10}$$

Applying the inverse Fourier transform technique, one obtains

$$U(0,t) = \int_{-\infty}^{+\infty} A(\omega,t)e^{-\phi}d\phi = \int_{-\infty}^{+\infty} u(0,t)e^{-j\omega t}dt \ . \tag{3.11}$$

Similarly, we will get

$$U(x,t) = U(0,t)e^{-jkx}e^{-\alpha x} \ . \tag{3.12}$$

With the non-dispersive assumption, the difference in the phase spectrum of these near and far region waves is then

$$\Delta\phi = \phi_f - \phi_n = kD = \frac{\omega D}{\upsilon_c} \tag{3.13}$$

where D is the spatial distance, ϕ_n and ϕ_f are the corresponding phase to the near and far regions respectively, and υ_c is the wave velocity in the medium.

As it is not possible to identify all materials with these assumptions, it is necessary to approximate the linear frequency dependence within a specified frequency band, and to consider the dispersive properties of the medium with some approximations. These issues will be addressed in the following sections.

3.3 Backward Scattering Measurements

In this section, we first review the salient features of the deviation of the 3-D dyadic Green function for a planar layered medium formerly proposed in Chapter 2.

When an elastic material is excited by a source, both compressional (C) and shear (S) waves could be launched. Shear wave can be further partitioned into shear vertical (SV) and shear horizontal (SH) polarizations [37]. As the medium is planar layered, C and SV waves are coupled by boundary conditions on horizontal planes (i.e., an incident C wave on the interface between two solids gives rise to both reflected and transmitted of C and SV waves). On the other hand, SH waves do not couple to C and SV waves [38]. Using this decomposition of waves and taking into account the coupling at boundaries and the multiple reflections within the layers, it is possible to derive explicit equations for a dyadic Green function for a perfectly layered structure.

In particular, it can be shown that when the observation point $\vec{r}$ and the source point $\vec{r}\,'$ are in the same layer, $\overleftrightarrow{G}$ is comprised of a free field (singular at $\vec{r} = \vec{r}\,'$) and a regular part resulting from the contributions of the layered structure. If the source and the observation points are not in the same layer, $\overleftrightarrow{G}$ is comprised of only a regular part. Once $\overleftrightarrow{G}$ is determined, the ultrasound field for an arbitrary source is obtained by applying this operator over the volume of the source weighted by an equivalent force equation (see Eq. (2.35)).

For an identification problem, we can denote $\vec{u}^s(\vec{r})$ to represent the field at point $\vec{r}$ which was induced by the surface reflection force to compute the ultrasound field. Assume the medium is insonified by a time-harmonic transducer placed in the upper half-space labeled 1, as shown in Figure 3.1, and assume it is filled with fluid. The axis of the transducer is perpendicular to the plane of the figure, and the wave is traveling along the $\hat{x}$ direction as depicted on the figure. As a result, the displacement field anywhere in the space will depend only on the lateral coordinate y and the depth coordinate x. The origin is taken at the interface between layer 1 and layer 2. The incident wave is modeled by

$$\vec{u}^i(\vec{r}\,') = u_o \delta(x' - x_o)\delta(y' - y_o)\hat{x} \tag{3.14}$$

where $\vec{r}_o = (x_o, y_o)$ locates the incident wave source in the rectangular coordinate system and u_o is the wave magnitude at r_o. A scattering force, as defined in Eq. (2.34), represented by a global reflection coefficient of the layered structure can be denoted as

$$\vec{f}_s(\vec{r}\,') = m(\vec{r}\,')\vec{u}(\vec{r}\,')\Big|_{\vec{r}\,' = \vec{r}_o} \tag{3.15}$$

where $m(\vec{r}_o)$ is the global reflection coefficient at $\vec{r}_o$. With the Born approximation, the scattered field, as defined in Eq. (2.35), becomes

$$\begin{aligned} \vec{u}^s(\vec{r}) &= \int_V \overleftrightarrow{G}(\vec{r}|\vec{r}\,') \cdot \vec{f}_s(\vec{r}\,')\, dv'\Big|_{\vec{r}\,' = (x_o, y_o, z')} \\ &= f_o \int_{-\infty}^{+\infty} \overleftrightarrow{G}(\vec{r}|x_o, y_o, z') \cdot \hat{x} dz' \end{aligned} \tag{3.16}$$

where $f_o = m(\vec{r}_o)u_o$ represents the force strength. Due to the spectral decomposition of the dyadic Green's function as a superposition of plane waves, a 2-D ultrasonic field can be computed by setting the z component of the field to zero [39]. Thus, the analysis of the backscattered ultrasonic field can be straightforwardly reduced to a 2-D problem.

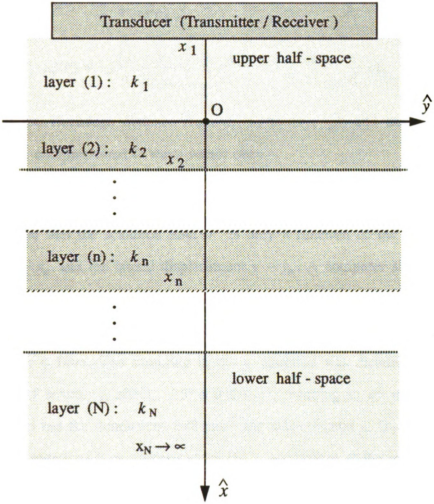

Figure 3.1 : The 2-D backscattering problem to a planar-layered medium.

Since layer 1 is a fluid which supports only compressional C waves, the x and y components of $\vec{u}^s$ become scalar quantities, and they can be written in a more compact form as

$$u_x^s(\vec{r}) = j\frac{f_o}{4}\frac{1}{\omega^2\rho_b}\int_{-\infty}^{\infty} k_x e^{jk_y(y-y_o)} e^{-jk_x(x-x_o)} \frac{1}{R}\, dk_y \quad , \tag{3.17}$$

$$u_y^s(\vec{r}) = -j\frac{f_o}{4}\frac{1}{\omega^2\rho_b}\int_{-\infty}^{\infty} k_y e^{jk_y(y-y_o)} e^{-jk_x(x-x_o)} \frac{1}{R}\, dk_y \quad , \tag{3.18}$$

where R is the Euclidean distance from (x, y) to (x_o, y_o), and the x and y components of the compressional C wave vector obey

$$k_x^2 + k_y^2 = k_o^2 \ . \tag{3.19}$$

It is also noted that the scattered field $\vec{u}^s$ is only a function of the longitudinal displacement $x - x_o$ and the lateral displacement $y - y_o$. A computer simulation gives a 2-D mapping of the modulus of the x component of the scattered field versus the coordinates x and y, is shown in Figure 3.2. The field mapping was sampled in the x direction at $dx = 1mm$. The sampling in the y direction was dictated by an approximated range of scattering effect, $-25° \leq \theta \leq +25°$, resulting in $dy = .5mm$; therefore the area shown has the dimensions 8×8 mm^2 and was centered at (x_T, y_T) = (-64, 0.0). The same computations were performed for the x component of the scattered field.

These results provide more detailed information about the distribution of the backscattered filed and the optimal position for locating the transducer to gain a higher reflected energy. Using this approach, the backscattered field can be evaluated with a known global reflection coefficient. It is therefore a useful scheme for ultrasonic identification.

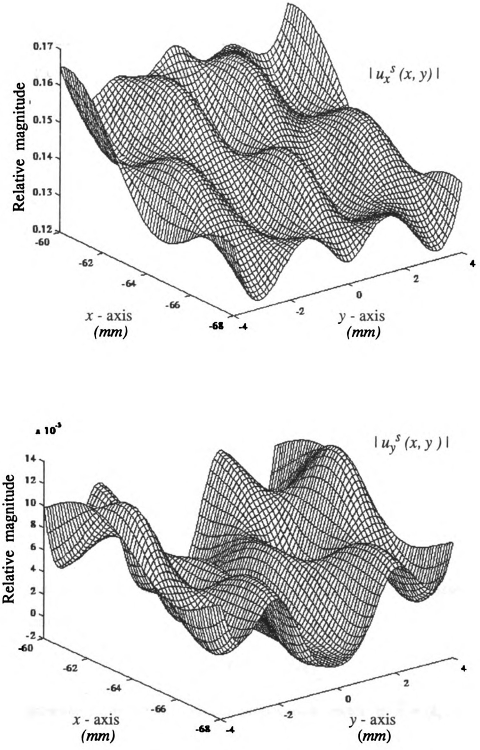

Figure 3.2 : 2-D map of the modulus of the x and y component of the scattered field $|u^s(x,y)|$ versus (x,y) within the region of layer 1.

3.4 Angular - Spectrum Techniques

If the ultrasound scattered field were in a weakly scattering medium, it could be represented by the following convolution

$$u^B(\vec{r}) = \int_V m(\vec{r}\,')u^i(\vec{r}\,')\, G(\vec{r} - \vec{r}\,')dv' \quad , \tag{3.20}$$

where $G(\vec{r} - \vec{r}\,')$ is the Green's function and $u_i(\vec{r})$ is the incident field. Thus Eq. (2.35) can be considered entirely in the angular-spectrum [40]. The plots of Fig. 3.3 will be used to illustrate the various transformations that take place.

Again, considering the effect of a single plane wave illuminating a perfectly layered medium, the backward scattered field can be obtained by using Eq. (3.20).The scattered field can simply be considered as a convolution of the Green function $g(\vec{r} - \vec{r}\,')$ with the product of the surface reflection coefficient $m(\vec{r})$ and the incident field $u^i(\vec{r}\,')$. First, define the following spatial Fourier transform pairs

$$m(\vec{r}) \longleftrightarrow M(\vec{k}) \quad , \tag{3.21a}$$

$$G(\vec{r} - \vec{r}\,') \longleftrightarrow \bar{G}(\vec{k}) \quad , \tag{3.21b}$$

and

$$u(\vec{r}) \longleftrightarrow U(\vec{k}) \quad . \tag{3.21c}$$

The integral solution to the wave equation can now be written in terms of these spatial Fourier transforms or

$$U^s(\vec{k}) = \bar{G}(\vec{k})\left[M(\vec{k}) * U^i(\vec{k})\right] \tag{3.22}$$

where "*" represents convolution, and the propagation vector is $\vec{k} = (k_x, k_y)$. An incident plane wave $u^i(\vec{r})$ can be expressed as

$$U^i(\vec{k}) = 2\pi\delta(\vec{k} - \vec{k}_o) \quad , \tag{3.23}$$

and thus the convolution of Eq. (3.22) becomes a shift in the spatial frequency domain or

$$M(\vec{k}) * U^i(\vec{k}) = 2\pi\, M(\vec{k} - \vec{k}_o) \ . \tag{3.24}$$

This convolution is illustrated in Figures 3.3(a) - (c) for a plane wave propagating with the propagation vector, $\vec{k}_o = (k_o, 0)$. Figure 3.3a shows the spatial Fourier transform of a single cylinder of radius 1 λ, and Figure 3.3b is the spatial Fourier transform of the incident field. The resulting multiplication in the space domain or convolution in the spatial frequency domain is shown in Figure 3.3c.

To find the spatial Fourier transform of the Green's function, the Fourier transform of the equation for a point scatterer

$$\left[\nabla^2 + k_o^2\right] G(\vec{r}|\vec{r}\,') = -\,\delta(\vec{r} - \vec{r}\,') \tag{3.25}$$

is taken to find

$$\left[-k^2 + k_o^2\right] G(\vec{k}|\vec{r}\,') = -\,e^{-j\vec{k}\cdot\vec{r}\,'} \ . \tag{3.26}$$

Rearranging terms the following expression for the Fourier transform of the Green's function is found

$$G(\vec{k}|\vec{r}\,') = \frac{e^{-j\vec{k}\cdot\vec{r}\,'}}{k^2 - k_o^2} \ . \tag{3.27}$$

This expression has a singularity for all $\vec{k}$ such that

$$|\vec{k}|^2 = k_x^2 + k_y^2 = k_o^2 \ . \tag{3.28}$$

An approximation of $G(\vec{k})$ is shown in Fig. 3.3d.

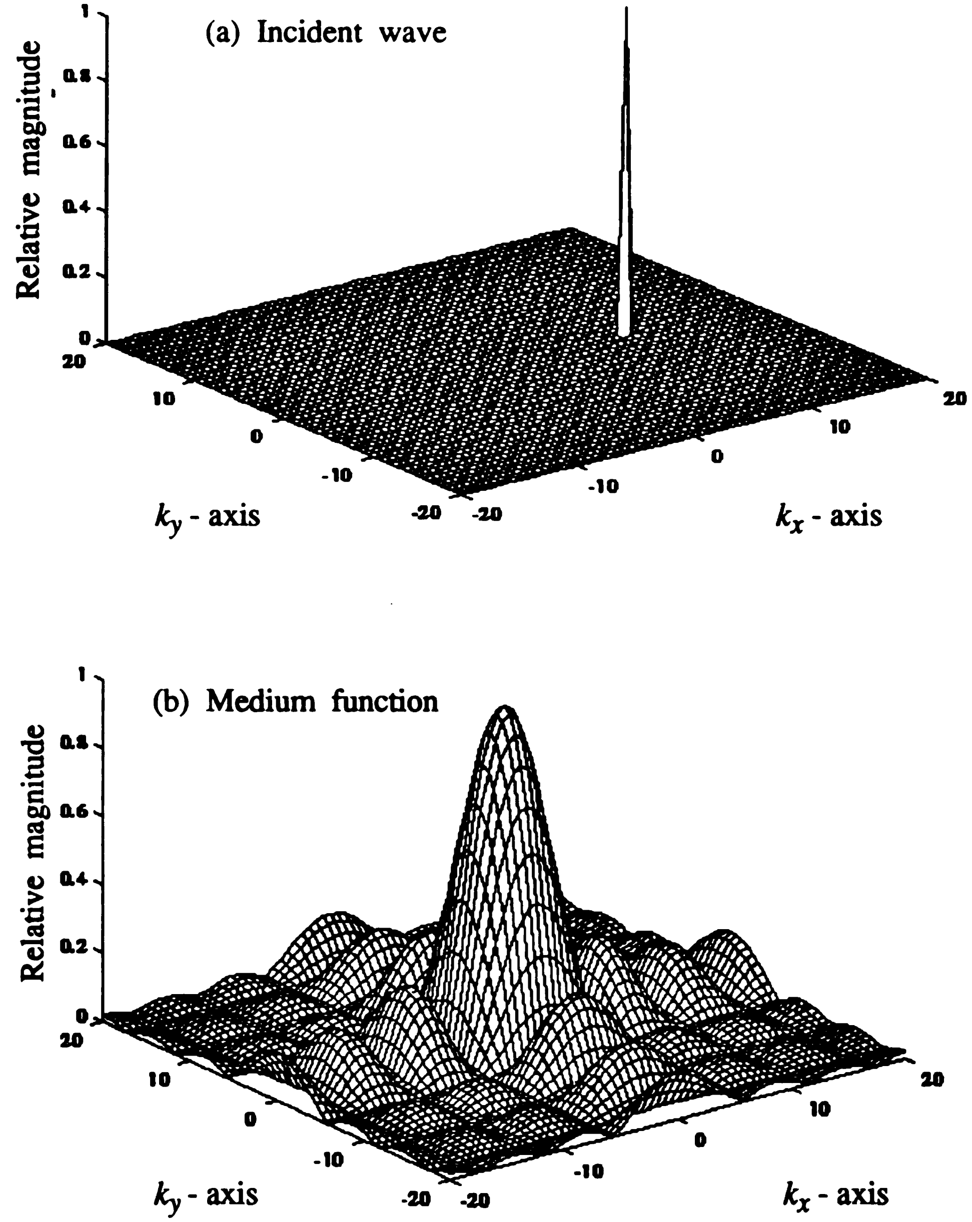

Figure 3.3 : 2-D angular-spectrum representation of the Helmholtz eqn. (a) The incident field $U^i(k)$, (b) The medium function $M(k)$ (c) The spectral convolution $M(k) * U^i(k)$, (d) The Green function $G(k)$, and (e) The scattered field $U^s(k)$.

Figure 3.3 (cont'd)

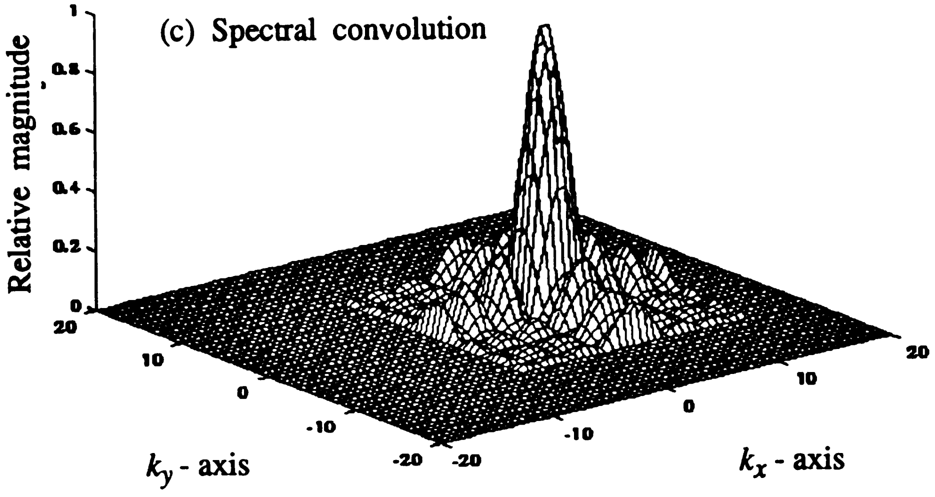
(c) Spectral convolution

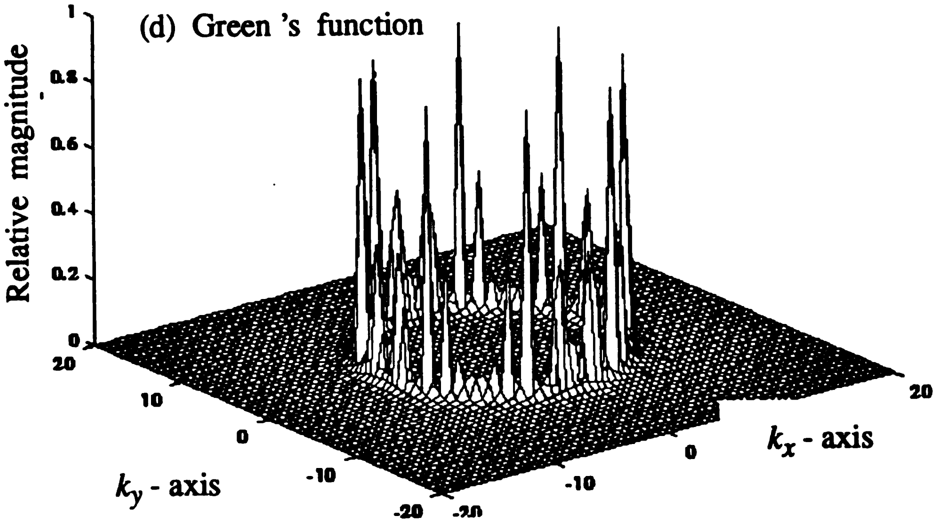
(d) Green 's function

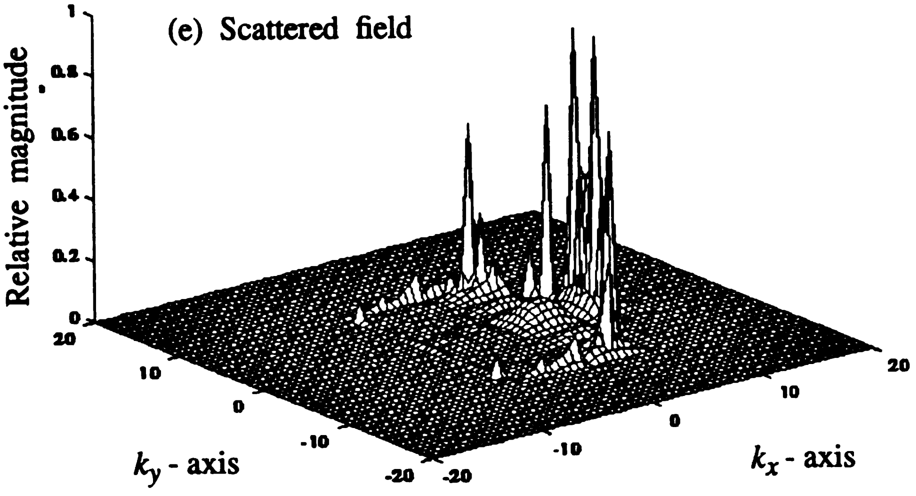
(e) Scattered field

The spatial Fourier transform representation is somewhat misleading since it represents a point scatterer as both a sink and a source of waves. A single plane wave propagating downward can be considered in two different ways depending on the point of view. From the upper side of the scatterer, the point scatterer represents a sink of the wave while to the bottom of the scatterer the wave is spreading from a source point. Later, when our expression for the scattered field is reflected, it will be necessary to choose a solution that leads to backward-propagating waves only.

The effect of the convolution in Eq. (3.20) is a multiplication in the spatial frequency domain of the shifted medium function, Eq. (3.24), and the Green's function, Eq. (3.27), evaluated at $\vec{r}\,' = (0,0)$. The scattered field can be written as

$$U^s(\vec{k}) = 2\pi \frac{M(\vec{k} - \vec{k}_o)}{k^2 - k_o^2} \quad . \tag{3.29}$$

Figure 3.3e shows the results for a plane wave propagating along the x-axis. Since the largest spatial frequency domain components of the Green's function satisfies Eq. (3.28), the spatial Fourier transform of the scattered field is dominated by a shifted and sampled version of the medium's Fourier transform.

An expression for the field at the receiver will now be derived. For simplicity, we will continue to assume that the incident field is propagating along the positive x axis or $\vec{k}_o = (k_o, 0)$. The scattered field along the receiver line $(x = x_o, y)$ is simply the inverse Fourier transform of the field in Eq. (3.29). That is

$$u^s(x = x_o, y) = \frac{1}{4\pi^2} \int_{-\infty}^{\infty} \int_{-\infty}^{\infty} U^s(\vec{k}) e^{j\vec{k}\cdot\vec{r}} dk_x dk_y \tag{3.30}$$

Using Eq. (3.27), this can be expressed as

$$u^s(x = x_o, y) = \frac{1}{4\pi^2} \int_{-\infty}^{\infty} \int_{-\infty}^{\infty} \frac{M(\gamma - k_o, k_y)}{\gamma^2 + k_y^2 - k_o^2} e^{j\vec{k}\cdot\vec{r}} d\gamma dk_y \quad . \tag{3.31}$$

First we carry out the integral form with respect to γ. For a given k_y, the integral has a singularity at

$$\gamma_{1,2} = \pm \sqrt{k_o^2 - k_y^2} \ . \tag{3.32}$$

Using contour integration, the integral can be evaluated with respect to γ. By adding $\frac{1}{2\pi}$ of the residue at each pole, the scattered field becomes

$$u^s(x,y) = \frac{1}{2\pi}\int \Gamma_1(x,k_y)e^{jk_y y}\,dk_y + \frac{1}{2\pi}\int \Gamma_2(x,k_y)e^{jk_y y}\,dk_y \tag{3.33}$$

where

$$\Gamma_1(x,k_y) = \frac{jM(\sqrt{k_o^2 - k_y^2} - k_o, k_y)}{2\sqrt{k_o^2 - k_y^2}}\, e^{j\sqrt{k_o^2 - k_y^2}\, x_o} \tag{3.34a}$$

and

$$\Gamma_2(x,k_y) = \frac{-jM(\sqrt{k_o^2 - k_y^2} - k_o, k_y)}{2\sqrt{k_o^2 - k_y^2}}\, e^{-j\sqrt{k_o^2 - k_y^2}\, x_o} \ . \tag{3.34b}$$

It can be seen that Γ_1 represents the solution in terms of plane waves traveling along the positive x axis, while Γ_2 represents plane waves traveling along the negative x axis.

As discussed earlier, the spatial Fourier transform of the Green's function Eq. (3.27) represents the field due to both a point source and a point sink, but the two solutions are distinct for receiver lines that are outside the extent of the medium. First consider the case in which the scattered field along the line $x = x_o$ is less than that at the x-coordinate of all points in the medium . Since all scattered fields originate in the medium, reflected waves propagating along the negative x axis represent a backward propagating waves while waves propagating along the positive x axis represent waves from a point source. Thus for x 0 (i.e., the receiver is above the medium) the reflected waves are represented by Γ_2 or

$$u^s(x,y) = \frac{1}{2\pi}\int \Gamma_2(x,k_y)e^{jk_y y}\,dk_y \quad , \qquad x < 0 \ . \tag{3.35}$$

Conversely, for a receiver along a line $x = x_o$ where x_o is larger than the x-coordinate of any point in the object, the scattered field is represented by Γ_1 or

$$u^s(x,y) = \frac{1}{2\pi}\int \Gamma_1(x,k_y)e^{jk_y y}\,dk_y \quad , \qquad x > x_{medium} \quad , \tag{3.36}$$

where x_{medium} represents the physical thickness of the layered structure. In general, the scattered field can be written as

$$u^s(x,y) = \frac{1}{2\pi}\int \Gamma(x,k_y)e^{jk_y y}\,dk_y \quad , \tag{3.37}$$

where it is understood that sign of the square root in the expression for Γ should be chosen so that only reflecting waves result.

Taking the spatial Fourier transform of both sides of Eq. (3.37), the spatial Fourier transform of the scattered field at the receiver line is

$$\int u^s(x = x_o, y)e^{-jk_y y}\,dy = \Gamma(x_o,k_y) \ . \tag{3.38}$$

Judging from Eqs. (3.34a) and (3.34b), $\Gamma(x_o,k_y)$ is a phase shifted version of the medium function. The Fourier transform of the scattered field along the line $x = x_o$ is related to the Fourier transform of the medium along a circular arc. The use of the contour integration is further justified by noting that only those waves that satisfy the relationship

$$k_x^2 + k_y^2 = k_o^2 \tag{3.39}$$

will be propagated, thus it is safe to ignore all waves not on the k_o-circle.

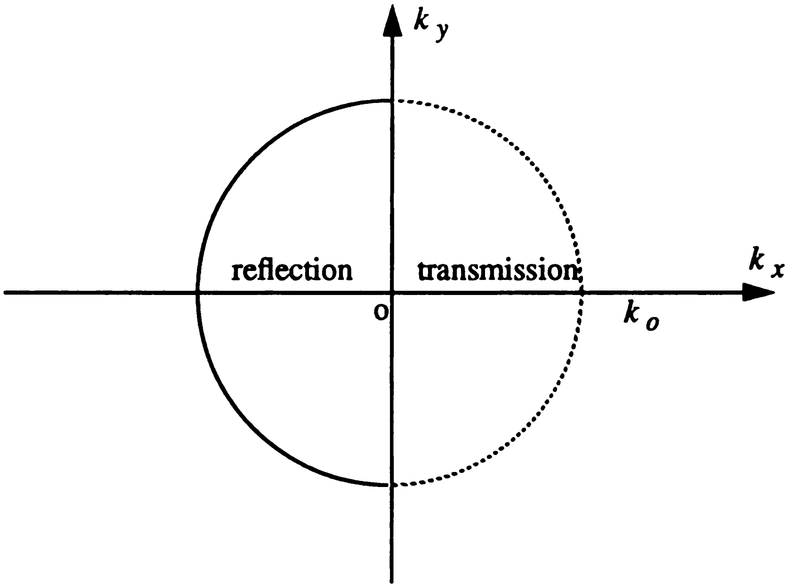

Figure 3.4 : Estimates of the two-dimensional transform of the scatterer are available along the solid arc for reflection propagation and the dashed arc for transmission propagation.

This result is depicted in Figure 3.4. The circular arc represents the locus of all points (k_x, k_y) such that $k_y = \pm\sqrt{k_o^2 - k_x^2}$. The solid line shows the incoming waves for a receiver line at $x = x_o$ above the medium. This can be considered reflection identification. Conversely, the dashed line indicates the locus of solutions for the transmission case.

3.5 IPM Representation of the Layered Structure

The *inverse problem method* (IPM) is an identification technique first formalized by T. K. Sarkar in 1981 for distinguishing the radar target from the complicated scattered field which corresponds uniquely to the individual target [41]. However, its basis is founded in the results of theoretical analysis (see [42 - 44] for examples) which revealed that the scattering field of such an approach is dependent on its geometry and material properties.

Later developments in the area of IPM have generally taken one of two directions. Many researchers have investigated the theoretical implications of the method [45 - 47], including the proper expansion of the system responses, while others have employed the method for the analysis of particular ultrasonic problems [48 - 49]. This section will present the theoretical approaches to the IPM technique. These will form the basis for an ultrasonic material identification method which will be investigated extensively in later chapters.

3.5.1 Determination of the Wave Transmission Matrix

In general, the ultrasound wave scattered by a planar layered structure results from the surface force induced by the incident wave, is shown in Figure 3.5. Systematic evidence suggests that the surface force can be represented as a wave reflection and transmission problem by a *wave transmission matrix* (WTM).

Let us consider a plane ultrasound wave which is arriving at a planar interface, as shown in Figure 3.5, at some arbitrary angle. We denote the downward wave D^i as the incident wave from above and the upward wave U^i as the back-scattered wave.

In order to find the reflection and transmission coefficients at the interface, it suffices to assume the total resultant field is represented by

$$U_1 = R_1 D_1 + T_{21} U_2 \tag{3.40a}$$

and

$$D_2 = T_{12} D_1 + R_2 U_2 \tag{3.40b}$$

where the corresponding reflection and transmission coefficients are defined as

$$R_1 = \left.\frac{U_1}{D_1}\right|_{U_2=0} , \quad T_{12} = \left.\frac{D_2}{D_1}\right|_{U_2=0} , \tag{3.41a}$$

$$R_2 = \left.\frac{D_2}{U_2}\right|_{D_1=0} , \quad T_{21} = \left.\frac{U_1}{U_2}\right|_{D_1=0} . \tag{3.41b}$$

After rearranging, Eq. (3.40b) becomes

$$D_1 = \frac{1}{T_{12}} D_2 - \frac{R_2}{T_{12}} U_2 = \frac{1}{T_{12}} \left[D_2 - R_2 U_2 \right] . \tag{3.42a}$$

With this relationship, Eq. (3.14a) can be rewritten as

$$\begin{aligned} U_1 &= \frac{1}{T_{12}} \left[R_1 D_2 - R_1 R_2 U_2 \right] + T_{21} U_2 \\ &= \frac{1}{T_{12}} \left[R_1 D_2 + \left[T_{12} T_{21} - R_1 R_2 \right] U_2 \right] . \end{aligned} \tag{3.42b}$$

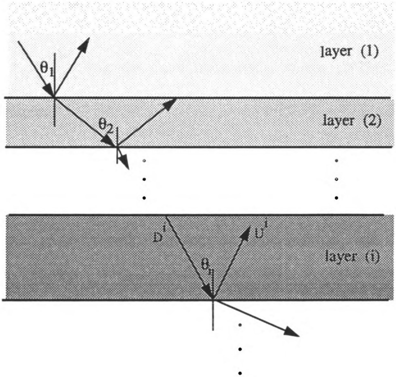

Figure 3.5 : The problem of the reflection and refraction of a plane wave off a layered structure.

Resulting from the reflection and transmission at the interface, two waves exist inside the upper layer with different directions of propagation. As a result, the expression for the ultrasound wave, in the layer can be put in the following form

$$\begin{bmatrix} D_1 \\ U_1 \end{bmatrix} = \frac{1}{T_{12}} \begin{bmatrix} 1 & -R_2 \\ R_1 & \left(T_{12}T_{21} - R_1R_2\right) \end{bmatrix} \begin{bmatrix} D_2 \\ U_2 \end{bmatrix} = \begin{bmatrix} W_{11} & W_{12} \\ W_{21} & W_{22} \end{bmatrix} \begin{bmatrix} D_2 \\ U_2 \end{bmatrix} \tag{3.43}$$

where $\begin{bmatrix} W \end{bmatrix} = \begin{bmatrix} W_{11} & W_{12} \\ W_{21} & W_{22} \end{bmatrix}$ is the wave transmission matrix (WTM). Two cases of WTM are of interest:

Case A : Two half-space layers

Figure 3.6 shows there are only two unbound half-spaces, namely the upper space 1 and the lower space 2, with their acoustic impedances Z_1 and Z_2 respectively. Assuming the downward wave D_1 and upward wave U_2 have unity strength, the reflection and transmission coefficients are related by

$$1 + R_1 = T_{12} \tag{3.44a}$$

$$1 + R_2 = T_{21} \ . \tag{3.44b}$$

The reflection coefficients are defined as

$$R_1 = \frac{Z_2 - Z_1}{Z_2 + Z_1} \quad \text{and} \quad R_2 = \frac{Z_1 - Z_2}{Z_1 + Z_2} \ . \tag{3.45}$$

where $Z_i = \dfrac{\rho_i \upsilon_{ci}}{\cos\theta_i}$ is the impedance of the i^{th} medium, θ_i is the incident angle at the i^{th} interface, ρ_i and υ_{ci} are the density and wave velocity in the i^{th} medium respectively. Since $R_2 = -R_1$, the elements of the matrix $\begin{bmatrix} W \end{bmatrix}$ can then be expressed as

$$W_{11} = \frac{1}{T_{12}} = \frac{1}{1 + R_1} = \frac{Z_2 + Z_1}{2Z_2} \ , \tag{3.46a}$$

$$W_{12} = \frac{-R_2}{T_{12}} = \left[\frac{Z_2 - Z_1}{Z_2 + Z_1}\right]\left[\frac{Z_2 + Z_1}{Z_2}\right] = \frac{Z_2 - Z_1}{Z_2} \quad , \tag{3.46b}$$

$$W_{21} = \frac{R_1}{T_{12}} = W_{12} \quad , \tag{3.46c}$$

and

$$W_{22} = \frac{T_{12}T_{21} - R_1R_2}{T_{12}} = \frac{\left[1 + R_1\right]\left[1 + R_2\right] - R_1R_2}{T_{12}} = \frac{1}{T_{12}} \quad . \tag{3.46d}$$

Two half-space layers, the WTM can simply be represented as

$$\left[W\right] = \frac{1}{T_{12}}\begin{bmatrix} 1 & R_1 \\ R_1 & 1 \end{bmatrix} \quad . \tag{3.47}$$

Case B : Finite length of an unbound medium

For waves propagating through a finite length of medium, as depicted in Figure 3.7, the downward-going wave and upward-going wave are

$$D_2 = D_1 e^{-jkx_{21}} \tag{3.48a}$$

$$U_2 = U_1 e^{jkx_{21}} \tag{3.48b}$$

where $kx_{21} = 2\pi\frac{x_{21}}{\lambda_c}$, λ_c is the wavelength of acoustic wave in the i^{th} medium and x_{21} is the physical distance between point x_1 and x_2. Thus one can define WTM, for a finite length of an unbound medium, as

$$\left[W\right] = \begin{bmatrix} e^{jkx_{21}} & 0 \\ 0 & e^{-jkx_{21}} \end{bmatrix} \quad . \tag{3.49}$$

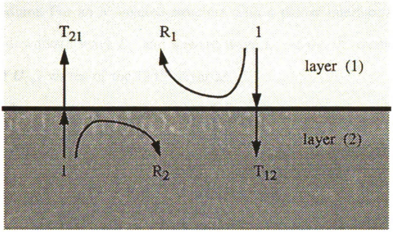

Figure 3.6 : Configuration for two half-space layers.

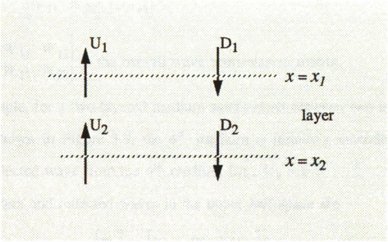

Figure 3.7 : Configuration for an unbound layer with finite length.

Finally, by using the WTM technique, one can obtain the expression of the reflected wave which is excited by an incident wave as it hits a layered structure of a differing medium. For an N-layered structure with a planar interface as shown in Figure 3.8, the downward wave D_i and upward wave U_i of the i^{th} medium are related to the D_{i+1} and U_{i+1} waves of the $i+1^{th}$ layer as

$$\begin{bmatrix} D_i \\ U_i \end{bmatrix} = \frac{1}{T_i} \begin{bmatrix} 1 & R_i \\ R_i & 1 \end{bmatrix} \begin{bmatrix} e^{jk_i x_1} & 0 \\ 0 & e^{-jk_i x_i} \end{bmatrix} \begin{bmatrix} D_{i+1} \\ U_{i+1} \end{bmatrix} \quad ; \; 1 \le i \le N \tag{3.50}$$

$$= \frac{1}{T_i} \begin{bmatrix} e^{jk_i x_i} & R_i e^{-jk_i x_i} \\ R_i e^{jk_i x_i} & e^{-jk_i x_i} \end{bmatrix} \begin{bmatrix} D_{i+1} \\ U_{i+1} \end{bmatrix}$$

where k_i and x_i are the wave number and thickness of the i^{th} medium, respectively. Using algebraic operations, the overall system becomes

$$\begin{bmatrix} D_1 \\ U_1 \end{bmatrix} = \prod_{i=1}^{N} \frac{1}{T_i} \begin{bmatrix} e^{jk_i x_i} & R_i e^{-jk_i x_i} \\ R_i e^{jk_i x_i} & e^{-jk_i x_i} \end{bmatrix} \begin{bmatrix} D_{i+1} \\ U_{i+1} \end{bmatrix} \tag{3.51}$$

$$= \begin{bmatrix} W_{11} & W_{12} \\ W_{21} & W_{22} \end{bmatrix} \begin{bmatrix} D_{N+1} \\ U_{N+1} \end{bmatrix}$$

where $\begin{bmatrix} A \end{bmatrix} = \begin{bmatrix} W_{11} & W_{12} \\ W_{21} & W_{22} \end{bmatrix}$ is the overall wave transmission matrix.

For example, for a two-layered medium sandwiched between two half-space backgrounds, as shown in Figure 3.9, the 4^{th} medium is infinitely extended. As a result, there is no reflected wave from the 4^{th} medium (i.e., $U_4 = 0$).

The incident and reflected waves in the upper half-space are

$$\begin{bmatrix} D_1 \\ U_1 \end{bmatrix} = \begin{bmatrix} W_{11} & W_{12} \\ W_{21} & W_{22} \end{bmatrix} \begin{bmatrix} D_4 \\ U_4 \end{bmatrix} \Bigg|_{U_4 = 0} \tag{3.52}$$

where $\begin{bmatrix} W_{11} & W_{12} \\ W_{21} & W_{22} \end{bmatrix} = \prod_{i=1}^{3} \frac{1}{T_i} \begin{bmatrix} e^{jk_i x_i} & R_i e^{-jk_i x_i} \\ R_i e^{jk_i x_i} & e^{-jk_i x_i} \end{bmatrix}$.

Therefore, the surface reflection ratio $m(\vec{r})$ at interface 1 (i.e., $x = 0$) is then

$$
\begin{aligned}
m(x = 0) = \left.\frac{U_1}{D_1}\right|_{U_4 = 0} &= \frac{W_{21}}{W_{11}} \qquad (3.53) \\
&= \frac{R_1\left(1 + R_2 R_3 e^{-j2k_3x_3}\right) + e^{-j2k_2x_2}\left(R_2 + R_3 e^{-j2k_3x_3}\right)}{\left(1 + R_2 R_3 e^{-j2k_3x_3}\right) + R_1 e^{-j2k_2x_2}\left(R_2 + R_3 e^{-j2k_3x_3}\right)} \\
&= R_1 + R_2\left(1 - R_1^2\right)e^{-j2k_2x_2} + R_3\left(1 - R_1^2\right)\left(1 - R_2^2\right) \\
&\quad \cdot e^{-j2\left(k_2x_2 + k_3x_3\right)} + \cdots \; .
\end{aligned}
$$

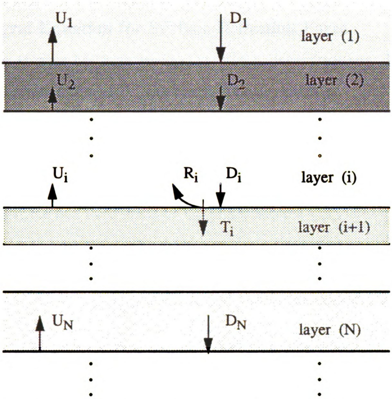

Figure 3.8 : Cascaded system of a planar *N*-layered medium.

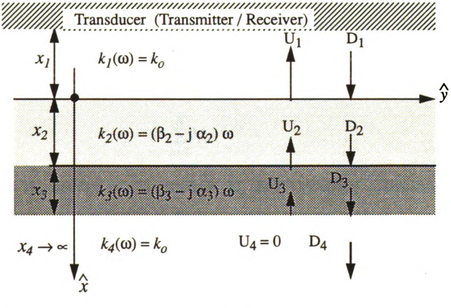

Figure 3.9 : The ultrasonic schematic diagram for a two-layered medium embedded in a fluid background.

3.5.2 Integral Equation for Surface Reflection Force

The wave number has been assumed to have a linear frequency dependency, the complex wave number of the n^{th} layer can then be expressed as

$$k_n(\omega) = \left[\beta_n - j\alpha_n\right]\omega \tag{3.54}$$

where β_n and α_n are the propagation and attenuation constants of the n^{th} layer respectively. Therefore, the first three terms of Eq. (3.53) become

$$\begin{aligned} m(\omega) &= R_1 + R_2\left[1 - R_1^2\right]e^{-j2(\beta_2 - j\alpha_2)\omega x_2} \\ &\quad + R_3\left[1 - R_1^2\right]\left[1 - R_2^2\right]e^{-j2[(\beta_2 - j\alpha_2)\omega x_2 + (\beta_3 - j\alpha_3)\omega x_3]} \\ &= M_1 e^{-(\sigma_1 + j\nu_1)\omega} + M_2 e^{-(\sigma_2 + j\nu_2)\omega} + M_3 e^{-(\sigma_3 + j\nu_3)\omega} \end{aligned} \tag{3.55}$$

where $M_1 = R_1$, $M_2 = R_2\left[1 - R_1^2\right]$, $M_3 = R_3\left[1 - R_1^2\right]\left[1 - R_2^2\right]$, $\sigma_1 + j\nu_1 = 0 + j0$, $\sigma_2 + j\nu_2 = 2\alpha_2 x_2 + j2\beta_2 x_2$, and $\sigma_3 + j\nu_3 = 2\left[\beta_2 x_2 + \beta_3 x_3\right] + j2\left[\alpha_2 x_2 + \alpha_3 x_3\right]$. This result suggests that the surface reflection coefficient of an N-layered structure can be represented in the frequency domain by the sum of the natural mode functions as

$$\begin{aligned} m(\vec{r}_o, \omega) &= \sum_{n=1}^{N} M_n e^{-\sigma_n \omega} e^{-j\nu_n \omega} \\ &= \sum_{n=1}^{N} M_n e^{\tau_n \omega} \end{aligned} \tag{3.56}$$

where N is the number of the interface, M_n is the coupling coefficient of the n^{th} mode, and $\tau_n = -\sigma_n - j\nu_n$ is the n^{th} complex natural mode factor.

Practically, a pulsed ultrasound field can be expressed as

$$\vec{u}(\vec{r}, t) = \begin{cases} \vec{u}(\vec{r})e^{j\omega_c t} & ; \quad |t| \le \dfrac{\Delta t}{2} \\ 0 & ; \quad |t| > \dfrac{\Delta t}{2} \end{cases} \tag{3.57}$$

where Δt is the time duration of the pulse and ω_c is the harmonic frequency of the ultrasound wave. Figure 3.10 shows the spectral distribution of a pulsed ultrasound wave. The spectrum of this pulsed field can be written as

$$\vec{u}(\vec{r},\omega) = \int_{-\infty}^{\infty} \vec{u}(\vec{r},t)e^{-j\omega t}\,dt = \int_{-\Delta t/2}^{\Delta t/2} \vec{u}(\vec{r})e^{-j(\omega-\omega_c)t}\,dt \tag{3.58}$$

$$= \frac{j\,\vec{u}(\vec{r})}{\omega-\omega_c}\left[e^{-j(\omega-\omega_c)\frac{\Delta t}{2}} - e^{j(\omega-\omega_c)\frac{\Delta t}{2}}\right]$$

$$= \vec{u}(\vec{r})\frac{2\sin\left[(\omega-\omega_c)\frac{\Delta t}{2}\right]}{\omega-\omega_c} \quad .$$

For a narrow pulse, the following approximation is valid,

$$\frac{\sin\left[(\omega-\omega_c)\frac{\Delta t}{2}\right]}{(\omega-\omega_c)\frac{\Delta t}{2}} \approx 1 \quad , \quad \left|\omega-\omega_c\right| \le \frac{2\pi}{\Delta t} \quad , \tag{3.59}$$

Finally, the surface reflection force becomes

$$\vec{f}_s(\vec{r}_o,\omega) = m(\vec{r},\omega)\vec{u}(\vec{r},\omega)\delta(\vec{r}-\vec{r}_o) \tag{3.60}$$

$$= \left[\sum_{n=1}^{N} M_n e^{\tau_n\omega}\right]\vec{u}(\vec{r}_o)\frac{2\sin\left[(\omega-\omega_c)\frac{\Delta t}{2}\right]}{\omega-\omega_c}$$

$$\approx \left[\sum_{n=1}^{N} M_n e^{\tau_n\omega}\right]\vec{u}(\vec{r}_o)$$

$$= \sum_{n=1}^{N} M_n \vec{f}_n(\vec{r}_o)e^{\tau_n\omega} \quad , \quad \left|\omega-\omega_c\right| \le \frac{2\pi}{\Delta t} \quad ,$$

where $\vec{f}_n(\vec{r}_o) = \vec{u}(\vec{r}_o)\Delta t$ is the spatial force distribution.

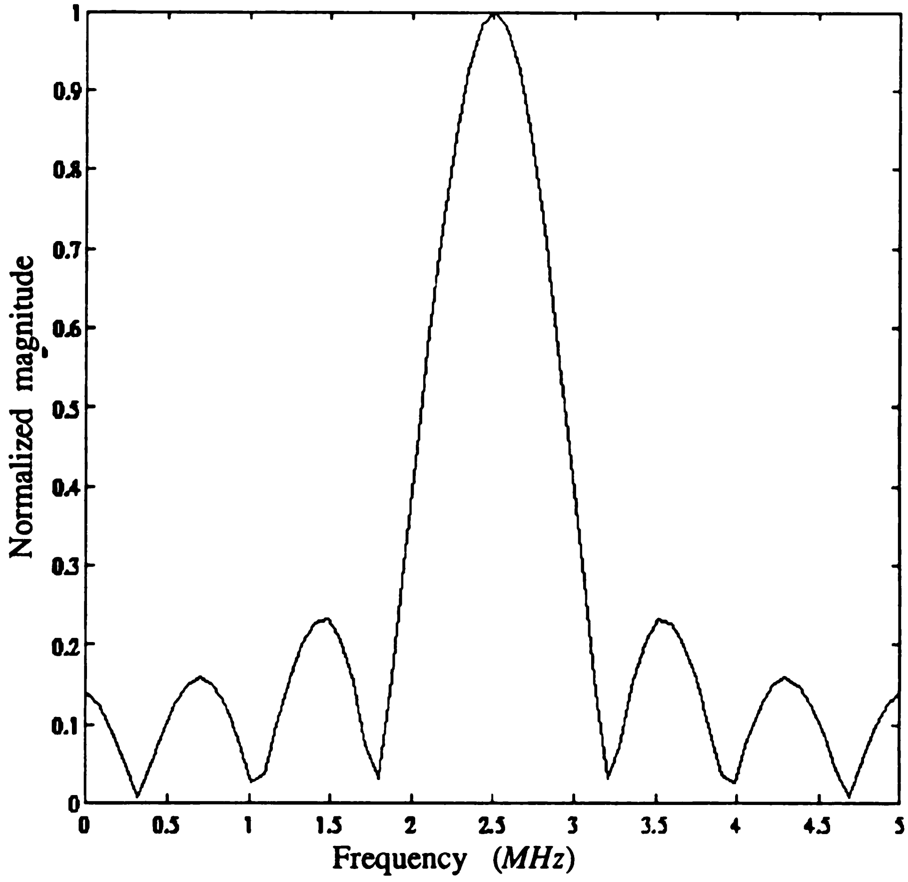

Figure 3.10 : The spectral ditribution of a pulsed ultrasound wave.

Evaluation of the steady-state scattered field excited by the induced surface reflection force can be simplified greatly by the use of a transform domain analysis. The z-transform of a discrete function $h(n)$ is defined as [50]

$$H(z) = Z\left\{h(n)\right\} = \sum_{n=0}^{\infty} h(n) z^{-n} \tag{3.61}$$

and the corresponding inverse transform is

$$h(n) = Z^{-1}\left\{H(z)\right\} = \frac{1}{2\pi j}\oint H(z) z^{n-1}\, dz \tag{3.62}$$

where the inversion integral is performed over the closed contour in the region of convergence of $H(z)$, and $h(n)$ is taken to be a causal function. If the l^{th} frequency sample in the specified band, $\omega_1 = \omega_c - \frac{2\pi}{\Delta t} \le \omega_l \le \omega_c + \frac{2\pi}{\Delta t} = \omega_2$, is denoted as

$$\omega_l = \omega_1 + l\Delta\omega \ , \qquad 0 \le l \le L-1 \ , \tag{3.63}$$

where $\Delta\omega = \frac{\omega_2 - \omega_1}{L} \le \frac{\pi}{\tau_{\max}}$, $\tau_{\max} = \max\left\{|\tau_1|, |\tau_2|, \cdots, |\tau_N|\right\}$, and L is the total number of samples, then the discrete form of the surface reflection force can be denoted as

$$\begin{aligned} \vec{f}_s(\vec{r}_o, l) = \vec{f}_s(\vec{r}_o, \omega_l) &= \sum_{n=1}^{N} M_n \vec{f}_n(\vec{r}_o) e^{(\omega_1 + l\Delta\omega)\tau_n} \\ &= \sum_{n=1}^{N} M'_n(z_n) \vec{f}_n(\vec{r}_o) z_n^l \ , \qquad 0 \le l \le L-1 \end{aligned} \tag{3.64}$$

where $z_n = e^{\Delta\omega\tau_n}$ and $M'_n(z_n) = M_n e^{\omega_1\tau_n}$. Transforming these frequency samples into the z-domain, the surface reflection force becomes

$$\vec{f}_s(\vec{r}_o, z) = \sum_{n=1}^{N} M'_n(z_n) \vec{f}_n(\vec{r}_o) \frac{z}{z - z_n} \ . \tag{3.65}$$

Thus, the steady-state reflection force is the sum of simple singular poles in the complex z-plane. For layered structures, the natural modes occur in N complex parameters, and it can easily be seen that the application of the inverse transform Eq. (3.62) and Cauchy's residue theorem returns Eq. (3.65) to the spectral form of Eq. (3.60).

The fundamental assumption of inverse problem method analysis is that Eq. (3.65) is a valid transform domain representation of the surface reflection force in the steady-state. That is, there exist no contributions due to higher-order poles, and it is important to stress that this representation is valid in the steady-state only.

Employing the bandpass concept, Eq. (2.33) results in the transform domain expression for the reflected ultrasound field maintained by the induced surface reflection force

$$\begin{aligned} \vec{u}^{\,r}(\vec{r},z) &= \int_S \overleftrightarrow{G}(\vec{r}|\vec{r}\,')\cdot\vec{f}_s(\vec{r}\,',z)\,ds' \\ &= \sum_{n=1}^{N} M'_n(z_n)\frac{z}{z-z_n}\int_S \overleftrightarrow{G}(\vec{r}|\vec{r}\,')\cdot\vec{f}_n(\vec{r}\,')\,ds' \ . \end{aligned} \tag{3.66}$$

After the inverse transform, the IPM representation of the reflected ultrasonic field is given by

$$\vec{u}^{\,r}(\vec{r},l) = \sum_{n=1}^{N} M'_n(z_n)z_n^l \int_S \overleftrightarrow{G}(\vec{r}|\vec{r}\,')\cdot\vec{f}_n(\vec{r}\,')\,ds' \quad ; \quad 0 \le l \le L-1 \ , \tag{3.67}$$

or denoting

$$\omega_l = \omega_1 + l\Delta\omega \quad ; \quad 0 \le l \le L-1 \ , \tag{3.68}$$

the reflected field can be expressed in the frequency domain as

$$\vec{u}^{\,r}(\vec{r},\omega) = \sum_{n=1}^{N} M_n e^{\omega\tau_n} \int_S \overleftrightarrow{G}(\vec{r}|\vec{r}\,')\cdot\vec{f}_n(\vec{r}\,')\,ds' \quad ; \quad \omega_1 \le \omega \le \omega_2 \ . \tag{3.69}$$

Before Eq. (3.69) can be used to evaluate the reflected field, the surface reflection force estimated by the incident field must be determined. This requires the calculation of the natural modes and coupling coefficients, all of which are included in the Eq. (3.65). As mentioned earlier, the natural modes are closely related to the properties and physical dimension of the medium, while the coupling coefficients are strong functions of interface reflectivity.

The surface reflection force can be determined through the use of the solution to an ultrasound field integral equation (UFIE). The reason is that the function of the ultrasound field equation is based on the boundary condition on the surface of the perfectly layered structure. The boundary condition is

$$\hat{t}\cdot\vec{u}^{\,i}(\vec{r},z) = \hat{t}\cdot\vec{u}^{\,r}(\vec{r},z) \tag{3.70}$$

where $\hat{t}$ is the tangential unit vector. Writing the reflected field as in Eq. (3.70) yields the UFIE

$$\sum_{n=1}^{N} M'_n(z_n)\frac{z}{z-z_n}\int_S \hat{t}\cdot\overleftrightarrow{G}(\vec{r}|\vec{r}\,')\cdot\vec{f}_n(\vec{r}\,')\,ds' = \hat{t}\cdot\vec{u}^{\,i}(\vec{r},z) \tag{3.71}$$

which must hold for all points on the surface of the target. Since the incident field is finite, the possible solutions to the resulting equation represent the natural modes of the medium (i.e., there are solutions to the UFIE only at each discrete pole $z = z_n$).

$$\lim_{z\to z_n} M'_n(z_n)\frac{z}{z-z_n}\int_S \hat{t}\cdot\overleftrightarrow{G}(\vec{r}|\vec{r}\,')\cdot\vec{f}_n(\vec{r}\,')\,ds' = \hat{t}\cdot\vec{u}^{\,i}(\vec{r},z_n)\ . \tag{3.72}$$

Replacing the normal unit vector $\hat{t}$ with $\int_S \vec{f}_m^{\,*}(\vec{r})\,ds'$, where $\vec{f}_m^{\,*}(\vec{r})$ is the conjugate force distribution of the m^{th} mode, and utilizing the symmetry property of the dyadic Green's function, then taking the limit $z_n \to z_m$ and l'Hospital's rule to Eq. (3.72), the coupling coefficients become

$$M'_m(z_m) = \frac{1}{d_m}\int_S \vec{u}^{\,i}(\vec{r}\,',z_m)\cdot\vec{f}_m(\vec{r}\,')\,ds' \tag{3.73}$$

where d_m is a normalization coefficient and is given by

$$d_m = \int_S ds\vec{f}_m^{\,*}(\vec{r})\cdot\int_S \overleftrightarrow{G}(\vec{r}|\vec{r}\,')\cdot\vec{f}_m(\vec{r}\,')\,ds' \ . \tag{3.74}$$

Replacing z_m by z, the coupling coefficients can be put in terms of the z-domain parameter.

$$M'_n(z) = \frac{1}{d_n}\int_S \vec{u}^{\,i}(\vec{r}\,',z)\cdot\vec{f}_n(\vec{r}\,')\,ds' \ . \tag{3.75}$$

3.5.3 Spectral Representation of the Reflected Field

In most of the ultrasonic imaging applications, it can be assumed that the target is in the far-zone field region. Thus, the incident ultrasonic pulse is a component of a Gaussian wave front, or

$$\vec{u}^{\,i}(\vec{r},\omega) = \hat{k}\ u_i(\omega)e^{-jkr} \quad , \quad \omega_1 \le \omega \le \omega_2 \ , \tag{3.76}$$

where $\hat{k}$ determines the polarization of the ultrasonic field, and $u_i(\omega)$ describes the temporal variation of the field. Transforming this to the z domain via Eq. (3.62) yields

$$\vec{u}^{\,i}(\vec{r},z) = \hat{k}\ u_i(z)e^{-jkr} \ . \tag{3.77}$$

Substituting Eq. (3.77) into Eq. (3.75) and making use of Eq. (3.66), it gives the spectral representation of the reflected field as

$$\vec{u}^{\,r}(\vec{r},l) = \sum_{n=1}^{N}\frac{u_i(z_n)}{d_n}z_n^l\left[\int_S e^{-jkr'}\hat{k}\cdot\vec{f}_n(\vec{r}\,')ds'\right] \tag{3.78}$$

$$\times\left[\int_S \overleftrightarrow{G}(\vec{r}|\vec{r}\,')\cdot\vec{f}_n(\vec{r}\,')ds'\right] \quad , \quad 0 \le l \le L \ .$$

This reflected field in the frequency domain can be written as

$$\vec{u}^{\,r}(\vec{r},\omega) = \sum_{n=1}^{N} U'_n(\vec{r})e^{j\theta_n(\vec{r})}e^{\tau_n\omega} \quad ; \quad \omega_1 \leq \omega \leq \omega_2 \ , \tag{3.79}$$

where $U'_n(\vec{r})e^{j\theta_n(\vec{r})} = \dfrac{u_i(z_n)}{d_n}\left[\int_S e^{-jkr'}\hat{k}\cdot\vec{f}_n(\vec{r}\,')ds'\right]\times\left[\int_S \overleftrightarrow{G}(\vec{r}|\vec{r}\,')\cdot\vec{f}_n(\vec{r}\,')ds'\right]$.

This result reveals that the reflected ultrasonic field also varies, in the frequency domain, as a sum of damped sinusoidal functions. This frequency response of the reflected field will be utilized for ultrasonic identification of layered structures in the following chapters. With the surface reflection force developed, we can further build the framework for evaluating the reflected field of a layered structure using the Born or the Rytov approximation. Moreover, the result is also applicable to the study of inverse problems which provides methods of reconstructing images and detecting material characteristics from the measurements of reflected field of a layered structures buried in a homogeneous surrounding. These issues will be further pursued in Chapter 5.

CHAPTER 4

EXTRACTION OF THE NATURAL MODE FACTORS FROM A MEASURED RESPONSE

4.1 Introduction

The most obvious requirement for the implementation of a layered structure identification scheme based on material feature resonances is the accurate knowledge of the natural mode factors of a wide variety of structures, as addressed in Chapter 3. For most realistic structures, theoretical determination of the natural mode factors is impractical. Thus, it becomes necessary, in some manner, to determine the natural mode factors from a measurement of the reflected response of a layered structure.

This chapter presents a variety of methods for extracting the natural mode factors of a structure from its reflected waveform. Basically, the methods can be divided into four categories. The first involves Prony's method, which is well known and discussed in many fields [51 -53]. This approach has some disadvantages, including a sensitivity to noise [54, 55].

In the second group, the Maximum Likelihood (ML) method [56] and the MUltiple SIgnal Classification (MUSIC) method [57] are discussed. They work best for processes consisting of narrow band and uncorrelated signals in white noise, but involve the high computational load of multivariate nonlinear maximization problems. Because of these factors, these two classes of techniques are not suitable for our research purpose, and other suboptimal techniques are needed.

The last two utilize eigenvalue analysis, solving first for a generalized eigenvalue problem and then extracting the natural mode factors from the exponential polynomial. The matrix pencil method [58, 59] involves reconstructing an autoregressive (AR) model to optimize the performance by subspace decomposition. Our proposed spectral Prony algorithm (SPA) involves evaluating a noncyclic convolution of the measured response and an exponential model.

Each of these techniques will be discussed in detail. Their performance under various circumstances, including the presence of random noise, will be examined for their merits in the applications of material characterization.

4.2 Least Squares Prony Method

The modern least squares (LS) version of exponential fitting problem is considerably different from the original Prony method [60]. This method makes use of a LS analysis to fit an exponential model for cases where there are more data points than needed to fit the assumed number of exponential terms [61].

For practical situations, the number of data points L usually exceeds the minimum number needed to fit a model of N exponentials, *i.e.*, $L > 2N$. In this overdetermined case, the data sequence can only be approximated as an exponential sequence,

$$u^s(l) = \hat{u}(l) = \sum_{n=1}^{N} h_n z_n^l \quad ; \quad 0 \le l \le L-1 \ , \tag{4.1}$$

where the coupling parameters h_n and natural modes z_n, from Eq. (3.67), are defined as

$$h_n = M'_n \int_S \overleftrightarrow{G}(\vec{r}\,|\,\vec{r}\,') \cdot \vec{f}_n(\vec{r}\,')\, ds' \tag{4.2a}$$

$$= A_n e^{j\theta_n}$$

and

$$z_n = e^{-(\sigma_n + j\nu_n)\Delta\omega} = e^{\tau_n \Delta\omega} \; . \tag{4.2b}$$

In denoting the approximation error as $\varepsilon(l) = u(l) - \hat{u}(l)$, one can find the order N and the parameters $\{h_n, z_n\}$ for $n = 1$ to $n = N$ such that the total squared error

$$\rho = \sum_{l=0}^{L-1} \left| \varepsilon(l) \right|^2 \tag{4.3}$$

is a minimum. This is a difficult nonlinear problem. A suboptimum solution that provides satisfactory results may be obtained with a variant of the original Prony method presented in Appendix A. The least squares approach [62] effectively reduces the nonlinearity of the exponential fitting problem into polynomial problem.

In the overdetermined data case, the linear difference equation (A.7) could be modified to

$$\sum_{n=1}^{N} a_n u(l-n) = e(l) \tag{4.4}$$

for $N + 1 \leq l \leq L - 1$. The term $e(l)$ represents the linear prediction approximation error, in contrast to error $\varepsilon(l)$, which represents the exponential approximation error.

Equation (4.4) is identical to the forward linear prediction error equation. Each a_n term is a linear prediction parameter. Referring to Eq. (A.7), the a_n may be selected such that the linear prediction squared error $\sum_{l=N+1}^{L-1} \left| e(l) \right|^2$ will be minimized. This is simply the covariance method of linear prediction [61]. The number of exponentials N (also called the number of poles in reference to AR processing) may be estimated using the same order selection rules. However, the maximum order is limited to $N \leq L/2$. The roots of the polynomial constructed from the linear prediction coefficients will yield, and the damping and phase factor can be solved from the roots by using Eq. (A.9) and Eq. (A.10).

If $z_1, \cdots, z_N$ have been determined by a LS linear prediction analysis and by polynomial parametering, then the exponential approximation $\hat{u}(l)$ of Eq. (4.1) becomes linear in the remaining unknown coupling parameters $h_1, \cdots, h_N$. Minimizing the squared error with respect to each of the h_n parameters yields the complex-valued $N \times N$ matrix normal equation

$$\left[\mathbf{Z}^H \mathbf{Z}\right] \mathbf{h} = \left[\mathbf{Z}^H \mathbf{u}\right] \tag{4.5}$$

where the superscript ^{H} denotes the Hermitian of a matrix. The $L \times N$ matrix $\mathbf{Z}$, the $N \times 1$ vector $\mathbf{h}$, and $L \times 1$ data vector $\mathbf{u}$ are defined as

$$\mathbf{Z} = \begin{bmatrix} 1 & 1 & \cdots & 1 \\ z_1 & z_2 & \cdots & z_N \\ \vdots & \vdots & & \vdots \\ z_1^{L-1} & z_2^{L-1} & \cdots & z_N^{L-1} \end{bmatrix}, \quad \mathbf{h} = \begin{bmatrix} h_1 \\ h_2 \\ \vdots \\ h_N \end{bmatrix}, \quad \mathbf{u} = \begin{bmatrix} u(0) \\ u(1) \\ \vdots \\ u(L-1) \end{bmatrix}. \tag{4.6}$$

The $N \times N$ Hermitian matrix $\mathbf{Z}^H \mathbf{Z}$ has the form

$$\mathbf{Z}^H \mathbf{Z} = \begin{bmatrix} \gamma_{11} & \cdots & \gamma_{1N} \\ \vdots & & \vdots \\ \gamma_{N1} & \cdots & \gamma_{NN} \end{bmatrix}, \tag{4.7}$$

where

$$\gamma_{jk} = \sum_{l=0}^{L-1} \left[z_j^* z_k \right]^l = \gamma_{kj}^* \quad . \tag{4.8}$$

A useful relationship that avoids the summation of Eq. (4.8) is

$$\begin{aligned} \gamma_{jk} &= \frac{\left[z_j^* z_k \right]^L - 1}{\left[z_j^* z_k \right] - 1} && \text{if } z_j^* z_k \neq 1 \\ &= \quad L && \text{if } z_j^* z_k = 1 \quad . \end{aligned} \tag{4.9}$$

Then the unknown h_n parameters can be solved using Eq. (4.5).

The LS Prony method will also fit exponentials to any additive noise present in the data because the exponential model does not make a separate estimate of the noise process. An exponential model incorporating additive noise would have the form

$$u(l) = \sum_{n=1}^{N} h_n z_n^l + \varepsilon(l) \quad , \qquad l = 0, 1, \cdots, L-1 \quad . \tag{4.10}$$

The function $\varepsilon(l)$ has also been used to represent the approximation error of the exponential model. If $u(l) - \varepsilon(l)$ is used in place of $u(l)$ in the analysis of Appendix A, then the linear difference equation becomes

$$u(l) = - \sum_{n=1}^{N} a_n u(l-n) + \sum_{n=0}^{N} a_n \varepsilon(l-n) \quad . \tag{4.11}$$

This is an autoregressive-moving average (ARMA) model with identical AR(N) and MA(N) coefficients and a driving noise process $\varepsilon(l)$. The first step of the LS Prony method uses the linear predication

$$u(l) = - \sum_{n=1}^{N} a_n u(l-n) + e(l) \tag{4.12}$$

and to whiten $e(l)$. Comparing Eq. (4.12) with (4.11), the whitened process $e(l)$ does not correspond well to the nonwhite MA process represented by $\sum_{n=0}^{N} a_n \varepsilon(l-n)$. It is for this reason that the LS Prony method does not often perform well in the presence of significant additive noise; it fails to account for nonwhite noise in the process. When the LS Prony estimation method is performed in the presence of significant additive noise, the attenuation terms are significantly misestimated. They often are estimated higher than they actually are [63].

4.3 Maximum Likelihood Method

In this section, we derive the Maximum Likelihood (ML) estimation of the coupling parameters and natural modes $\{h_n, z_n \; ; \; n = 1, \cdots, N\}$. The derivation follows the one in [64] (see also [65]). Referring to Eq. (4.10), the vector of the received signals $u(l)$ can be expressed more compactly as

$$\mathbf{u} = \mathbf{Z}\mathbf{h} + \boldsymbol{\varepsilon} \tag{4.13}$$

where **u**, **Z**, and **h** are defined in Eq. (4.6), and ε is the noise vector. The evaluation problem is to estimate the natural modes $\{z_n = e^{-(\sigma_n + \nu_l)\Delta\omega} \; ; n = 1, \cdots, N\}$ of the sources from the L samples of the array $u(0), \cdots, u(L-1)$.

To carry out the evaluation problem, we make the following assumptions [66]:

A1: The noise ε is a stationary and ergodic complex valued Gaussian process with zero mean and variance matrix $\delta^2\mathbf{I}$, where δ^2 is an unknown scalar and **I** is the identity matrix.

A2 : The noise samples $\{\varepsilon(l)\}$ are statistically independent.

Unlike the common approach in the sensor array literature [67], we do not regard the signals as sample functions of random process. Instead, we regard them as unknown deterministic sequences. Although this is done mainly because it allows, certain computational simplifications, it also has some interesting advantages when the reflection waveforms are to be analyzed [68].

Under these assumptions, it follows from Eq. (4.13) that the joint density function of the sampled data can be written as

$$f(\mathbf{u}) = \frac{1}{\pi \cdot \det[\delta^2 I]} \exp\left[-\frac{1}{\delta^2} |\mathbf{u} - \mathbf{Z}(z_n)\mathbf{h}|^2\right] \tag{4.14}$$

where "det ( )" denotes the determinant. Thus, the log likelihood, ignoring constant terms, is given by

$$LH = -L\log(\delta^2) - \frac{1}{\delta^2}|\mathbf{u} - \mathbf{Z}(z_n)\mathbf{h}|^2 \ . \tag{4.15}$$

To compute the ML estimator, we have to maximize the log likelihood with respect to the unknown parameters $\{z_n, \mathbf{h}\}$ and noise variance δ^2. Fixing $\{z_n, \mathbf{h}\}$, and then maximizing it with respect to δ^2, we get

$$\delta^2 = \frac{1}{L}|\mathbf{u} - \mathbf{Z}(z_n)\mathbf{h}|^2 \ . \tag{4.16}$$

Substituting this result back into the log-likelihood function, ignoring constant terms, one deduces that the ML estimator is obtained by solving the following maximization problem:

$$\max_{\{z_n\},\, \mathbf{h}} \left\{-L\log\left[\frac{1}{L}|\mathbf{u} - \mathbf{Z}(z_n)\mathbf{h}|^2\right]\right\} . \tag{4.17}$$

Since the logarithm is a monotonic function, the above maximization problem is equivalent to the following minimization problem:

$$\min_{\{z_n\},\, \mathbf{h}} \left\{|\mathbf{u} - \mathbf{Z}(z_n)\mathbf{h}|^2\right\} . \tag{4.18}$$

To carry out this minimization, we fix $\mathbf{h}$ and minimize Eq. (4.18) with respect to $\{z_n \mid n = 1, 2, \cdots, N\}$. This yields the following solution

$$\mathbf{h} = \left[\mathbf{Z}^H(z_n)\mathbf{Z}(z_n)\right]^{-1}\mathbf{Z}^H(z_n)\mathbf{u} \ . \tag{4.19}$$

Substituting Eq. (4.19) into Eq. (4.18), we arrived at the following minimization problem:

$$\min_{\{z_n\}} \left\{ |\mathbf{u} - \mathbf{Z}(z_n)\left[\mathbf{Z}^H(z_n)\mathbf{Z}(z_n)\right]^{-1}\mathbf{Z}^H(z_n)\mathbf{u}|^2 \right\} \ . \tag{4.20}$$

This can be rewritten as

$$\min_{\{z_n\}} \left\{ |\mathbf{u} - \mathbf{P}_{\mathbf{Z}}(z_n)\mathbf{u}|^2 \right\} \tag{4.21a}$$

where $\mathbf{P}_{\mathbf{Z}}(z_n)$ is the projection operator onto the space spanned by the columns of the matrix $\mathbf{Z}(z_n)$,

$$\mathbf{P}_{\mathbf{Z}}(z_n) = \mathbf{Z}(z_n)\left[\mathbf{Z}^H(z_n)\mathbf{Z}(z_n)\right]^{-1}\mathbf{Z}^H(z_n) \ . \tag{4.21b}$$

Thus the ML estimator of the parameter z_n is obtained by maximizing the log-likelihood function

$$LH(\{z_n\}) = |\mathbf{P}_{\mathbf{Z}}(z_n)\mathbf{u}|^2 \ . \tag{4.22}$$

This estimator has an appealing geometric interpretation. Notice, from Eq. (4.13), that in the absence of noise the vector $\mathbf{u}$ stays in the N-dimensional space spanned by the columns of $\mathbf{Z}(z_n)$, referred to as the signal space, while the presence of noise may cause $\mathbf{u}$ to wander away from this subspace. From Eq. (4.22), it follows that the ML estimator is obtained by searching over the array manifold for those N steering vectors that form the N-dimensional signal subspace which is closest to the vector $\mathbf{u}$, where closeness is measured by the modulus of the projection of the vectors onto this subspace. A different form of Eq. (4.22), which is found to be more suitable for our purposes, is obtained by rewriting it as

$$LH(\{z_n\}) = \mathrm{tr}\left[\mathbf{P}_Z(z_n)\mathbf{R}\right] \tag{4.23a}$$

where "tr[ ]" is the trace of the bracketed matrix, and **R** is the sample covariance matrix [69]

$$\mathbf{R} = \mathbf{u}\mathbf{u}^H \ . \tag{4.23b}$$

However, The maximization of the log-likelihood Eq. (4.23) is a nonlinear, multi-dimensional maximization problem, and as such is computationally expensive.

4.4 MUSIC Method

It is seen from Eq. (4.13) that the measured data with the ultrasound transducer are given in the same form as those received by an L-element array antenna [70]. Thus, we may estimate the natural mode factors $\{z_n\ , n = 1, \cdots, N\}$ using the MUSIC algorithm.

The MUSIC algorithm uses the eigenstructure of the measured data correlation matrix [71]. From Eq. (4.13), the data correlation matrix can now be expressed as

$$\begin{aligned} \mathbf{R} &= E[\mathbf{u}\mathbf{u}^H] \\ &= \mathbf{Z}\, E[\mathbf{h}\mathbf{h}^H]\mathbf{Z}^H + \delta^2\mathbf{I} \end{aligned} \tag{4.24}$$

where "E[ ]" denotes the ensemble average, and $E[\mathbf{h}\mathbf{h}^H]$ denotes the signal correlation matrix. Here we assume that $E[\varepsilon\varepsilon^H] = \delta^2\mathbf{I}$ holds in Eq. (4.24). Since these components cannot be measured in advanced with the present ultrasonic system, we cannot show the validity of the assumption.

Now we can express the eigenvalues and the corresponding eigenvectors of **R** as $\eta_1 \geq \cdots \geq \eta_L$ and $v_1 \geq \cdots \geq v_L$, respectively. Then, the following properties hold when the individual signals are incoherent.

(1) The minimum eigenvalue of **R** is equivalent to δ^2 with multiplicity $L - N$. Then we have

$$\eta_1 \geq \eta_2 \geq \cdots \geq \eta_N > \eta_{N+1} = \eta_{N+2} = \cdots = \eta_L = \delta^2 \ . \qquad (4.25)$$

From the expression $\eta_N > \eta_{N+1} = \eta_{N+2} = \cdots = \eta_L = \delta^2$, we may obtain the number of reflections (N).

(2) The eigenvectors corresponding to the minimum eigenvalue are orthogonal to the columns of the matrix **Z**. That is, they are orthogonal to the "mode vector" of the signals:

$$\left\{ \mathbf{v}_{N+1}, \cdots, \mathbf{v}_L \right\} \perp \left\{ \mathbf{c}(z_1), \cdots, \mathbf{c}(z_N) \right\} \qquad (4.26)$$

where $\mathbf{c}(z_n) = [1 \ z_n \ z_n^2 \ \cdots \ z_n^{L-1}]^T$ is the n^{th} column of the matrix **Z**.

We define a $\mathbf{V}_L$ to be the $L \times (L-N)$ matrix whose columns are the $L - N$ noise eigenvectors. Then, we can estimate the natural mode of each reflection by searching the peak position of the following function.

$$P_{\text{music}}(z) = \frac{\mathbf{c}(z)^H \mathbf{c}(z)}{\mathbf{c}(z)^H \mathbf{V}_L \mathbf{V}_L^H \mathbf{c}(z)} \ . \qquad (4.27)$$

Properties (1) and (2), hold when the matrix $\mathbf{h}\mathbf{h}^H$ is nonsingular. However, the parameters $(h_1, \cdots, h_N)$ are coherent in the case of measurements with a layered structure mechanism. This is because the parameters that are identical to the reflection coefficients do not change, but have constant values. Thus, the matrix $E(\mathbf{h}\mathbf{h}^H)$ is singular, and the MUSIC method does not work properly [72-73]. The construction of $E(\mathbf{h}\mathbf{h}^h)$ has to employ some de-correlation preprocessing to destroy the parameter coherence which makes the problem more difficult.

4.5 Matrix Pencil Method

Following the idea of the matrix pencil method, we consider the following set of "information" vectors: $\mathbf{u}_0, \mathbf{u}_1, \cdots, \mathbf{u}_M$, where

$$\mathbf{u}_i = [u(i), u(i+1), \cdots, u(i+L-M-1)]^T \ . \tag{4.28}$$

The superscript " ^{T} " denotes the transpose of a matrix. Based on these vectors, we define the matrices $\mathbf{U}_1$ and $\mathbf{U}_2$ as

$$\mathbf{U}_1 = \left[\mathbf{u}_0, \mathbf{u}_1, \cdots, \mathbf{u}_{M-1}\right] \tag{4.29}$$

$$\text{and} \quad \mathbf{U}_2 = \left[\mathbf{u}_1, \mathbf{u}_2, \cdots, \mathbf{u}_M\right] \ . \tag{4.30}$$

To look into the underlying structure of the two matrices, one can write

$$\mathbf{U}_1 = \mathbf{Z}_L \mathbf{H} \mathbf{Z}_R \text{and} \tag{4.31}$$

$$\mathbf{U}_2 = \mathbf{Z}_L \mathbf{H} \mathbf{Z}_o \mathbf{Z}_R \tag{4.32}$$

where

$$\mathbf{Z}_L = \begin{bmatrix} 1 & \cdots & 1 \\ z_1 & \cdots & z_N \\ \vdots & & \vdots \\ z_1^{L-M-1} & \cdots & z_N^{L-M-1} \end{bmatrix} , \tag{4.33}$$

$$\mathbf{Z}_R = \begin{bmatrix} 1 & z_1 & \cdots & z_1^{M-1} \\ 1 & z_2 & \cdots & z_2^{M-1} \\ \vdots & \vdots & & \vdots \\ 1 & z_N & \cdots & z_N^{M-1} \end{bmatrix} , \tag{4.34}$$

$$\mathbf{Z}_o = \text{diag}\left[z_1, \cdots, z_N\right] , \tag{4.35}$$

$$\text{and} \quad \mathbf{H} = \text{diag}\left[h_1, \cdots, h_N\right] \ . \tag{4.36}$$

Based on the above decomposition of $\mathbf{U}_1$ and $\mathbf{U}_2$, one can show that if $N \le M \le L - N$, then the poles $\{z_n \mid n = 1, \cdots, N\}$ are the generalized eigenvalues of the matrix pencil $\mathbf{U}_2 - z\mathbf{U}_1$. Namely, if $N \le M \le L - N$, then $z = z_n$ is a rank-reducing eigenvalue of $\mathbf{U}_2 - z\mathbf{U}_1$.

To develop and illustrate the use of an algorithm for computing the generalized eigenvalues of the matrix pencil problem we can write

$$\begin{aligned} \mathbf{U}_1^{\ddagger}\mathbf{U}_2 &= \mathbf{Z}_R^{\ddagger}\mathbf{H}^{-1}\mathbf{Z}_L^{\ddagger}\mathbf{Z}_L\mathbf{H}\mathbf{Z}_o\mathbf{Z}_R \\ &= \mathbf{Z}_R^{\ddagger}\mathbf{Z}_o\mathbf{Z}_R \end{aligned} \tag{4.37}$$

where the superscript ‡ denotes the (Moore-Penrose) pseudo-inverse [74], whereas we use "-1" for the regular inverse. It can be seen from Eq. (4.37) that there exist vectors $\mathbf{w}_n$; $n = 1, \cdots, N$ such that

$$\mathbf{U}_1^{\ddagger}\mathbf{U}_1\mathbf{w}_n = \mathbf{w}_n \tag{4.38}$$

and

$$\mathbf{U}_1^{\ddagger}\mathbf{U}_2\mathbf{w}_n = z_n\mathbf{w}_n \quad . \tag{4.39}$$

The $\mathbf{w}_n$ are the generalized eigenvectors of $\mathbf{U}_2 - z\mathbf{U}_1$. To compute the pseudo-inverse $\mathbf{U}_1^{\ddagger}$, one can use the singular value decomposition (SVD) [75] of $\mathbf{U}_1$ as follows:

$$\begin{aligned} \mathbf{U}_1 &= \sum_{n=1}^{N} \eta_n \mathbf{t}_n \mathbf{v}_n^H \\ &= \mathbf{T}\mathbf{D}\mathbf{V}^H \end{aligned} \tag{4.40}$$

$$\mathbf{U}_1^{\ddagger} = \mathbf{V}\mathbf{D}^{-1}\mathbf{T}^H \tag{4.41}$$

where $\mathbf{T} = [\mathbf{t}_1, \cdots, \mathbf{t}_N]$, $\mathbf{V} = [\mathbf{v}_1, \cdots, \mathbf{v}_N]$, and $\mathbf{D} = \mathrm{diag}[\eta_1, \cdots, \eta_N]$. The superscript ^{H} denotes the conjugate transpose of a matrix. $\mathbf{T}$ and $\mathbf{V}$ are matrices of left and right singular vectors, respectively. Note that for noisy data $u(l)$ one should choose $\eta_1, \cdots, \eta_N$ to be the N largest singular values of $\mathbf{U}_1$, and the resulting $\mathbf{U}_1^{\ddagger}$ is called the truncated pseudo-inverse of $\mathbf{U}_1$. Since $\mathbf{U}_1^{\ddagger}\mathbf{U}_1 = \mathbf{V}\mathbf{V}^H$ and $\mathbf{V}^H\mathbf{V} = \mathbf{I}$, substituting Eq. (4.41) into Eq. (4.39) and left multiplying Eq. (4.39) by $\mathbf{V}^H$ yields

$$\left[\mathbf{Z} - z_n \mathbf{I}\right]\mathbf{z}_n = 0 \tag{4.42}$$

where $n = 1, \cdots, N$,

$$\mathbf{Z} = \mathbf{D}^{-1}\mathbf{T}^H\mathbf{U}_2\mathbf{V} \ , \tag{4.43}$$

and

$$\mathbf{z}_n = \mathbf{V}^H\mathbf{w}_n \ . \tag{4.44}$$

Notice that $\mathbf{Z}$ is an $N{\times}N$ matrix and that z_n and $\mathbf{z}_n$ are, respectively, eigenvalues and eigenvectors of $\mathbf{Z}$.

It is important to realize that the number of poles, N, can be estimated from the singular values,

$$\eta_1 \geq \eta_2 \geq \cdots \geq \eta_N \geq \cdots \geq \eta_{min(L-M,\,M)} \ ,$$

since $\eta_{N+1} = \cdots = \eta_{min(L-M,\,M)} = 0$ for noiseless data.

If $M = N$, the SVD of $\mathbf{U}_1$ is not required, and z_n ; $n = 1, \cdots, N$ are the eigenvalues of the $N{\times}N$ matrix $\left[\mathbf{U}_1^H\mathbf{U}_1\right]^{-1}\mathbf{U}_1^H\mathbf{U}_2$ which is obtained by substituting $\mathbf{U}_1^{\ddagger} = \left[\mathbf{U}_1^H\mathbf{U}_1\right]^{-1}\mathbf{U}_1^H$ into Eq. (4.39). Furthermore, one can verify that with or without noise,

$$\left[\mathbf{U}_1^H\mathbf{U}_1\right]^{-1}\mathbf{U}_1^H\mathbf{U}_2 = \begin{bmatrix} 0 & \cdots & -a_N \\ 1 & & -a_{N-1} \\ \vdots & \ddots & \vdots \\ \cdot & \cdot & \cdot \\ & & -a_1 \end{bmatrix} \tag{4.45}$$

which is the companion matrix of the polynomial

$$1 + \sum_{n=1}^{N} a_n z^{-1} = 0 \ . \tag{4.46}$$

Where

$$\begin{bmatrix} a_N \\ a_{N-1} \\ \cdot \\ \cdot \\ \cdot \\ a_1 \end{bmatrix} = - \left[\mathbf{U}_1^H \mathbf{U}_1 \right]^{-1} \mathbf{U}_1^H \mathbf{u}_p \tag{4.47}$$

is the solution of the least square Prony method. So for $M = N$, the matrix pencil method is equivalent to the LS Prony method. However, in the matrix pencil method, it gives us different values of M for $N \le M \le L - N$.

4.6 SPA Method

A very interesting method for natural mode extraction which can be constructed using the frequency-sampling concept introduced in Chapter 3. This section will develop the SPA method such that the frequency response of the backscattered field will pass through a given response. It is a fact that the backscattered field is not a linear phase function, the sampled response must then contain both magnitude and phase.

This method uses a criterion based on the SVD algorithm, which is helpful in increasing the accuracy of the mode extraction [76, 77], rather than rely upon the more commonly used LS error approximation between the actual and desired frequency response. Furthermore, it is a useful noncyclic design to avoid the coherence of the measured signals.

First we define the z-transform of the "causal" part of the spectral sequence $u(l)$ as

$$U(z) = \sum_{l=0}^{\infty} u(l) z^{-l} \quad , \quad z \in \mathbb{C} \ . \tag{4.48}$$

With Eq. (4.1), this series converges for $|z| > 1$ to a rational function in the z-plane:

$$U(z) = \sum_{l=0}^{\infty}\left[\sum_{n=1}^{N} h_n z_n^l\right] z^{-l} \tag{4.49}$$

$$= \sum_{n=1}^{N} h_n \left[\sum_{l=0}^{\infty} z_n^l z^{-l}\right]$$

$$= \sum_{n=1}^{N} h_n \frac{z}{z - z_n}$$

$$= \frac{\sum_{n=0}^{N} b_n z^{N-n}}{\sum_{n=0}^{N} a_n z^{N-n}} = \frac{B(z)}{A(z)} \ ,$$

with $a_0 = 1$ and $b_N = 0$. Equation (4.49) can be rewritten as

$$B(z) = U(z)A(z) \ , \tag{4.50}$$

which is the z-transform version of convolution. The convolution can be written as a matrix multiplication. Using the first L terms of the impulse response, we can write

$$\begin{bmatrix} b_0 \\ b_1 \\ \cdot \\ \cdot \\ \cdot \\ 0 \\ \cdot \\ \cdot \\ \cdot \\ 0 \end{bmatrix} = \begin{bmatrix} u(0) & 0 & \cdots & 0 \\ u(1) & u(0) & & \\ \cdot & & \cdot & \\ \cdot & & \cdot & \\ \cdot & & \cdot & \\ u(N) & & \cdots & u(0) \\ \cdot & & & \cdot \\ \cdot & & & \cdot \\ \cdot & & & \cdot \\ u(L-1) & & \cdots & u(L-N-1) \end{bmatrix} \begin{bmatrix} 1 \\ a_1 \\ \cdot \\ \cdot \\ \cdot \\ a_N \end{bmatrix} . \tag{4.51}$$

To compute the coefficients of a_n and b_n, we partition the matrices into the form of

$$\begin{bmatrix} \mathbf{b} \\ \hline 0 \end{bmatrix} = \begin{bmatrix} \mathbf{U}_1 \\ \hline \mathbf{u}_1 : \mathbf{U}_2 \end{bmatrix} \begin{bmatrix} 1 \\ \hline \mathbf{a}_1 \end{bmatrix} , \tag{4.52}$$

where $\mathbf{b}$ is the vector of the $N+1$ numerator coefficients, with $b_N = 0$, of Eq. (4.49), $\mathbf{a}_1$ is the vector of the N denominator coefficients, $\mathbf{u}_1$ is the vector of the last $L - N$ terms of the impulse response, $\mathbf{U}_1$ is the $(N+1)\times(N+1)$ partition of Eq. (4.51), and $\mathbf{U}_2$ is the $(L-N)\times N$ remaining part. The lower $L - N$ equations are written as

$$0 = \mathbf{u}_1 + \mathbf{U}_2\mathbf{a}_1 \tag{4.53a}$$

or

$$\mathbf{u}_1 = -\,\mathbf{U}_2\mathbf{a}_1 \ , \tag{4.53b}$$

First, the vector $\mathbf{a}_1$, the denominator coefficient in Eq. (4.49), has to be determined. The upper $N + 1$ equations of Eq. (4.52), with $\mathbf{a} = \begin{bmatrix} 1 & \mathbf{a}_1 \end{bmatrix}$, are written as

$$\mathbf{b} = \mathbf{U}_1\mathbf{a} \ . \tag{4.54}$$

Then the numerator coefficients vector $\mathbf{b}$ of the transfer function (4.49) can be evaluated.

Now the natural mode factors and coupling coefficients are

$$\tau_n = \frac{\log(z_n)}{\Delta\omega} \tag{4.55a}$$

and

$$h_n = \lim_{z \to z_n} (z - z_n)\frac{B(z)}{zA(z)} \quad ; \qquad n = 1, \cdots, N \ . \tag{4.55b}$$

It is a fact that $u(l)$ can contain only an unknown but finite number N of exponentials. A finite number $L \geq 2N$ of spectral samples $u(l)$ must be sufficient for the calculation of $U(z)$, thereby requiring the use of Eq. (4.55) to determine τ_n and h_n. According to Eq. (3.70), $\vec{u}\,'(\vec{r},\omega)$ is known in a finite interval, the samples $u(l) = \vec{u}\,'(\vec{r},\omega_l)$; $l = 0, 1, \cdots, L$, with $L\Delta\omega \leq \omega_2 - \omega_1$ are also available.

These properties lead to an effective strategy for determining the natural mode factors of an ultrasound backscattering field out of band-limited measurement data. Starting with L spectral samples $u(l)$, a rational function $\tilde{U}(z)$ of order M can be determined using SPA. In particular, the SVD algorithm, which was introduced in both the MUSIC and the matrix pencil methods, can be used for the accuracy estimation of the natural modes in the presence of additive noise. This yields the parameters of

$$\tilde{U}(z) = \frac{\sum_{m=0}^{M} \tilde{b}_m z^{M-m}}{\sum_{m=0}^{M} \tilde{a}_m z^{M-m}} \quad ; \quad \tilde{a}_0 = 1 \text{ and } \tilde{b}_M = 0 \ . \tag{4.56}$$

During the procedure, the order M must be chosen large enough, i.e., $M \geq N$, to correspond to a first estimate of the expected number of reflections. One must calculate the N largest singular values of $\tilde{\mathbf{U}}_2$ to evaluate poles $\tilde{z}_n$ of $\tilde{U}(z)$, and perform a noncyclic convolution to get the information required for determining the estimates of natural mode factors and coupling coefficients by using Eq. (4.55). Because the preceding methods are an interpolation scheme to design a model that only produces the first L+1 terms of the specified $u(l)$, these processes say nothing about other points in the passband. To control $\tilde{u}(z)$ over the whole range of the passband, we pose an approximation problem where we define an equation-error vector for Eq. (4.52) as follows

$$\begin{bmatrix} \mathbf{b} \\ -- \\ 0 \end{bmatrix} + \begin{bmatrix} \mathbf{e} \end{bmatrix} = \begin{bmatrix} \mathbf{U}_1 \\ ----- \\ \mathbf{u}_1 : \mathbf{U}_2 \end{bmatrix} \begin{bmatrix} 1 \\ -- \\ \mathbf{a}_1 \end{bmatrix} . \tag{4.57}$$

If $\mathbf{U}_2$ has full rank, Eq.(4.57) can be solved for $\mathbf{a}_1$. This solution minimizes the lower part of $\mathbf{e}$, and $\mathbf{b} = \mathbf{U}_1\mathbf{a}$ gives zero error for the upper part. Then the natural mode factors and coupling coefficients are determined without any bound on resolution.

Therefore, it is not worthwhile to attempt to design a maximization scheme as in Sections 4.3 and 4.4, since it is difficult to calculate the peaks of the norm of Eqs. (4.22) and (4.27) with respect to the natural modes. Rather, it is necessary to calculate these using an SVD algorithm, for which many computer routines are available.

As with the maximization employed in Sections 4.3 and 4.4, initial guesses are required as a starting point for the iteration process. The main benefit of the SPA method over the ML method and MUSIC method is that no guesses for the complex mode factors are required since they are not used in the construction of the SPA method.

The major problem in employing this scheme is, in reality, the quality of the measurement as the spectral samples $\tilde{u}(l)$ are perturbed by additive noise which causes variations in the estimation process. The resulting resolution is highly influenced by the choice of the modeling technique for the calculation of the parameters of $\tilde{U}(z)$, by the S/N-ratio in the measured data, and by the number L of spectral samples. For high S/N-ratios, however, some improvements can be achieved through additional echo estimation via parameter modeling.

4.7 Comparison of Methods

Five methods for extracting the natural mode factors of the layered structure from a measured response have been presented in this chapter. The sensitivity to random noise and the computational load to numerical implementation have been noted as the motivations behind introducing the SPA method. In this section, a comparison will be made among the various methods, and justification for using the proposed technique will be presented

It has been shown that the new extraction routine SPA is successful in the simple case of a single-mode response, while other methods are also known to work well under certain circumstances. Without too much extra effort, we have shown that the spectral Prony method can be extended to cover multi-mode responses. There are conditions that the natural-mode extraction schemes must be satisfied. First, it must be able to perform in the presence of random noise, which will undoubtedly be introduced at points in the measuring process. Second, it must be able to discriminate nearly degenerate modes which are quite closely spaced compared with the separation between other modes. Third, it should work well when the number of modes in a measured response is underestimated.

The last requirement leads to a particularly useful procedure. Since the number of modes in a measured response will not be known *a priori*, one would like to start from a small number of modes. For methods which need initial guesses, this small number of initial guesses will be very advantageous. This is only possible, of course, if the routine works well when the number of modes in measured response is underestimated.

To test the various requirements, consider a practical example with a three-mode response given by

$$\hat{u}(f) = .6045 + e^{(-.057-j7.257)f} - .6759\, e^{(-.121-j10.304)f} \ ; \ 0 \le f \le 5\ MHz \quad (4.58)$$

Here, the complex mode factors used to construct $\hat{u}(f)$ are the first three natural mode factors from a 4-layer (water-Plexiglas-Aluminum-water) structure. The amplitudes have been chosen to accentuate the reflection coefficients. This response is then sampled at 38 equally spaced points between 1.5 MHz and 3.0 MHz.

The sensitivity of each of the methods to the presence of random noise can be tested by perturbing each point in the response by a random number, the value of which is defined by

$$SNR = \sum_{l=1}^{L} \frac{|u(l)|^2}{L\delta^2} \tag{4.59}$$

and

$$SNR(db) = 10 \log_{10}(SNR) \tag{4.60}$$

where L is the total number of signal samples and δ^2 is the noise variance. Tables 4.1 - 4.3 show the results of using each method with various levels of noise. In the ML and MUSIC methods, only two phase factors have been evaluated. Using a more complex technique would have produced other factors, but would have required more computation time. A total of 200 Monte-Carlo runs were conducted in each of the proposed methods. For the case of Prony's method, the DC component in Eq. (4.58) has been removed, since Prony's method is unable to accommodate a DC component.

Tables 4.1 - 4.3 reveal that, with the exception of the LS Prony method, the techniques work reasonably well in the presence of random noise, both the matrix pencil method and SPA method are among the best. It is reassuring to see that these two quite different approaches yield similar results.

Table 4.1 : Evaluation of different mode extraction methods in the presence of 30 db white noise.

Mode / Method	$\sigma_1 + j\nu_1$	$\sigma_2 + j\nu_2$	$\sigma_3 + j\nu_3$
	0	-.057 - j7.257	-.121 - j10.304
PRONY	σ_1 —	$\sigma_2 = -.079 \pm .016$	$\sigma_3 = -.271 \pm .062$
	ν_1 —	$\nu_2 = 7.275 \pm .015$	$\nu_3 = 10.441 \pm .079$
MLM	σ_1 —	σ_2 —	σ_3 —
	$\nu_1 = -.031 \pm .22$	$\nu_2 = 7.226 \pm .22$	$\nu_3 = 10.344 \pm .22$
MUSIC	σ_1 —	σ_2 —	σ_3 —
	$\nu_1 = -.031 \pm .22$	$\nu_2 = 7.226 \pm .22$	$\nu_3 = 10.344 \pm .22$
PENCIL	$\sigma_1 = 0$	$\sigma_2 = -.059 \pm .005$	$\sigma_3 = -.121 \pm .015$
	$\nu_1 = 0$	$\nu_2 = 7.258 \pm .006$	$\nu_3 = 10.304 \pm .016$
SPA	$\sigma_1 = 0$	$\sigma_2 = -.057 \pm .006$	$\sigma_3 = -.121 \pm .014$
	$\nu_1 = 0$	$\nu_2 = 7.257 \pm .005$	$\nu_3 = 10.305 \pm .012$

Table 4.2 : Evaluation of different mode extraction methods in the presence of 20 db white noise.

Mode / Method	$\sigma_1 + j\nu_1$	$\sigma_2 + j\nu_2$	$\sigma_3 + j\nu_3$
	0	-.057 - j7.257	-.121 - j10.304
PRONY	σ_1 —	$\sigma_2 = -.197 \pm .054$	$\sigma_3 = -1.355 \pm .435$
	ν_1 —	$\nu_2 = 7.384 \pm .053$	$\nu_3 = 11.249 \pm .415$
MLM	σ_1 —	σ_2 —	σ_3 —
	$\nu_1 = -.031 \pm .22$	$\nu_2 = 7.226 \pm .22$	$\nu_3 = 10.344 \pm .22$
MUSIC	σ_1 —	σ_2 —	σ_3 —
	$\nu_1 = -.031 \pm .22$	$\nu_2 = 7.226 \pm .22$	$\nu_3 = 10.344 \pm .22$
PENCIL	$\sigma_1 = -.004 \pm .011$	$\sigma_2 = -.069 \pm .022$	$\sigma_3 = -.188 \pm .054$
	$\nu_1 = 0$	$\nu_2 = 7.388 \pm .053$	$\nu_3 = 10.340 \pm .060$
SPA	$\sigma_1 = -.001 \pm .014$	$\sigma_2 = -.056 \pm .017$	$\sigma_3 = -.133 \pm .043$
	$\nu_1 = 0$	$\nu_2 = 7.260 \pm .017$	$\nu_3 = 10.295 \pm .045$

Table 4.3 : Evaluation of different mode extraction methods in the presence of 10 db white noise.

Mode / Method	$\sigma_1 + j\nu_1$	$\sigma_2 + j\nu_2$	$\sigma_3 + j\nu_3$
	0	-.057 - j7.257	-.121 - j10.304
PRONY	σ_1 —	$\sigma_2 = -.449 \pm .182$	$\sigma_3 = -4.560 \pm 1.732$
	ν_1 —	$\nu_2 = 7.549 \pm .131$	$\nu_3 = 15.326 \pm 2.933$
MLM	σ_1 —	σ_2 —	σ_3 —
	$\nu_1 = -.053 \pm .22$	$\nu_2 = 7.248 \pm .22$	$\nu_3 = 10.322 \pm .22$
MUSIC	σ_1 —	σ_2 —	σ_3 —
	$\nu_1 = -.053 \pm .22$	$\nu_2 = 7.204 \pm .22$	$\nu_3 = 10.366 \pm .22$
PENCIL	$\sigma_1 = -.205 \pm .511$	$\sigma_2 = -.189 \pm .156$	$\sigma_3 = -.535 \pm .307$
	$\nu_1 = .124 \pm .324$	$\nu_2 = 7.426 \pm .761$	$\nu_3 = 10.546 \pm .799$
SPA	$\sigma_1 = -.006 \pm .030$	$\sigma_2 = -.089 \pm .106$	$\sigma_3 = -.223 \pm .151$
	$\nu_1 = 0$	$\nu_2 = 7.414 \pm .811$	$\nu_3 = 10.346 \pm .797$

Note :	$\sigma_n + j\nu_n$	Theoretical modes used to construct impulse response
	PRONY	Least square Prony's Method
	MLM	Maximum Likelihood Method
	MUSIC	MUtiple SIgnal Classification
	PENCIL	PENCIL-matrix Method
	SPA	Spectral Prony's Algorithm

Figure 4.1 shows a simulation of the quasi-impulse response of this 4-layered structure, with 20 *db* random noise added. The first three natural modes were used. This represents a typical measured response. We intend to extract the three modes from the noisy response using the SPA method and Prony's method.

Figure 4.2 shows the results of a straightforward Prony method. The simulated results are deviated from the theoretical ones. Improvements can be made by assuming larger number of modes in the response. These results are also shown in Figure 4.2. The accuracy has improved for overestimated cases, but it is very difficult to determine which of the modes are actually present in the response. Without the *a priori* knowledge of the three mode values it would be difficult to identify the results. On the other hand, Figure 4.3 shows the modes extracted using the SPA method assuming only three modes are present. The results are quite reasonable. The results show that one does not gain much advantage by assuming more than three initial modes.

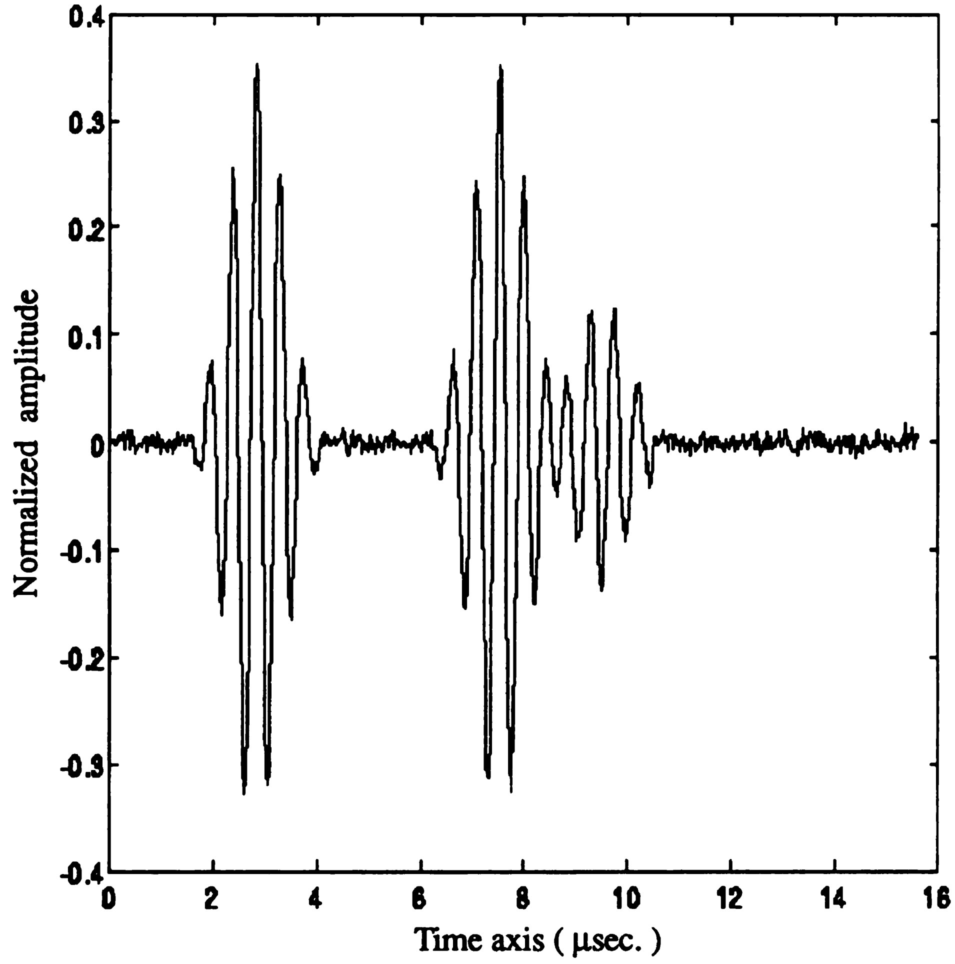

Figure 4.1 : The quasi-impulse response of a 4-layered structure, constructed using the first three natural modes with 20 db noise added.

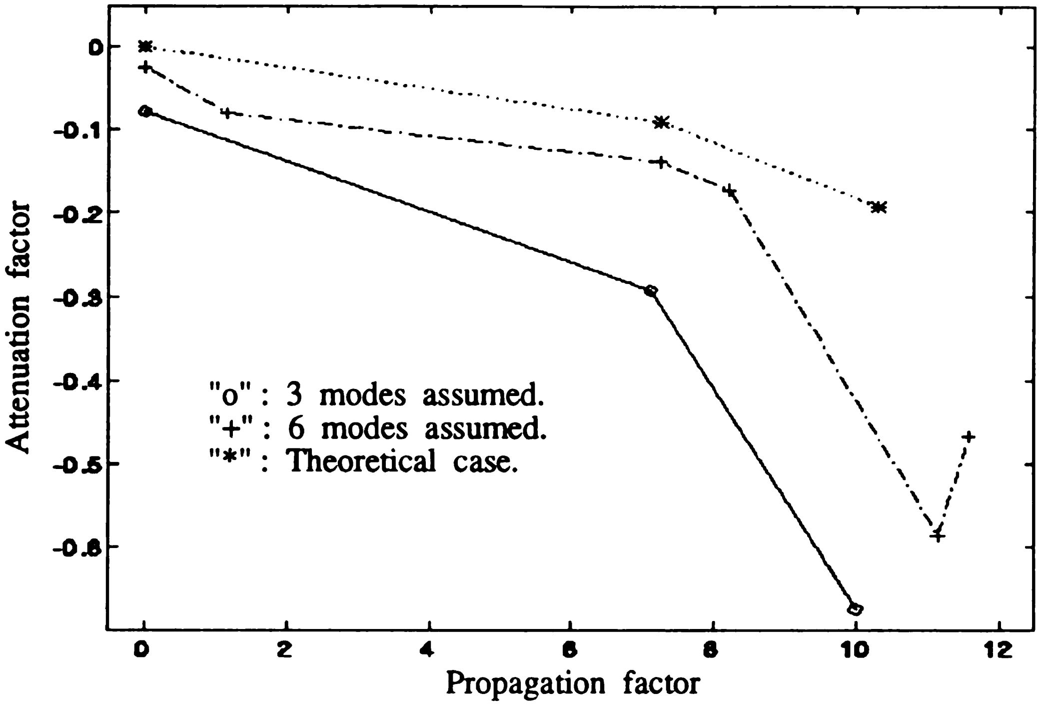

Figure 4.2 : Mode factors evaluated from noisy responses using LS Prony's method with three modes asumed (o) and six modes assumed (+). (A stars denotes the theroretical values.)

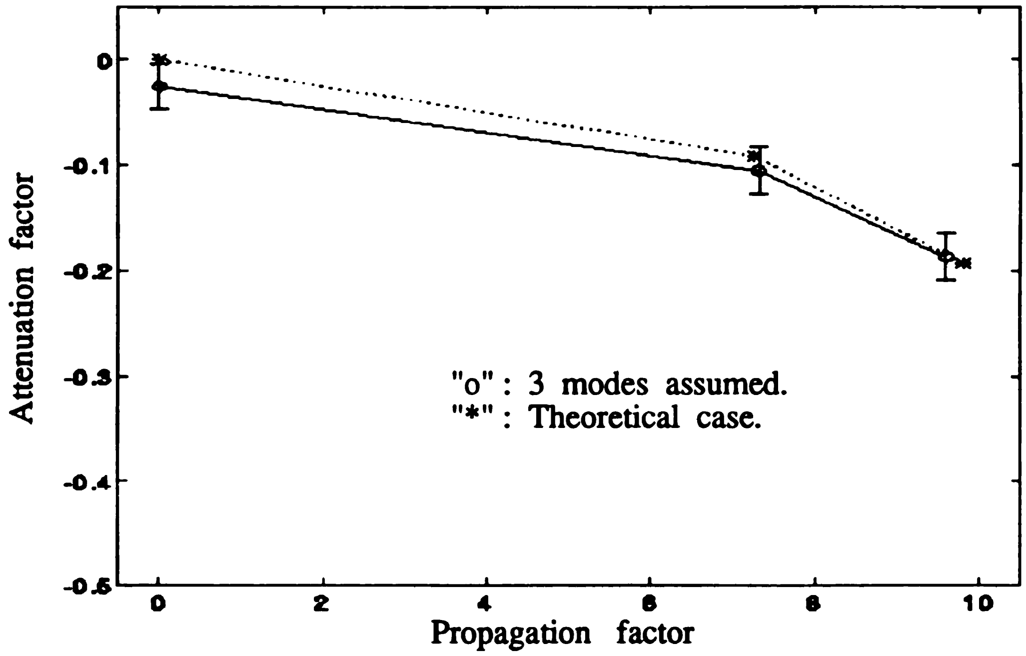

Figure 4.3 : Mode factors evaluated from noisy responses using the SPA method with three modes (o). (A star denotes the theoretical values.)

CHAPTER 5

RECONSTRUCTION PROCEDURES USING THE SPA APPROACH

5.1 Introduction

Ultrasonic identification techniques based on natural resonance involve illuminating an unknown layered structure with an arbitrary spectral waveform and analyzing the scattered ultrasonic field. No special restriction is given on the shape of the incident field other than demanding it to carry adequate energy contents to excite natural modes of the target for identification purpose. On the other hand, the angular-spectrum and backward scattering techniques investigate the probability of constructing a specified wavenumber-limited model which would result a wavenumber-limited scattered field. This chapter will introduce a method to enhance ultrasonic identification of layered structures by combining the SPA concept with the aspect independence of natural modes.

An SPA reconstruction can be described as a phase-detection filter (PDF) which upon excitation of a particular layered structure extinguishes a pre-specified portion of the natural mode phase spectrum. Since the scattered-field response of a layered structure is merely the convolution of the incident field waveform and the structure scattered-field impulse response, it is easy to show that SPA reconstruction need not actually be implemented to affect identification. Indeed, two views of SPA reconstruction will be considered. The first describes the effects of directly passing a specified PDF; it uses a z-transform approach. The second describes the more tractable scheme of convolving this PDF with the measured scattered field waveform; this strategy uses a discrete frequency domain approach. Moreover, the effects of signal processing and implementation considerations will be addressed in Sections 5.3 and 5.4.

Preliminary treatment of the SPA reconstruction technique has been carried out in [78].

5.2 SPA Reconstruction

The motivation for adopting a specified PDF is revealed in the examination of the spectral representation, Eq. (3.79), of the scattered field. Notice that each of the complex terms in the natural mode series of the scattered field is multiplied by $u_i(z_n)$, where $u_i(z_n)$ is the z-transform of the discrete incident field waveform $u_i(l)$, and z_n is the pole of n^{th} natural resonance mode of the layered structure. If a specified PDF is defined as

$$A(z_n) = 0\ , \quad \text{for all} \quad 1 \leq n \leq N\ , \tag{5.1}$$

it will result in a null scattered-field waveform in the high-frequency samples. Consequently, it is easy to reconstruct ultrasonic identification using the SPA technique. Since the PDF is based entirely on the natural modes of a particular object, and since the natural modes of a layered structure are unique, each PDF will then correspond uniquely to one object. Thus, ultrasonic reconstruction using the SPA approach will be easier than analyzing the spectral response of any given scattered field.

As in the natural-resonance-based techniques described in Chapter 3, any convenient incident field with adequate spectral content could be used to illuminate the unknown layered structure. Rather than analyzing the scattered field in terms of its natural mode composition, it would be easier to convolve the scattered field with a PDF defined by Eq. (5.1). Applying the z-transform of the discrete frequency samples of the scattered field to Eq. (3.79) yields

$$u^s(\vec{r},z) = \sum_{n=1}^{N} U'_n(\vec{r}) \frac{z \cdot e^{j\theta_n(\vec{r})}}{z - z_n} \quad . \tag{5.2}$$

Convolution in the discrete frequency-domain is equivalent to multiplication in the z-transform domain, thus we have

$$Z\left\{a(l) * u^s(\vec{r}_o,l)\right\} = A(z)\left[\sum_{n=1}^{N} U'_n(\vec{r}_o) e^{j\theta_n(\vec{r}_o)} \frac{z}{z - z_n}\right] \quad . \tag{5.3}$$

Implementing the inversion integral Eq. (3.62) and invoking Cauchy's residue theorem results in the response

$$\begin{aligned} b(l) &= a(l) * u^s(\vec{r}_o,l) \\ &= \sum_{n=1}^{N} U_n'(\vec{r}_o) e^{j\theta_n(\vec{r}_o)} z_n^l A(z_n) \quad . \end{aligned} \tag{5.4}$$

Ideally, $A(z_n) = 0$ by the definition of Eq. (5.1), so $b(l) = 0$ in the high-frequency samples. In other words, the PDF has extinguished the measured scattered field in the high-frequency samples. It should be noted that it is impossible to reconstruct a PDF as defined in Eq. (5.1), because the real ultrasound field is not available to be measured exactly. The response generated by convolving the PDF with an unexpected object is only related to Eq. (5.4). The poles of $A(z)$ do not correspond to the natural modes of the measured object, however, the discrete frequency samples of $b(l)$ are still a sum of the natural modes.

The problems are that the amplitudes and phases will not be the same as those which would be measured if the specified PDF were used directly. This may seem trivial, but it indicates that the accuracy of identifying certain modes may be poorer. Another aspect is that the use of SPA reconstruction also gives interpolation bias of the results. That is, the condition that $b(l)$ be zero in Eq. (5.4) did not depend on the aspect dependent modal amplitude and phases. Thus, convolution of a PDF with the measured scattered field from the expected layered structure results in zero response regardless of the reflection coefficients.

5.2.1 Reflected Signal Perspective

It is now necessary to find some convenient way to implement the defining PDF equation. For ultrasonic identification, it is more appropriate to define a PDF via

$$b(l) = 0 \qquad ; \quad l \geq L_e \ , \tag{5.5}$$

where $b(l)$ is given by

$$b(l) = a(l) * u^s(\vec{r}_o, l) \tag{5.6}$$

as in Eq. (5.4). Here L_e is the duration of the PDF's impulse response. It is obvious that L_e must always be taken to be finite, or else there would be no high-frequency samples. This analysis may actually be termed a z-transform analysis since it is the z-transform representation of the PDF which is utilized. The z-transform of the PDF is

$$A(z) = Z\left\{a(l)\right\} = \sum_{l=0}^{L_e-1} a(l) z^{-l} \ . \tag{5.7}$$

Referring to Eq. (5.1), the z-transform representation of this PDF requires

$$A(z_n) = \sum_{l=0}^{L_e-1} a(l) z_n^{-l} = 0 \quad , \ 1 \leq n \leq N \ . \tag{5.8}$$

Denoting $z_n = e^{-(\sigma_n + jv_n)\Delta\omega}$ and substituting into Eq.(5.8), the exponential becomes

$$A(z_n) = \sum_{l=0}^{L_e-1} a(l) e^{-(\sigma_n \Delta\omega) l} \Big[\cos(v_n \Delta\omega l) - j \sin(v_n \Delta\omega l) \Big] = 0 \quad ; \quad 1 \le n \le N. \tag{5.9}$$

This shows that both real and imaginary parts of Eq. (5.9) hold simultaneously only if

$$\sum_{l=0}^{L_e-1} a(l) e^{-(\sigma_n \Delta\omega) l} \cos(v_n \Delta\omega l) = 0 \quad ; \quad 1 \le n \le N \ , \tag{5.10a}$$

and

$$\sum_{l=0}^{L_e-1} a(l) e^{-(\sigma_n \Delta\omega) l} \sin(v_n \Delta\omega l) = 0 \quad ; \quad 1 \le n \le N \ . \tag{5.10b}$$

These equations will be used to calculate $a(l)$ upon an appropriate mathematical representation.

We have considered Eq. (5.8) as the z-transform of PDF. Alternatively, it can also be termed a frequency-domain analysis since all calculations avoid the z-transform of $b(l)$. Invoking the definition of Eq. (5.5) along with Eq. (5.6), the scattered-field representation Eq. (3.79) yields

$$b(l) = a(l) * \left\{ \sum_{n=1}^{N} U'_n(\vec{r}_o) e^{j\theta_n(\vec{r})} z_n^{l} \right\} = 0 \quad ; \quad l \ge L_e \ . \tag{5.11}$$

Writing the convolution in summation form gives

$$b(l) = \sum_{l'=0}^{L_e-1} a(l') \cdot \left[\sum_{n=1}^{N} U'_n(\vec{r}_o) e^{j\theta_n(\vec{r})} z_n^{l-l'} \right] = 0 \quad ; \quad l \ge L_e \tag{5.12}$$

which can be written more simply as

$$b(l) = \sum_{n=1}^{N} b_n \cdot \left[\sum_{l'=0}^{L_e-1} a(l') z_n^{-l'} \right] = 0 \quad ; \quad l \ge L_e \tag{5.13}$$

where $b_n = U'_n(\vec{r}_o)e^{j\theta_n(\vec{r}')}z_n^l$. Now Eq. (5.13) can hold only if

$$\sum_{l'=0}^{L_e-1} a(l')e^{-(\sigma_n\Delta\omega)l'}\cos(v_n\Delta\omega l') = 0 \quad ; \; 1 \le n \le N \;, \tag{5.14a}$$

and

$$\sum_{l'=0}^{L_e-1} a(l')e^{-(\sigma_n\Delta\omega)l'}\sin(v_n\Delta\omega l') = 0 \quad ; \; 1 \le n \le N \;. \tag{5.14b}$$

which are identical to Eq. (5.10) from the z-transform analysis.

5.2.2 PDF Representation

To implement the $2N$ equations in Eqs. (5.10a) and (5.10b), the PDF must be represented mathematically. It is necessary to have at least $2N$ variable parameters in the representation in order to satisfy the equations.

The PDF is considered to be represented as

$$a(l) = \sum_{m=0}^{2N} a_m f_m(l) \quad ; \; 0 \le l \le L_e - 1 \tag{5.15}$$

where $f_m(l)$ is the m^{th} basis function from an appropriately chosen set and a_m is the coefficient of the m^{th} basis function. The basis functions do not have specified forms, and they may overlap or be sub-sectional. Substituting Eq. (5.15) into Eq. (5.10) yields

$$\sum_{m=0}^{2N} a_m \cdot \left[\sum_{l=0}^{L_e-1} f_m(l)e^{-(\sigma_n\Delta\omega)l}\cos(v_n\Delta\omega l) \right] = 0 \quad , \; 1 \le n \le N \;, \tag{5.16a}$$

and

$$\sum_{m=0}^{2N} a_m \cdot \left[\sum_{l=0}^{L_e-1} f_m(l)e^{-(\sigma_n\Delta\omega)l}\sin(v_n\Delta\omega l) \right] = 0 \quad , \; 1 \le n \le N \;. \tag{5.16b}$$

When the amplitude parameters represent all the unknown variables, these equations become simultaneous linear equations and can be written in matrix form as

$$\begin{bmatrix} \mathbf{Q}^{c}_{m,n} \\ \cdots\ \cdots \\ \mathbf{Q}^{s}_{m,n} \end{bmatrix} \begin{bmatrix} a_0 \\ \vdots \\ a_{2N} \end{bmatrix} = \begin{bmatrix} 0 \\ \vdots \\ 0 \end{bmatrix} \tag{5.17}$$

where

$$Q^{c}_{m,n} = \sum_{l=0}^{L_s-1} f_m(l) e^{-(\sigma_n \Delta\omega) l} \cos(\nu_n \Delta\omega l) \ , \tag{5.18a}$$

and

$$Q^{s}_{m,n} = \sum_{l=0}^{L_s-1} f_m(l) e^{-(\sigma_n \Delta\omega) l} \sin(\nu_n \Delta\omega l) \ . \tag{5.18b}$$

The entries of the Q matrix are generally difficult to compute by the use of Eqs. (5.18a) and (5.18b). The amount of effort needed to calculate these entries in closed form can be reduced by using the z-transform domain analysis of Section 5.2.1. Comparing Eq. (5.18) with Eq. (5.8) reveals that the matrix entries can also be written in terms of the z-transform of $f_m(l)$ as

$$Q^{c}_{m,n} = \mathrm{Re}\left\{ F_m(z_n) \right\} \tag{5.19a}$$

and

$$Q^{s}_{m,n} = \mathrm{Im}\left\{ F_m(z_n) \right\} \tag{5.19b}$$

where $F_m(z)$ is the transform of $f_m(l)$. With few exceptions, the transform of $f_m(l)$ will be a much simpler function than those resulting from the computation of Eq. (5.18). The real and imaginary parts of $F_m(z)$ are easily separated after the transform has been numerically evaluated. The only drawback to this approach is the need for tedious arithmetic manipulations.

5.2.3 SPA Approach

Letting $u(l)$ represent the discrete frequency-domain response of a layered structure, the convolution of a specified PDF $a(l)$ and its response can be written as

$$b(l) = a(l) * u(l) = \sum_{l'=0}^{L_e-1} a(l')u(l-l') \quad ; \; 0 \le l \le L \; . \tag{5.20}$$

The natural mode factors embedded in $u(l)$ can be extracted by constructing $a(l)$ as a PDF [via Eq. (5.18)] and minimizing the norm of the high-frequency sample convolved response

$$||b(l)||_2^2 = \sum_{l=L_e}^{L} \left[b(l)\right]^2 \tag{5.21}$$

with respect to the parameters $\sigma_1, \cdots, \sigma_N, \nu_n, \cdots, \nu_N$, where $L - L_e$ discrete points are chosen at which to evaluate the norm. If $u(l)$ is a pure sum of natural modes, and if a sufficient number of natural mode factors are used to construct $a(l)$, then the minimum of Eq. (5.21) will be zero, and the routine will work well.

For the sake of extracting complex factors from the PDF as easily as possible, it is preferable to express the PDF in terms of discrete impulses,

$$a(l) = \sum_{m=0}^{2N} a_m \delta(l-m) \quad \text{with} \quad a_0 = 1 \tag{5.22}$$

where N modes are assumed to be in $u(l)$. In theory it would be permissible to use more than $2N$ basis functions, but this leads to matrix conditioning problems, since only N modes are actually present in $u(l)$. However, the summation equation is forced to be satisfied at discrete samples which are spaced in the same manner as the impulse functions in $u(l)$. This allows Eq. (5.6) to be written as

1) : $l < 2N$

$$\begin{bmatrix} u_0 & & & & \\ u_1 & u_0 & & & \\ u_2 & u_1 & . & & \\ . & . & . & & \\ . & . & & . & \\ . & . & & & \\ u_{2N-1} & u_{2N-2} & \cdot & \cdot \ \cdot & u_0 \end{bmatrix} \begin{bmatrix} 1 \\ a_1 \\ a_2 \\ . \\ . \\ . \\ a_{2N} \end{bmatrix} = \begin{bmatrix} b_0 \\ b_1 \\ b_2 \\ . \\ . \\ . \\ b_{2N-1} \end{bmatrix} \tag{5.23a}$$

$$\mathbf{U}_1 \cdot \begin{bmatrix} 1 \\ \mathbf{a} \end{bmatrix} = \mathbf{b} \tag{5.23b}$$

where $\mathbf{a} = \begin{bmatrix} a_1 \, a_2 & \cdots & a_{2N} \end{bmatrix}^T$ and $\mathbf{b} = \begin{bmatrix} b_0 \, b_1 & .. & b_{2N-1} \end{bmatrix}^T$.

2) : $l \geq 2N$

$$\begin{array}{lcr} a_1 u_{2N-1} + a_2 u_{2N-2} + a_3 u_{2N-3} + \cdots + a_{2N} u_0 & = & -u_{2N} \\ a_1 u_{2N} + a_2 u_{2N-1} + a_3 u_{2N-2} + \cdots + a_{2N} u_1 & = & -u_{2N+1} \\ \cdots & & \\ . & & . \\ . & & . \\ . & & . \\ a_1 u_{L-1} + \qquad \cdots \qquad + a_{2N} u_{L-2N} & = & -u_L \end{array} \tag{5.24}$$

where $L \geq 4N$ is the total samples of $u(l)$ and $u_l = u(l)$. Eq. (5.24) can then be written in matrix form as

$$\begin{bmatrix} u_{2N-1} & u_{2N-2} & \cdots & u_0 \\ u_{2N} & u_{2N-1} & \cdots & u_1 \\ . & . & & . \\ . & . & & . \\ . & . & & . \\ u_{L-1} & u_{L-2} & \cdots & u_{L-2N} \end{bmatrix} \begin{bmatrix} a_1 \\ a_2 \\ . \\ . \\ . \\ a_{2N} \end{bmatrix} = \begin{bmatrix} -u_{2N} \\ -u_{2N+1} \\ . \\ . \\ . \\ u_L \end{bmatrix} \tag{5.25a}$$

$$\mathbf{U}_2 \cdot \mathbf{a} = \mathbf{b}_1 \tag{5.25b}$$

where $\mathbf{b}_1 = \begin{bmatrix} -u_{2N} \ -u_{2N+1} & \cdots & u_L \end{bmatrix}$.

Once the coefficient of a_n is determined by solving Eq. (5.25), the natural mode factors can be found by calculating the roots of

$$\sum_{m=0}^{2N} a_m z^{2N-m} = 0 \ . \tag{5.26}$$

The n^{th} coupling coefficient can also be determined as

$$u'_n(\vec{r})e^{j\theta_n(\vec{r})} = \lim_{z \to z_n} \left[z - z_n \right] \frac{B(z)}{zA(z)} \ . \tag{5.27}$$

5.3 Signal Processing Considerations

The reconstruction algorithm described above involves a number of signal processing steps. The following procedure describes the final reconstruction when small changes are made to the signal processing procedure.

The algorithm for reconstructing acoustic properties of a layered structure from SPA is briefly described below:

1) Collect the reflected waveform.
2) Fourier transform each reflection waveform.
3) Evaluate the N natural modes of the layered structure using the SPA method.
4) Implement SPA by using an N^{th} order PDF to get the estimates of the acoustic properties of the layered structure.

At each step of this procedure, the signal processing theory suggests a number of methods to improve the reconstruction. These include:

a) Applying a Hamming window to the reflection waveform to smooth the data at the end of the receiver.
b) Zero padding the samples to reduce the effects of inter-period interference. This also increases the resolution in the frequency domain and should make mode extraction more accurate.

c) **Multiplying the Fourier transform of the reflection waveform by a band-pass filter (BPF) to reduce the effects of high and low frequency deformations.**

These steps are illustrated in Figure 5.1 where optional steps have been indicated with dashed boxes.

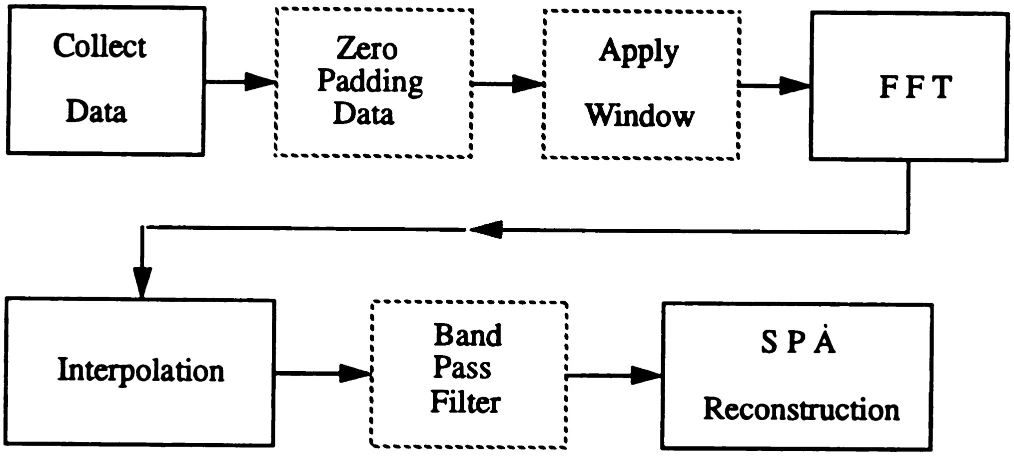

Figure 5.1 : The signal processing steps in a typical S P A reconstruction are shown above. The steps that are needed are shown with a solid box while the optional steps are shown with dashed boxes.

To evaluate the effects of each of these changes, Figures 5.2 and 5.3 show the estimated natural mode factors using all eight possible combinations of options. The data were measured from a 11.675 mm Plexiglass layer under the ultrasonic wave with an operation frequency of 2.25 MHz. An important part of the reconstruction process is filtering the reflection data. The filter is implemented with an FFT algorithm. These algorithms do not perform an aperiodic convolution like that used in linear system theory, but rather a circular convolution. If the data are padded with zeros so that the new data sequence is twice as long as the original, then the results produced by circular and aperiodic convolution are the same. In addition, zero padding the original reflection increases the resolution of the data in the frequency domain and thus makes an interpolation scheme more accurate. Unfortunately, the extra data require more than double the computational time. For example: an FFT takes $N\log_2 N$ operations so that when N is doubled, the computational expense goes up by a factor of

$$\frac{(2N)\log_2(2N)}{N\log_2 N} = 2\left[1 + \frac{2}{\log_2 N}\right] . \tag{5.28}$$

Based on the reconstruction results shown in Figure 5.2, it can be concluded that doubling the size of the reflection data only makes a small improvement in the quality of the reconstruction. Since the extra zeros cause more than doubling the computational expense involved in filtering the data, it is advisable not to zero pad.

A second signal processing concern relates to data truncation. In a real-life experiment, it is only possible to collect and process a finite amount of data. Generally, this does not present a problem since the data eventually vanishes outside a specific range and the data can be truncated without loss of signal information. The data truncation error can then be mathematically modeled as a multiplication in the time domain by a rectangular window [79]. In the frequency domain this is equivalent to convolving the data with a sinc function and thus leveling the frequency domain signal. Other windows like the Hamming window have also been used to reduce the effects of data truncation.

Figure 5.2 shows that a Hamming window does not have the same positive effect as the SPA reconstruction. In this case, most of the high frequency information is at either end of the reflected waveform; thus, the window only serves to attenuate the high frequency components. Figure 5.4 shows that the Fourier transform of the reflection is smoothed before (top graph) and after (bottom graph) a Hamming window is applied. The loss of high frequency data caused by the Hamming window leads to lower attenuation factors in reconstruction, as depicted in Figures 5.2 and 5.3.

Finally, a very big improvement is observed by adding a BPF before SPA reconstruction of the data. Before the filtering, SPA implementation includes partial terms which also serve to enhance the low and high frequency noises. However, by adding a BPF, this effect is counteracted.

Based on the information shown in Figures 5.2 and 5.3, we conclude that the best results are obtained if a BPF is used, but that zero padding the reflection data and applying a Hamming window to the reflection data do not significantly improve the results.

No Hamming window

No zero padding

Attenuation *(db / mm-MHz)*	0.2909
Acoustic Speed *(m/sec)*	2850.03
Reflection Coeff.	0.3713
Acoustic Imped. *(Kg / m^2-sec)*	$3.272 *10^6$

With zero padding

Attenuation *(db / mm-MHz)*	0.3106
Acoustic Speed *(m/sec)*	2848.45
Reflection Coeff.	0.3711
Acoustic Imped. *(Kg / m^2-sec)*	$3.270 *10^6$

Hamming window

No zero padding

Attenuation *(db / mm-MHz)*	0.1555
Acoustic Speed *(m/sec)*	2845.89
Reflection Coeff.	0.3707
Acoustic Imped. *(Kg / m^2-sec)*	$3.267 *10^6$

With zero padding

Attenuation *(db / mm-MHz)*	0.1484
Acoustic Speed *(m/sec)*	2841.15
Reflection Coeff.	0.3700
Acoustic Imped. *(Kg / m^2-sec)*	$3.262 *10^6$

Figure 5.2: The material properties of reconstruction are shown with a 11.675 *mm* thin Plexiglass layer and the Hamming window added.
(All reconstruction shown here are without band-pass filtering)

	No zero padding		With zero padding	
No Hamming window	Attenuation (*db / cm-MHz*)	0.1332	Attenuation (*db / mm-MHz*)	0.1328
	Acoustic Speed (*m/sec*)	2754.41	Acoustic Speed (*m/sec*)	2754.06
	Reflection Coeff.	0.3565	Reflection Coeff.	0.3565
	Acoustic Imped. (Kg / m^2*-sec*)	$3.162 * 10^6$	Acoustic Imped. (Kg / m^2*-sec*)	$3.162 * 10^6$
Hamming window	Attenuation (*db / mm-MHz*)	0.1123	Attenuation (*db / mm-MHz*)	0.1116
	Acoustic Speed (*m/sec*)	2756.01	Acoustic Speed (*m/sec*)	2755.91
	Reflection Coeff.	0.3567	Reflection Coeff.	0.3567
	Acoustic Imped. (Kg / m^2*-sec*)	$3.164 * 10^6$	Acoustic Imped. (Kg / m^2*-sec*)	$3.164 * 10^6$

Figure 5.3: The material properties of reconstruction are shown with a 11.675 *mm* thin Plexiglass layer and the Hamming window added.
(All reconstruction shown here are with band-pass filtering)

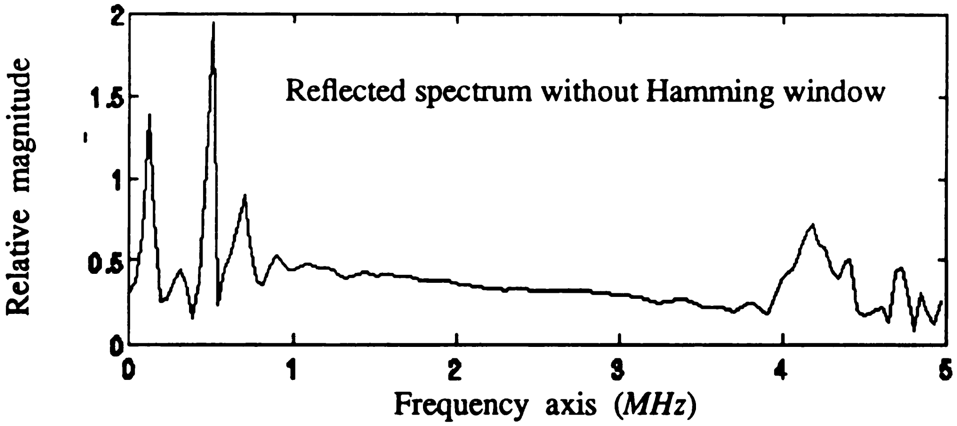

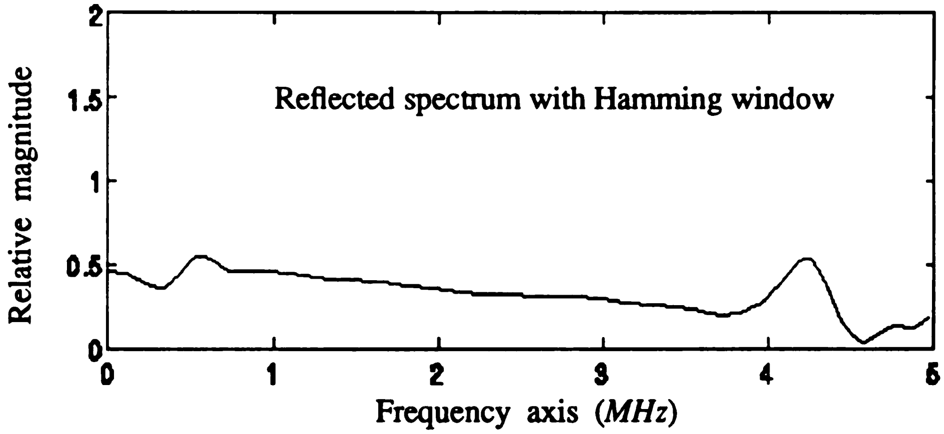

Figure 5.4 : The spectrum of the field before (top graph) and after (bottom graph) multiplying by a Hamming window in the frequency domain are shown here.

5.4 Implementation Considerations

The quality of an SPA reconstruction is limited by both mathematical approximations and experimental limitations. In the derivation of a model for the scattered field either the Born or the Rytov approximation is used to solve UFIE for the scattered field. These approximations are a source of error and limit the applications, as addressed in Chapter 2.

The experimental considerations, on the other hand, are caused by a shortage of data. It is only possible to collect a finite amount of data about the backscattering field, and the experimental errors can be attributed to interpolation error and the finite aperture. Regardless of the limit in resolution caused by evanescent waves, the limit in quality due to the Born and the Rytov approximations still exist.

5.4.1 Limitation of the Wave Propagation

The most fundamental limitation is that evanescent waves are ignored. Since these waves have a complex wave number, they are severely attenuated and phase delayed over a distance as short as a wavelength. This sets the upper limit of the wave number to

$$k_{\max} = \frac{2\pi}{\lambda} \ . \tag{5.29}$$

This also leads to a fundamental limit of the propagation process, and the range resolution of the SPA reconstruction. These can be improved by conducting the ultrasonic identification at a higher operation frequency (or shorter wavelength).

After the wave has been scattered by the target and received by the receiver, the signal must be detected and processed. Unfortunately, it is not possible to sample at every point, so a non-zero interval must be chosen. This introduces an interpolation error into the process. By the Nyquist theorem this can be modeled as a low-pass filtering operation, where the highest evaluated propagation delay, as defined in Eq. (3.63), is given by

$$\tau_{\max} = \frac{\pi}{\Delta\omega} \tag{5.30}$$

and $\Delta\omega$ is the sampling interval. Of course this analysis has ignored the non-linear properties of wave number and the resulting frequency shifts that occur.

5.4.2 Effect of a Finite Receiving Region

Not only are there physical limitations on the finest sampling interval, there is usually a limitation on the region that can be covered. This generally means that signals of the received waveform will be collected at only a portion of signal energy in the receiver region. Consider a single scatterer which is located at the far-zone field region. The wave propagating from this single scatterer is a cylindrical wave in two dimensions or a spherical wave in three dimensions. This effect is depicted in Figure 5.5. It is easier to analyze the effect by considering the expanding wave to be locally planar at any given point from the scatterer. This can be justified on a more analytical basis by evaluating the phase of the propagating wave. The received wave at a point $(x = x_s, y_s)$ due to a scatterer at the origin is given by

$$u(x,y) = \frac{e^{jk_o\sqrt{x^2+y^2}}}{\sqrt{x^2+y^2}} \ . \tag{5.31}$$

This instantaneous spatial frequency along the receiver region $(x_s - \Delta \le x \le x_s + \Delta, y_s - \Delta y \le y \le y_s + \Delta)$ can be found by taking the spatial derivative of the phase with respect to y [80]

$$\text{phase} = k_o\sqrt{x^2+y^2} \tag{5.32}$$

and

$$k_{rec} = \frac{k_o y}{\sqrt{x^2 + y^2}} \tag{5.33}$$

where k_{rec} is the spatial frequency received at the point (x,y). From Figure 5.5, it is easy to see that

$$\tan\theta = \frac{y}{x} , \tag{5.34}$$

and we obtain

$$k_{rec} = \frac{k_o \frac{y}{x}}{\sqrt{(\frac{y}{x})^2 + 1}} = \frac{k_o \tan\theta}{\sqrt{\tan^2\theta + 1}} . \tag{5.35}$$

Thus, k_{rec} is a monotonically increasing function of the angle of view θ. It is easy to see that the maximum received energy can be increased by either moving the receiver closer to the focus line of the object or by increasing the region of the receiver.

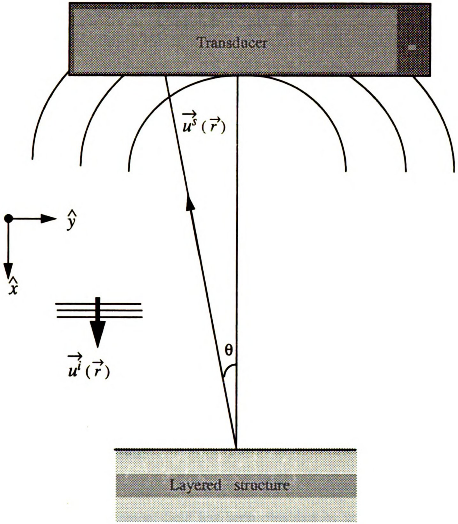

Figure 5.5 : The field scattered by a layered structure is measured along a transducer region with finite dimension.

CHAPTER 6

ULTRASOUND FIELD WITHIN AN ARBITRARILY SHAPED AND INHOMOGENEOUS SCATTERER

6.1 Introduction

In certain applications, it is desirable to gain the knowledge of the ultrasound field distribution inside a medium. For example, in hyperthermia treatment of tumors [81 - 83], the induced temperature profile is directly related to the ultrasound field distribution. Therefore, knowledge of the field distribution plays an extremely important role in the success of treatments.

Much work has been reported on the evaluation of scattered acoustic fields [84 - 87]. Specifically, the displacement field has been obtained by computing the scattering integral in which the dyadic Green's function has been used [88 - 90]. However, the field distribution inside the scatterer has not been investigated extensively due to the fact that the boundary conditions of an arbitrarily shaped scatterer are rather complicated. Without knowing the internal field distribution, it is virtually impossible to determine the heat generation and, consequently, the temperature profile inside the medium structure.

Most of the work published in evaluating the internal field of a medium has been confined to the case of planar layered media with homogeneous and uniform attenuation properties [91 - 93], because of their simple in boundary conditions. In other areas, such as the case of underwater acoustics or seismology, one can ignore the boundary conditions because a large-scale problem is being considered [94 - 96]. Recent studies show that the scattering effect of a scatterer, embedded in an inhomogeneous layered structure, can be solved by using the dyadic Green's function with the Born approximation [97 - 99]. However, field distribution within the scatterer that remains unsolved could due to the existence of singularity in the integral equation.

In this chapter, we seek to relax the restrictive assumptions commonly made on the medium and to design a novel approach to avoid the singularity of the integration. The outline of the chapter is as follows: (1) In the next section, we develop a general 3-D forward scattering formulation [100] for the purpose of evaluating the scattered field of an arbitrarily shaped scatterer. Then, we decompose the displacement field into an incident field and a scattered field of interest. The incident field results from the original excitation in the background medium on the absence of the scatterer whereas the scattered field results from the scatterer. (2) In Section 6.3, we consider an arbitrarily shaped medium embedded in a homogeneous background (such as water), and develop an expression for the 3-D displacement field induced by a plane ultrasonic wave. We then use the proposed technique to preset the coefficients of the transform matrix in Section 6.4. Finally, four simulations are performed. The results show that the fields obtained from the proposed technique are reasonable over a wide range of pixel dimensions.

6.2 Integral Representation of the Scattered Field

Consider a finite scatterer of arbitrary dimension, with the density $\rho_m(\vec{r})$ and the compressibility $c_m(\vec{r})$, illuminated in a background medium (such as water) by a compressional plane ultrasonic wave as shown in Figure 6.1. The induced ultrasonic force in the scatterer gives rise to a scattered ultrasound displacement field $\vec{u}^s(\vec{r})$, which might be accounted for by replacing an equivalent background force density function $\vec{f}_{eq}(\vec{r})$ [101]

$$\begin{aligned} \vec{f}_{eq}(\vec{r}) &= -\left[\omega^2\rho_m(\vec{r}) - \omega^2\rho_o\right]\vec{u}(\vec{r}) \\ &= -\left[c_m(\vec{r})k_m^2(\vec{r}) - c_o k_o^2\right]\vec{u}(\vec{r}) \\ &= -\left[\frac{c_m(\vec{r})k_m^2(\vec{r})}{c_o k_o^2} - 1\right]\left[c_o k_o^2\right]\vec{u}(\vec{r}) \\ &= -n(\vec{r})\left[c_o k_o^2\right]\vec{u}(\vec{r}) \\ &= -m(\vec{r})\,\vec{u}(\vec{r}) \ . \end{aligned} \tag{6.1}$$

The wave number $k_m(\vec{r}) = \beta_m(\vec{r}) - j\alpha_m(\vec{r})$ is a complex quantity governed by the nature of the scatterer. The velocity in the medium is $\upsilon_m(\vec{r}) = \left[\frac{c_m(\vec{r})}{\rho_m(\vec{r})^{1/2}}\right] = \frac{\omega}{\beta_m(\vec{r})}$, $\alpha_m(\vec{r})$ is the attenuation coefficient, and ρ_o and c_o are the density and compressibility of the background medium respectively. Moreover, $n(\vec{r})$ is the complex deviation ratio of the scatterer and the background, as defined in Eq. (6.1), and $\vec{u}(\vec{r})$ is the total displacement field inside the scatterer.

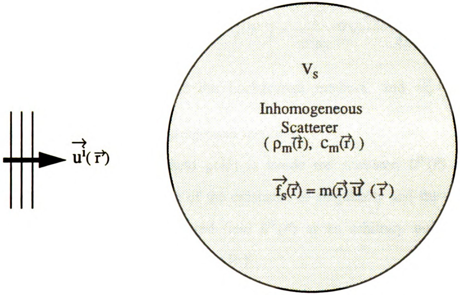

$$\vec{u}(\vec{r}) = \vec{u}^i(\vec{r}) + \vec{u}^s(\vec{r})$$

Figure 6.1 : An inhomogeneous scatterer insonified by a plane ultrasonic wave.

In general, the scattered displacement field $\vec{u}^s(\vec{r})$ inside the scatterer can be expressed in terms of $\vec{f}_{eq}(\vec{r})$ by the use of the dyadic Green's function $\overleftrightarrow{G}(\vec{r}|\vec{r}\,')$ as follows [102]:

$$\vec{u}^s(\vec{r}) = \int_V \vec{f}_{eq}(\vec{r}\,') \cdot \overleftrightarrow{G}(\vec{r}|\vec{r}\,')dv' \tag{6.2}$$

where the dyadic Green's function, $\overleftrightarrow{G}(\vec{r}|\vec{r}\,') = \dfrac{1}{\omega^2\rho_o}\nabla\nabla\dfrac{exp(-j\vec{k}_o \cdot (\vec{r}-\vec{r}\,'))}{4\pi|\vec{r}-\vec{r}\,'|}$, represents the transfer function of the background medium, and $|\vec{k}_o| = \omega\left[\dfrac{\rho_o}{c_o}\right]^{1/2}$ denotes the wave number of the background medium.

In this case in which the field point is inside the scatterer, $\vec{u}^s(\vec{r})$ should be evaluated with special care because of the existence of singularity and the requirement of uniqueness properties. The scattered field $\vec{u}^s(\vec{r})$ at an arbitrary point inside the scatterer can be written as (see Appendix B)

$$\vec{u}^s(\vec{r}) = PV \int_V \vec{f}_{eq}(\vec{r}\,') \cdot \overleftrightarrow{G}(\vec{r}|\vec{r}\,')dv' - \frac{\vec{f}_{eq}(\vec{r})}{3\omega^2\rho_o} \tag{6.3}$$

where the symbol "PV" denotes the principal value of the integral. We may now write the total ultrasonic displacement field $\vec{u}(\vec{r})$ inside the scatterer as the sum of the incident field $\vec{u}^i$ and the scattered field $\vec{u}^s$ as

$$\vec{u}(\vec{r}) = \vec{u}^i(\vec{r}) + \vec{u}^s(\vec{r}) \ . \tag{6.4}$$

Substituting Eq. (6.3) into Eq. (6.4) and rearranging terms gives the integral equation for $\vec{u}(\vec{r})$:

$$\left[1 - \frac{m(\vec{r})}{3\omega^2\rho_o}\right]\vec{u}(\vec{r}) + PV \int_V m(\vec{r}\,')\vec{u}(\vec{r}\,') \cdot \overleftrightarrow{G}(\vec{r}|\vec{r}\,')dv' = \vec{u}^i(\vec{r}) \ . \tag{6.5}$$

In Eq. (6.5), $\vec{u}^i(\vec{r})$ is the incident ultrasonic field and is considered to be a known quantity. $\vec{u}(\vec{r})$ is the unknown total ultrasonic field inside the scatterer, which can be discretized to yield a linear system of equations with complex coefficients.

6.3 Evaluation Procedure

Assuming that $\vec{u}(\vec{r})$ and $m(\vec{r})$ are smoothly-varying functions of space within the volume of the scatterer, we can partition the medium into N pixels, and treat $\vec{u}(\vec{r})$ and $m(\vec{r})$ as constants in each pixel. Under these assumptions, the integral Eq. (6.5) can be transformed into a linear system problem.

Denoting the m^{th} sub-volume by V_m and the position of V_m by $\vec{r}_m$, we can rewrite Eq. (6.5) using $x_1 = x$, $x_2 = y$, and $x_3 = z$, as

$$[1 - \frac{m(\vec{r}_m)}{3\omega^2\rho_o}]\, u_{x_p}(\vec{r}_m) + \sum_{q=1}^{3}\sum_{n=1}^{N}\Big[m(\vec{r}_n) \tag{6.6}$$

$$\cdot\, PV \int_{V_n} G_{x_p x_q}(\vec{r}_m|\vec{r}\,')\, dV'\Big]\, u_{x_q}(\vec{r}_n) = u^i_{x_p}(\vec{r}_m)$$

where p, q = 1, 2, 3 and

$$G_{x_p x_q}(\vec{r}_m|\vec{r}\,') = \frac{j}{\omega^2\rho_o}\frac{\partial^2}{\partial x_q \partial x_p}\left[\frac{exp(-j\vec{k}_o\cdot(\vec{r}_m-\vec{r}\,'))}{4\pi|\vec{r}_m-\vec{r}\,'|}\right] . \tag{6.7}$$

For simplicity, one can define

$$A^{mn}_{x_p x_q} = m(\vec{r}_n)\cdot PV \int_{V_n} G_{x_p x_q}(\vec{r}_m|\vec{r}\,')\, dV' . \tag{6.8}$$

Then Eq. (6.6) becomes

$$\sum_{q=1}^{3}\sum_{n=1}^{N}\left[A^{mn}_{x_p x_q} + \delta_{pq}\delta_{mn}\left[1 - \frac{m(\vec{r}_m)}{3\omega^2\rho_o}\right]\right] u_{x_q}(\vec{r}_n) = u^i_{x_p}(\vec{r}_m) , \tag{6.9}$$

$$m = 1, 2, ..., N \quad \text{and} \quad p, q = 1, 2, 3.$$

Denoting $\left[\tilde{A}_{x_p x_q}\right]_{N\times N}$ as a matrix, its elements are assigned by

$$\tilde{A}^{mn}_{x_p x_q} = A^{mn}_{x_p x_q} + \delta_{pq}\delta_{mn}\left[1 - \frac{m(\vec{r}_m)}{3\omega^2\rho_o}\right] \tag{6.10}$$

where $m, n = 1, 2, \ldots, N$ and $p, q = 1, 2, 3$. $\left[u_{x_p}\right]$ and $\left[u^i_{x_p}\right]$ are N-dimensional vectors which are given by

$$\left[u_{x_p}\right] = \begin{bmatrix} u_{x_p}(\vec{r}_1) \\ \cdot \\ \cdot \\ \cdot \\ u_{x_p}(\vec{r}_N) \end{bmatrix} \quad \text{and} \quad \left[u^i_{x_p}\right] = \begin{bmatrix} u^i_{x_p}(\vec{r}_1) \\ \cdot \\ \cdot \\ \cdot \\ u^i_{x_p}(\vec{r}_N) \end{bmatrix} \tag{6.11}$$

where p = 1, 2, 3. For all possible values of m and p in Eq. (6.10), the matrix representation of Eq. (6.9) is obtained as

$$\begin{bmatrix} [\tilde{A}_{xx}] & [\tilde{A}_{xy}] & [\tilde{A}_{xz}] \\ [\tilde{A}_{yx}] & [\tilde{A}_{yy}] & [\tilde{A}_{yz}] \\ [\tilde{A}_{zx}] & [\tilde{A}_{zy}] & [\tilde{A}_{zz}] \end{bmatrix} \begin{bmatrix} [u_x] \\ [u_y] \\ [u_z] \end{bmatrix} = \begin{bmatrix} [u^i_x] \\ [u^i_y] \\ [u^i_z] \end{bmatrix} \tag{6.12a}$$

$$\text{or} \quad \left[\tilde{A}\right]\left[u\right] = \left[u^i\right] \tag{6.12b}$$

where $\left[\tilde{A}\right]$ is a $3N\times 3N$ matrix, while $\left[u\right]$ and $\left[u^i\right]$ have dimension 3N expressing the total displacement field and the incident displacement field at the centers of the N pixels.

Notice that in this way, a 3-D image matrix is represented by a 1-D vector stacked by rows. The inverse problem becomes that of determining the total ultrasound displacement field $\vec{u}(\vec{r})$ from the measurements $\vec{u}^{\,i}(\vec{r})$. Therefore, one may evaluate the field distribution inside the medium by solving the Eq. (6.12) with available methods [103 - 105].

6.4 Determination of Transformation Matrix Elements

In order to evaluate the coefficients of the matrix $\left[\tilde{A}_{x_p x_q}\right]$, one must be careful in calculating the principal value of Eq. (6.8). Examining the off-diagonal elements of $\left[\tilde{A}_{x_p x_q}\right]$, we clearly see that r_m does not belong to V_n, and $G_{x_p x_q}(\vec{r}_m | \vec{r}\,')$ is continuous throughout V_n . Therefore, we may omit the principal value operation from our evaluations. However, when we deal with the diagonal elements of $\left[\tilde{A}_{x_p x_q}\right]$, r_m now belongs to V_n , and we need to make some approximations.

6.4.1 Off-Diagonal Elements

First let us consider the off-diagonal elements of $\left[\tilde{A}_{x_p x_q}\right]$, where p, q = 1, 2, 3. From Eq. (6.9), it is clear that

$$\tilde{A}^{mn}_{x_p x_q} = A^{mn}_{x_p x_q} = m(\vec{r}_n) \cdot \int_{V_n} G_{x_p x_q}(\vec{r}_m | \vec{r}\,')dv' \quad ; \; m \neq n \; . \tag{6.13}$$

With the same approximation described in Section 6.3, we have

$$\tilde{A}^{mn}_{x_p x_q} = A^{mn}_{x_p x_q} = m(\vec{r}_n)G_{x_p x_q}(\vec{r}_m | \vec{r}_n)\Delta V_n \quad ; \; m \neq n \; , \tag{6.14}$$

where $\Delta V_n = \int_{V_n} dV'$. Using the definition of Eq. (6.7), we can rewrite Eq. (6.14) as

$$\tilde{A}^{mn}_{x_p x_q} = \frac{1}{\omega^2 \rho_o} m(\vec{r}_n)\, \Delta V_n \frac{exp(-jk_o R_{mn})}{4\pi R^3_{mn}} \left\{ \frac{(x^m_p - x^n_p)}{R_{mn}} \frac{(x^m_q - x^n_q)}{R_{mn}} \right. \tag{6.15}$$

$$\left. \cdot \left[3 - (k_o R_{mn})^2 + j3k_o R_{mn}\right] - (1 + jk_o R_{mn})\delta_{pq} \right\} \quad ; \; m \neq n \; ,$$

where $R_{mn} = |\vec{r}_m - \vec{r}_n|$, while $\vec{r}_m$ and $\vec{r}_n$ are denoted

$$\vec{r}_m = \hat{x}\, x^m_1 + \hat{y}\, x^m_2 + \hat{z}\, x^m_3 \; , \text{ and } \quad \vec{r}_n = \hat{x}\, x^n_1 + \hat{y}\, x^n_2 + \hat{z}\, x^n_3 \; . \tag{6.16}$$

When N is chosen properly, reasonable results can be obtained by using Eqs. (6.14) and (6.15). For better accuracy, however, Eq. (6.13) should be integrated numerically by any conventional method.

6.4.2 Diagonal Elements

For the diagonal elements of $\left[\tilde{A}_{x_p x_q}\right]$ in Eq. (6.9), we have

$$\tilde{A}^{nn}_{x_p x_q} = m(\vec{r}_n)\cdot PV \int_{V_n} G_{x_p x_q}(\vec{r}_n | \vec{r}\,')dv' + \delta_{pq}\left[1 - \frac{m(\vec{r}_n)}{3\omega^2\rho_o}\right] \tag{6.17}$$

$$= m(\vec{r}_n)\cdot \lim_{\varepsilon\to 0} \int_{V_n - V_{n\varepsilon}} G_{x_p x_q}(\vec{r}_n | \vec{r}\,')dv' + \delta_{pq}\left[1 - \frac{m(\vec{r}_n)}{3\omega^2\rho_o}\right] .$$

For better accuracy, the volume V_n has been approximated as a sphere having the same volume as the cubic pixel which is centered at r_n. Now, let a_n be the radius of the sphere, after steps of manipulation (see Appendix C), Eq. (6.17) becomes

$$\tilde{A}^{nn}_{x_p x_q} \approx \delta_{pq}\left\{\frac{-m(\vec{r}_n)}{3\omega^2\rho_o}\left[(1 + jk_o a_n)\, exp(-jk_o a_n) - 1\right] + \left[1 - \frac{m(\vec{r}_n)}{3\omega^2\rho_o}\right]\right\} \tag{6.18}$$

where $a_n = \left[\frac{3\Delta V_n}{4\pi}\right]^{1/3}$. If the actual shape of V_n differs appreciably from that of a sphere, the approximation may lead to errors. In such a case, the integration throughout a small sphere surrounding r_n should be performed by procedures outlined in Appendix C; the integration throughout the remainder of V_n must be carried out numerically.

6.5 Computer Simulation

Numerical simulations of some simple composite models are performed to test the validity of the theory developed. Other models will also be used to explore the scattering effects within an arbitrarily shaped inhomogeneous medium.

6.5.1 Dimension of Pixels

When using a discretized pulse expansion in a linear system of equations, it is crucial to establish a suitable limitation on the dimensions of the sub-volumes. In order to arrive at an optimal choice, we consider a homogeneous bar with a deviation ratio of $n(\vec{r}) = 10$, as shown in Figure 6.2a, illuminated by a 1 MHz plane wave with unit strength. Expressed in wavelengths, the dimensions of the this homogeneous bar is $6 \times \frac{1}{2} \times \frac{1}{2} \lambda^3$.

When the homogeneous medium is partitioned into cubical pixels, the induced field can be evaluated in each pixel. Models having different pixel numbers ($N = 12$, $N = 96$, and $N = 324$), with dimensions of $\frac{1}{2}\lambda$, $\frac{1}{4}\lambda$, and $\frac{1}{6}\lambda$ respectively, are used in this study. Computational results confirm with our assumption that the induced ultrasound field is dominantly the x component.

Figure 6.2b shows the axial ultrasound fields along the $\hat{z}$-axis for each model. For the $\frac{1}{2}\lambda$ case, the field intensity distribution deviates noticeably from the other two cases. This is because too large a pixel dimension was chosen. For the $\frac{1}{4}\lambda$ and $\frac{1}{6}\lambda$ cases, the fields are symmetrical to the axial axis. A standing wave pattern is established along the plate due to the finite boundary condition. Since none of the pixels, as shown in the $\frac{1}{4}\lambda$ case, lies along the $\hat{z}$-axis, we plotted the average field intensity in its surroundings to facilitate a comparison with the cases of $\frac{1}{2}\lambda$ and $\frac{1}{6}\lambda$. The

results indicate that pixels with dimension of $\frac{1}{4}\lambda$ produce quite an accurate field distribution; it is therefore not necessary to choose yet smaller pixel sizes.

We have also investigated the effects of frequency and deviation ratio upon the field distributions. A small cube ($1.5 \times 1.5 \times 1.5$ mm^3) with the combinations of different harmonic frequencies and deviation ratios was used. Since the cube presents a symmetrical cross-section to the incident field, we only need to evaluate the induced field in one quadrant. The results are summarized in Table 6.1. We observe that the field strength at the center of the cube is nearly independent of the harmonic frequency but is highly dependent on the deviation ratio.

Table 6.1 : The central displacement field of a ($1.5 \times 1.5 \times 1.5$ mm^3) homogeneous cube with various *n(r)*, insonified by a plane ultrasonic wave of different harmonic frequencies.

f_o (*MHz*)	λ_o (mm)	*n(r)*	λ_m (mm)	Displacement field *u (r)* at cubical center
1	1.5	0.5	2.25	$u_x = 0.1078 - j\,0.0708$ $u_y = 0.0179 - j\,0.0021$ $u_z = u_y$
0.1	15	0.5	22.5	$u_x = 0.1065 - j\,0.0853$ $u_y = 0.0207 - j\,0.0053$ $u_z = u_y$
0.1	15	5.0	90.0	$u_x = -0.0468 + j\,0.0102$ $u_y = -0.0021 + j\,0.0013$ $u_z = u_y$
0.1	15	50.0	765	$u_x = -0.0036 + j\,0.0003$ $u_y = -0.0008 + j\,0.0003$ $u_z = u_y$

Note : $\upsilon_o = (c_o / \rho_o)^{1/2}$ and $\upsilon_m(r) = (c_m(r) / \rho_m(r))^{1/2}$

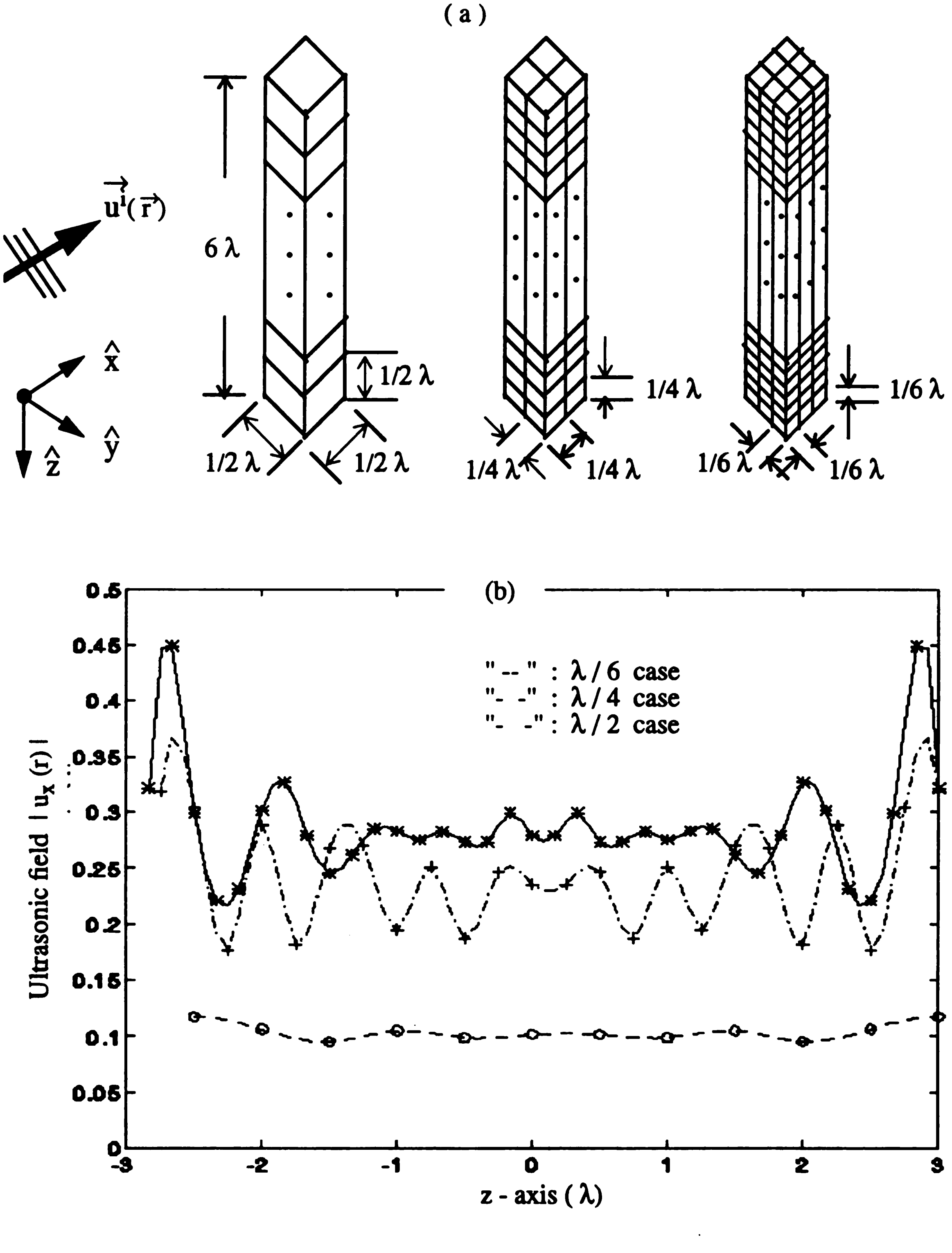

Figure 6.2 : (a) Three different configurations of a homogeneous bar with $n(r) = 10$, $f = 1$ MHz, and (b) The ultrasonic field $u_x(r)$ versus the z axis.

6.5.2 Evaluation of Inhomogeneous Field Distributions

Two models composed of biological materials with their properties given in Table 6.2 [106] are used in our simulation.

Table 6.2 : Specified values of tissue properties, under a harmonic frequency of 1 *MHz* used in the computational simulations.

Biological material	Velocity (m/sec)	Attenuation (Np/m)	density (kg/m^3)
fat	1445 (1440 -1490)	7 (5 - 9)	921
muscle	1570 (1500 - 1630)	9 (4.5 - 15)	1138

(1) Model A : fat-muscle plate.

(2) Model B : fat-muscle-fat bar.

For the planar model, as shown in Figure 6.3a, we set the incident ultrasonic field to be perpendicular to the surface of the model (i.e., $\hat{x}$-axis). From the results of the previous section, no transverse components need to be considered since we are using a purely longitudinal ultrasonic wave.

The fat-muscle square plate has a dimensions $4.5 \times 4.5 \times .75\ mm^3$. The distributions of the ultrasound field inside both layers, versus the $\hat{y}$- and $\hat{z}$- axes, are shown in Figure 6.3b. As expected, the field distributions at the fat-muscle interface are discontinuous due to the difference of their acoustic impedances. The field intensity is higher in the fat region than in the muscle region. Figure 6.4a shows the 13.5 *mm* long bar of fat with a 1.125 *mm* layer of muscle in its center. The axial field distribution is shown in Figure 6.4b. It can easily be seen that the field contains a forward propagation and a reflected component. These waves attenuate exponentially as they travel. As a result, a standing wave pattern is established between the boundaries. For a homogeneous medium, the field intensity is the lowest at the middle of the structure. This is expected, since no boundary exists inside the structure which could cause reflections to trap acoustic energy. On the other hand, structures composed of different materials could produce a local maximum in the field intensity distribution.

In addition, if one wants to evaluate the acoustic power variation within a medium, one can relate power to pressure variation. The acoustic pressure can be expressed as a linear function of the phase constant β as

$$p(\vec{r}) = \rho_m(\vec{r})\frac{\partial u(\vec{r})}{\partial t} = j\omega\rho_m(\vec{r})u(\vec{r}) = j\beta_m(\vec{r})Z_m(\vec{r})u(\vec{r}) \tag{6.19}$$

where $Z_m(\vec{r}) = \rho_m(\vec{r})\upsilon_m(\vec{r})$ is the acoustic impedance and $\upsilon_m(\vec{r})$ is the acoustic velocity in the medium. The power absorbed by the medium is

$$\text{Power}(\vec{r}) = \mu_{ab}\left[\frac{|p(\vec{r})|^2}{Z_m(\vec{r})}\right] \tag{6.20}$$

where μ_{ab} is the absorption coefficient [107].

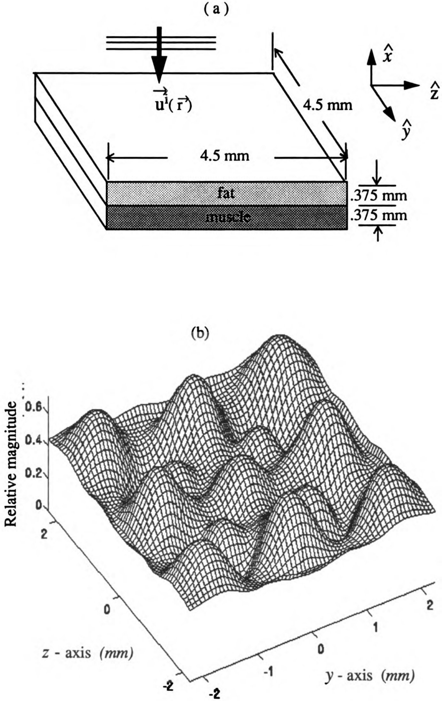

Figure 6.3 : (a) Configuration of a fat-muscle plate, (b) The field distribution of the fat plate, and (c) The field distribution of the muscle plate, as a function of spatial locations in y - z plane. (to be cont'd)

Figure 6.3 (cont'd)

(c)

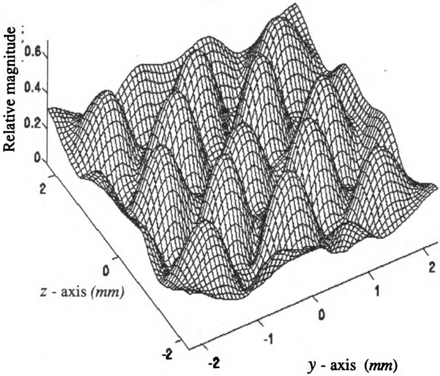

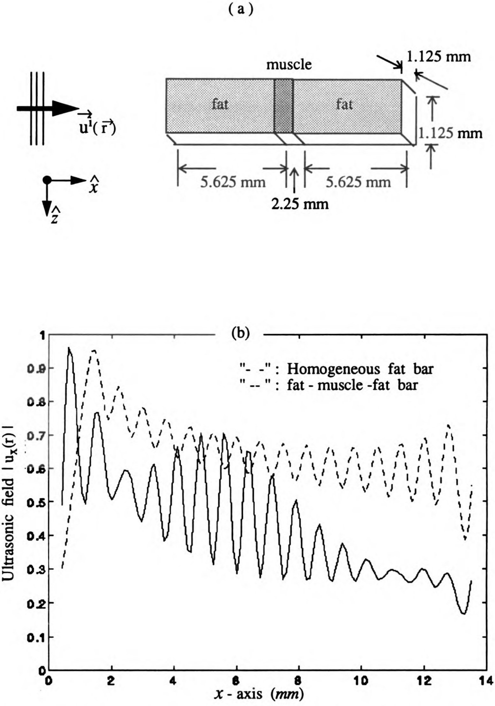

Figure 6.4 : (a) Configuration of a fat-muscle-fat bar, and (b) The x component of the ultrasonic field as a function of the axial distance.

In this chapter, we have developed a method to determine the acoustic field distribution around and inside a scatterer. A dyadic Green's function has been used in the evaluation process. A special arrangement to handle the singularity in the Green's function integration has also been demonstrated. Two models of simple structures made of biological materials are used in the field distribution analysis. In choosing the pixel size for computer simulation, it is obvious that a smaller pixel size will give a more accurate result. However, computing time increases with decreasing pixel size. We found that a pixel size of $\frac{1}{4}\lambda$ cube gives acceptable results with a reasonable computing effort.

In most of the published work, the factor $e^{-\alpha x}$ is attached to the field solution to account for attenuation. The present analysis indicates that the attenuation and phase characteristics should be properly handled as a complex propagation factor throughout the analysis.

It is interesting to note that the power absorbed in the muscle region of an inhomogeneous bar is several times larger than that absorbed by the surrounding fat layers. Specifically, a material with high field attenuation and high mass density will absorb more power and consequently reaches a high temperature. A good example is the case of hyperthermia treatment of tumors. A tumor has a high mass density and higher attenuation than the surrounding soft tissues. Together with the fact that a tumor site has poor blood circulation, its temperature could easily exceed the cell survival level under ultrasonic irradiation.

CHAPTER 7

EXPERIMENTS

7.1 Introduction

This chapter has two main purposes. The first is to present experimental justification for using the IPM concept to reconstruct an object's scattered field. This is accomplished by comparing the acoustic properties of a thin plexiglass layer obtained from time-domain measurements of the reflected waveform. A verification of the dimensional independence of material properties will also be given, via time-domain measurements taken from different layer thicknesses. Note that each of these tasks requires the utilization of natural mode extraction scheme, and thus also provides a practical test for the techniques of Chapter 5.

Second, with the legitimacy of the IPM concept strengthened by empirical observation, an experimental verification of the SPA algorithm is sought. This is accomplished by using the reflected waveform measurements of two multi-layered models -- a plexiglass-aluminum and a plexiglass-copper model.

7.2 Experiment Facility and Measurement System

A system for measuring the time-domain reflected waveform of layered structures has been built at the MSU ultrasonic laboratory. A schematic representation of the measurement equipment utilized in ultrasonic interrogation is shown in Figure 7.1.

Target excitation is provided by an incident ultrasonic wave radiated by a transmitter (S/N: MD306) suspended over a water tank. The transducer has an axial focal length of 2 *cm*, a radius of 1.27 *cm*, and a characteristic impedance of 50 Ω. It transmits a pulsed longitudinal wave which approximates a pulsed plane wave propagated perpendicular to the surface of the target. Reception of the ultrasonic field reflected by a layered target is also received by the same transducer.

The transducer (S/N: MD306) is driven by a Panametrics 5050PR pulser, which provides a quasi-Gaussian pulse of approximately 5 *μs* duration at a rate of 800 *Hz*. Electronic gains and power levels can be adjusted on the pulser panel. Since the transducer is designed for a specified frequency, the spectrum of the ultrasonic wave pulse is transmitted with a Gaussian shape centered at 2.25 *MHz* (bandwidth: 1.5 *MHz*).

Channel 2 of a Tektronix 466 storage oscilloscope measures the signal from the ultrasonic transducer, while channel 1 of the scope is optionally connected to a trigger output located at the pulser for timing purposes. A waveform acquisition board (Waag II) interfaces the sampling reflected signal with an IBM-PC computer, which acquires the measured data under software control. Each of the reflected waveforms is accessed through input channel A in the waveform acquisition board.

Once measurements have been obtained and stored in microcomputer memory, they can be processed and placed on local hard disk or transmitted via modem to the MSU mainframe computer system.

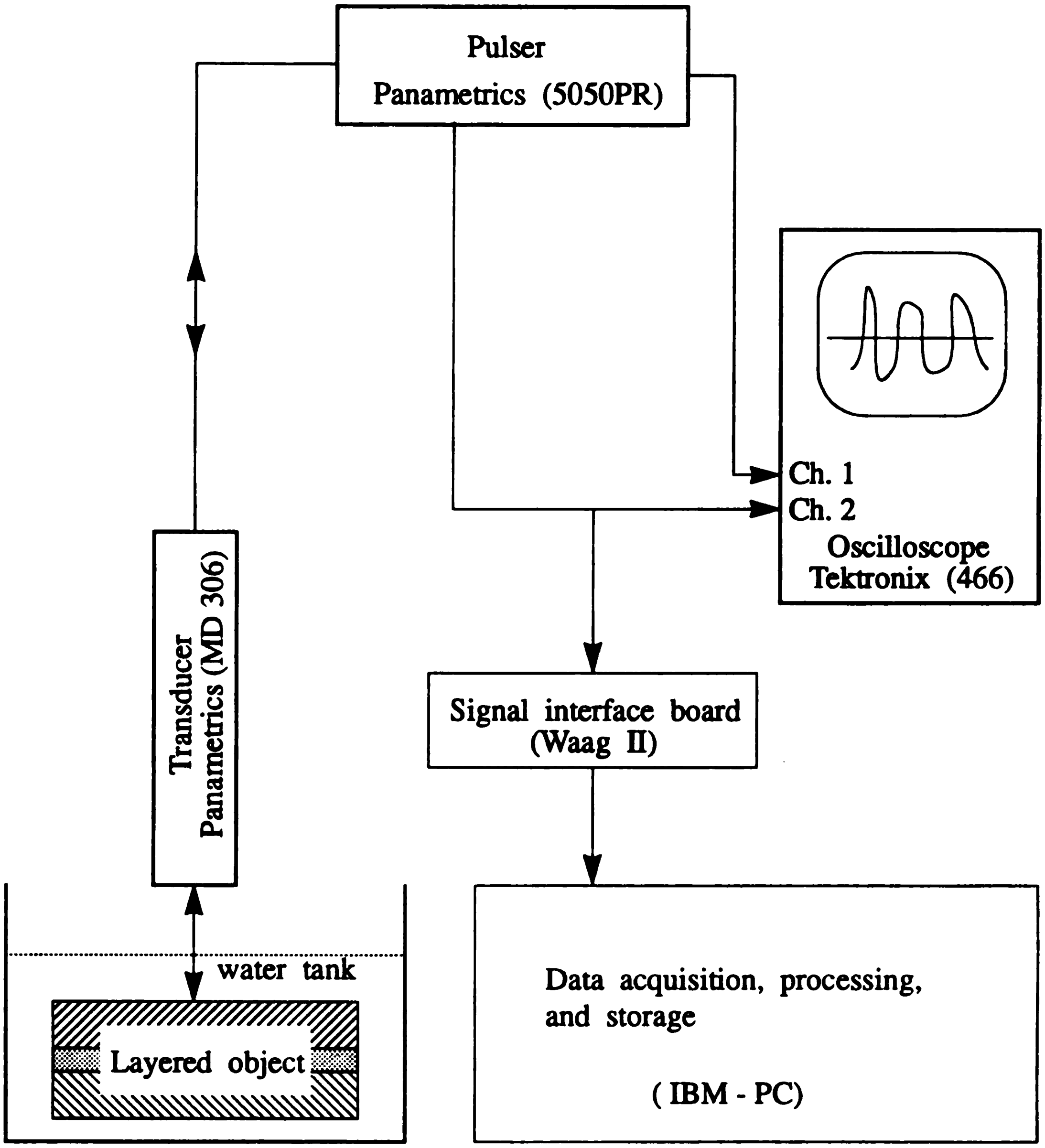

Figure 7.1 : Schematic representation of the Ultrasonic Interrogation System.

7.3 Data Acquisition and Processing Procedure

As mentioned in the previous section, reception of the layered object reflected waveform is provided by means of a single transducer. The reason for using such a transducer is that its simplified configuration can easily be modeled. Moreover, there is no need to be concerned about the timing and amplitude differences between the transmitter and receiver.

Generally, the measured signals are unavoidably corrupted by the presence of random noise. To overcome this problem, the data acquisition process involves making repeated measurement runs and averaging the results. This has been found to increase the signal to noise ratio considerably. However, inconsistencies in the measurements between runs due to triggering jitter, inaccurate reproduction of sampling density, and drift of the preamplifier characteristics and the external power supply voltage necessitate the implementation of fairly sophisticated data acquisition and processing software.

Figure 7.2 shows a typical trace on the sampling reflected waveform, displaying the reflected waveform from the testing object. Because the A/D converter will only accept voltage values between –5 and +5 volts, the first large positive going and negative going peaks of the reflection response must be adjusted so that any portion of the trace to be measured falls within this range. The amplifier gain on the pulser is turned up to near maximum on the signal trace channel, to accentuate the steady-state portion of the reflection waveform.

Figure 7.3 shows a flowchart of the data acquisition and processing routines. The data acquisition phase consists of making multiple (usually 128) separate traces. The sampling density is adjusted such that each data run takes roughly 10 ms to complete. It is important that the sampling density be high enough for the layered structure's response to be accurately reproduced. Data acquisition software (a C-program) allows the selection of an A/D converter sampling rate of up to 40 MHz. However, the amount of available PC memory puts a limit on the number of points allowed in each data run.

The data acquisition phase begins by running the C-program SCAN5. This program controls the A/D converter and interfaces with the experimenter via keyboard control. It then loops through the entire data acquisition process N times. After the data run is finished, the computer gives the operator the option of repeating the run (in case of problems incurred during the sweep), viewing the acquired data, resetting the time-domain window size, and/or writing the data to a floppy disk. It is important to keep the disk writing time to a minimum in order to make the entire data acquisition process as short as possible, because this minimizes the amount of transducer drifting between data runs.

Data processing begins by averaging the subsequent data sets and then subtracting the DC offset. If satisfactory processing of all the data sets results in a high signal-to-noise ratio and differentiated response of the layered structure, this response is finally written to hard disk as the processed data.

At any point in the data analysis, the C-program DATAPLOT allows the plotting of a disk file data set on the CRT screen, and also allows a hard copy to be printed. Moreover, it contains a program employing the fast Fourier transform algorithm [108] to obtain the Fourier spectrum of a disk file data set. This allows a preliminary discrimination of the imaginary parts of the object's natural modes, which can then be used as initial guesses in the more sophisticated natural mode extraction schemes of Chapter 4.

One main goal of all the data processing routines discussed is to accomplish as much as possible in the laboratory using the IBM-PC computer. At this time, everything but the natural mode extraction schemes can be completed quite rapidly in the laboratory.

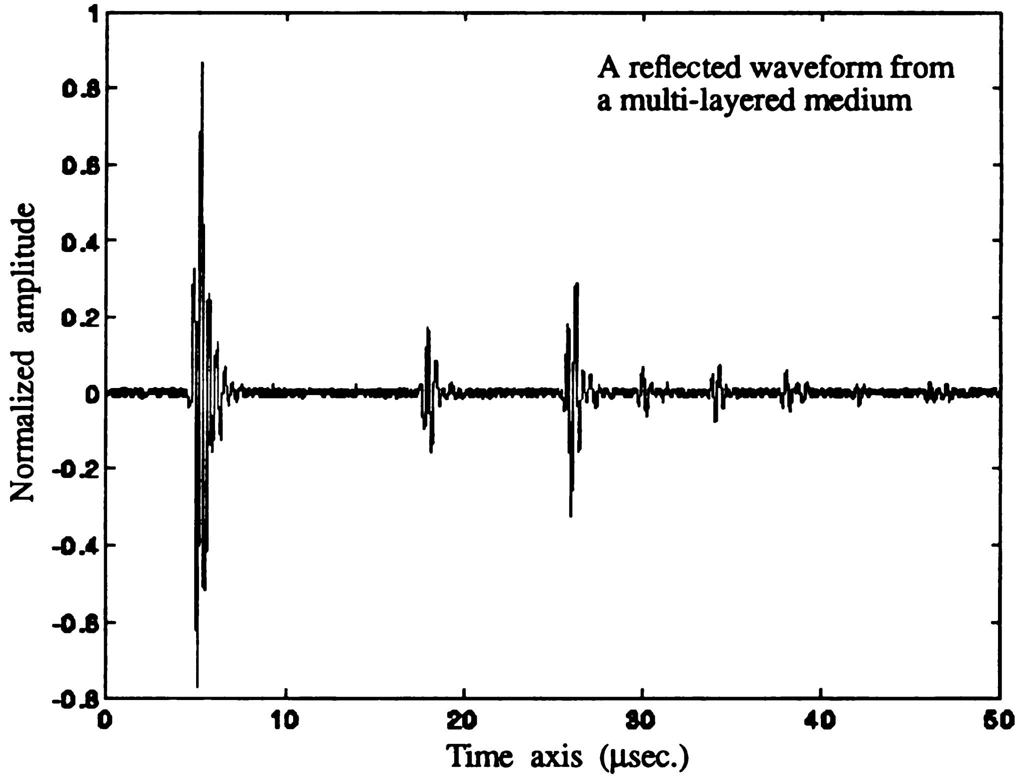

Figure 7.2 : Typical layered structure trace of a reflection waveform insonified by a quasi-Gaussian pulsed ultrasonic source.

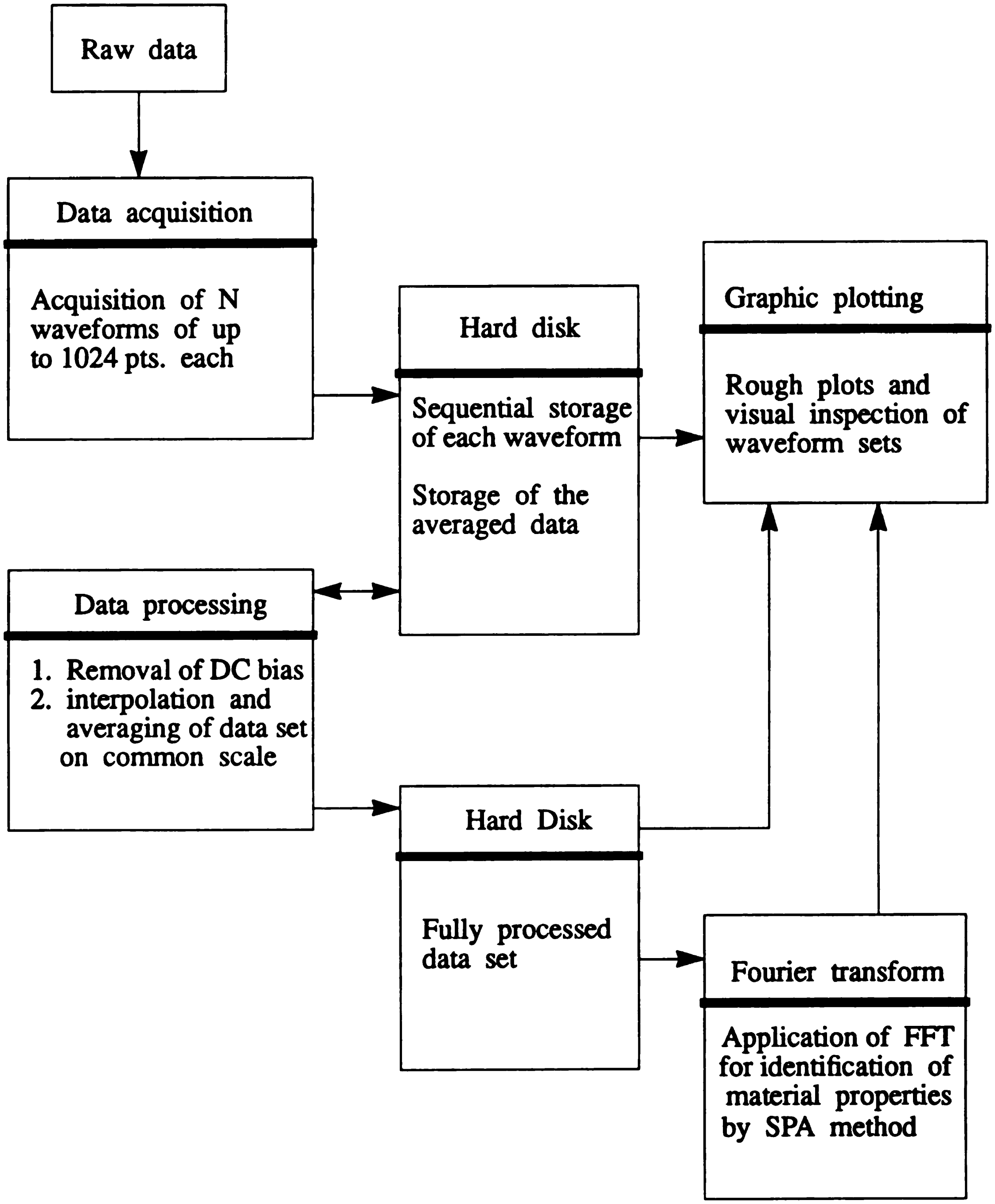

Figure 7.3 : Flowchart for IBM-PC controlled data acquisition and processing.

7.4 Experimental Investigation of IPM Validity

The SPA concept discussed in this thesis is based entirely upon the hypothesis that the steady-state scattered field response of a layered structure can be written as in Eq. (3.79) -- that is, it can be represented completely by a series of natural-resonance-based damped sinusoid functions. If this expansion is not correct, or if it is not complete, then the SPA scheme will fail. It thus becomes crucial to verify experimentally the natural mode behavior of a layered structure.

Affirmation of the natural mode description of the frequency-domain response of a layered structure can be accomplished by comparing the extracted natural modes with those obtained from the theoretical IPM analysis in Chapter 3. To the extent that IPM involves implicitly the assumption of a pure natural mode description, close agreement between the two sets of modes would tend to substantiate the IPM reconstruction. This necessitates, however, the use of a layered structure which has been analyzed theoretically. The layered structure should also have clear boundaries and well-known properties, to make the mode extraction easier. Judging from these restricted criteria, we decided that the model should be made of thin Plexiglass layers.

A visually striking confirmation of the natural mode resonance is shown in Figure 7.4. This is the measured reflection waveform of a thin plexiglass layer of a thickness of 11.675 mm, placed perpendicular to the ultrasonic transducer. Note that the indicated early-time and late-time regions are reflections from the front and rear surfaces. It is obvious that this structure response is dominated by a single natural mode which is determined by the product of the double layer thickness (D) and the wave number ($k(\omega) = \beta(\omega) + j\alpha(\omega)$) of the specified plexiglass layer. Figure 7.5 shows a single mode best fit of the ratio of the rear and front responses from the SPA method.

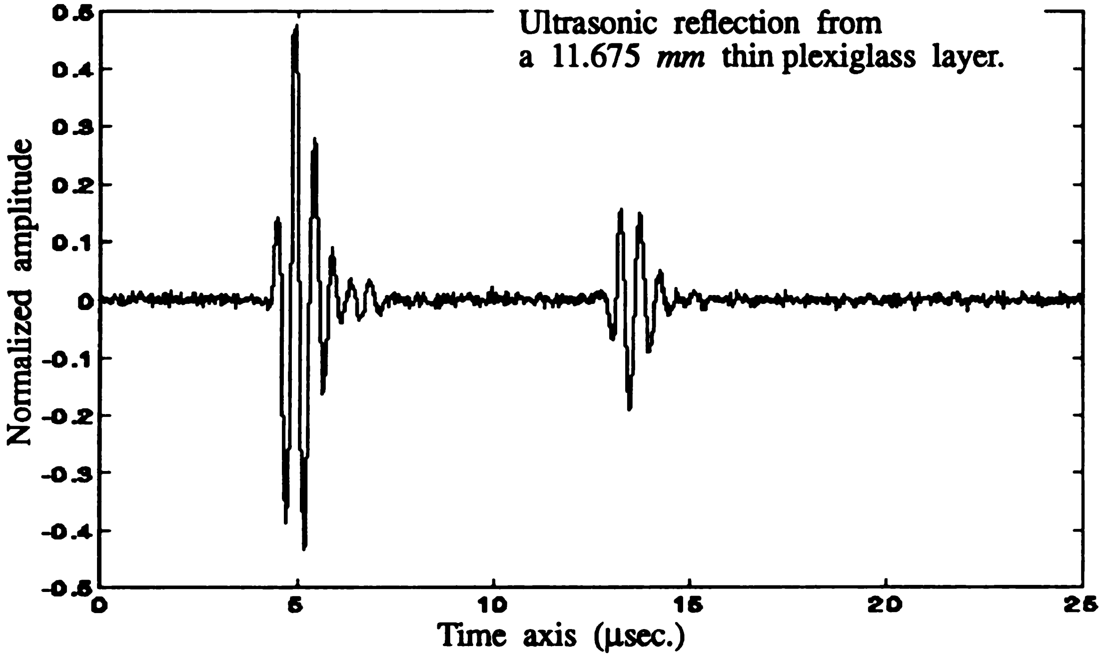

Figure 7.4: The measured reflection waveform of a 11.675 *mm* thin plexiglass layer placed perpendicular to the transducer axis.

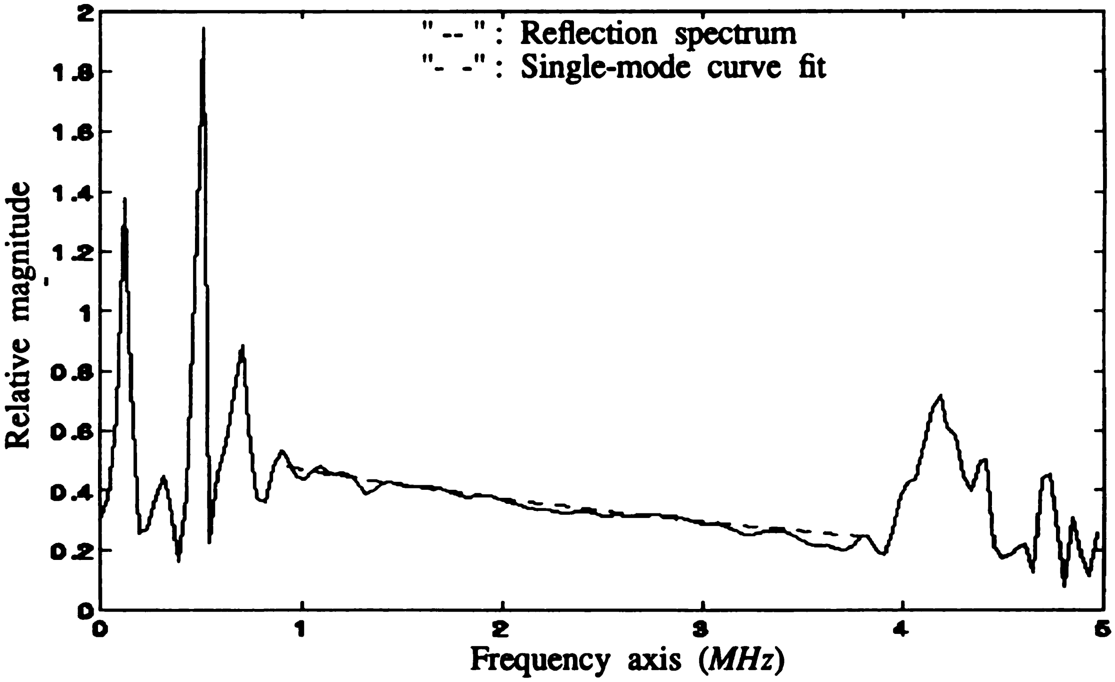

Figure 7.5: One-mode best fit to the spectral ratio of the rear and the front echoes, obtained from a 11.675 mm thin plexiglass layer.

Based on analysis in Chapter 5, the first natural mode of this layer should occur at $\sigma_1 + j\upsilon_1 = -.0376 + j8.522\ MHz^{-1}$. The single mode best fit from the SPA method ascribes a mode of $\sigma_1 + j\upsilon_1 = -.0358 + j8.478\ MHz^{-1}$. The agreement is extremely close.

By thinning the layer it is possible to lower the mode factors and thus to stimulate the existence of higher order modes caused by reverberation. Figure 7.6 shows the measured surface reflection waveform of a thin plate having a thickness of 1.475 *mm* placed perpendicular to the ultrasonic transducer. This reflection is apparently not dominated by any single mode. The question then becomes whether the reflection can be represented by a pure natural mode series. Figure 7.7 shows evidence for a positive answer. This figure displays the phase spectrum of the reflection waveform obtained via SPA. Three peaks very clearly dominate the spectrum and they can be used for initial guesses in the SPA method. Due to scattering and absorption effects, only the first three modes of this thin layer are absorbable.

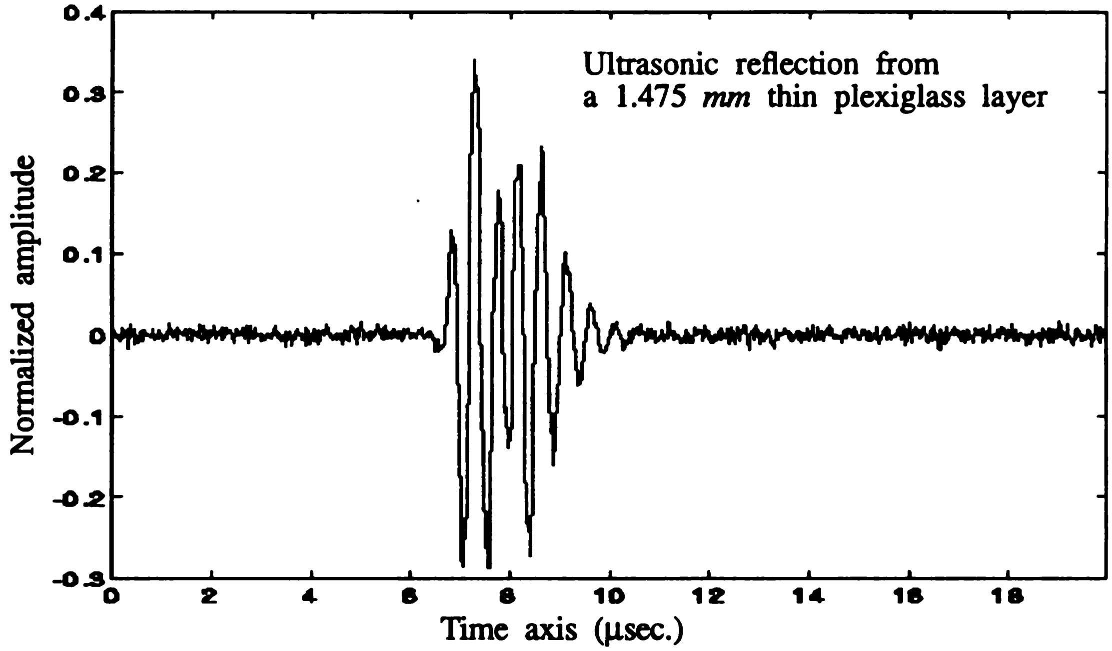

Figure 7.6 : Measured reflection waveform of a 1.475 *mm* thin plexiglass layer placed perpendicular to the transducer axis.

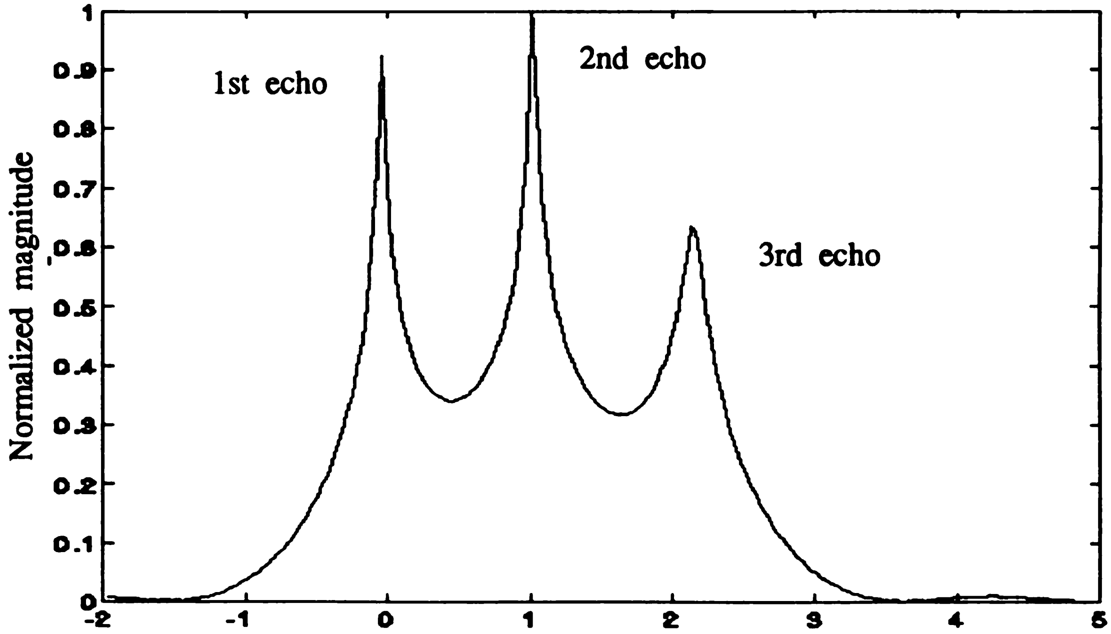

Figure 7.7 : Phase spectrum of the measured reflection waveform of a 1.475 mm thin plexiglas layer, obtained via SPA.

The theoretical and evaluated values of these natural modes are summarized in Table 7.1.

Table 7.1 : The reconstructed natural modes of a 1 .475 *mm* thin plexiglass layer, evaluated via the SPA method.

Natural modes	Theoretical value	Evaluated value	Evaluated amplitude
1st mode	0	.0041 + j0.0092	0.3872
2nd mode	-0.04 - j1.05	-.0213 - j1.0399	0.3451
3rd mode	-0.08 - j2.10	-.0743 - j2.1004	0.0631

The imaginary parts of the natural modes compare well with the theoretical values. However, the damping coefficients are not quite as close. We suspect that the discrepancies are due to the scattering and attenuation effects.

Confirmation of the IPM reconstruction can also be provided through reflected waveform measurements. For example, Figures 7.8a and 7.8b show the measured echo reflected by 5.365 *mm* and 4.645 *mm* thin plexiglass layers placed perpendicular to the transducer axis. It is obvious that the echo measurements are much noisier than that of 11.675 *mm* case. In fact, there is a noticeable amount of overlapping between the front and rear echo waveforms. Because of only two successive echoes, a single mode is excited.

Figures 7.8c and 7.8d show the single-mode best fit to the pass-band portion of the frequency response provided by the SPA method. These results for the thin plexiglass layers provide a great amount of confidence in the natural mode extraction from the reflection waveform of layered structures. If the reconstruction is indeed complete, then the material properties evaluated from the layer reflection waveforms should be independent of layer thickness. This has been shown to be true in the case of the thin plexiglass layers above.

A verification of the thickness independence of the material characteristics of this layered structure can be obtained by making measurements at different thicknesses, and evaluating the material characteristics from each reflection. Table 7.2 shows the experimental results. Material properties obtained from the experiment; such as velocity, attenuation coefficients, reflection coefficients, and acoustic impedance, are almost the same for four plexiglass layers with different thicknesses.

This completes the validation of natural modes reconstruction by using the IPM approach.

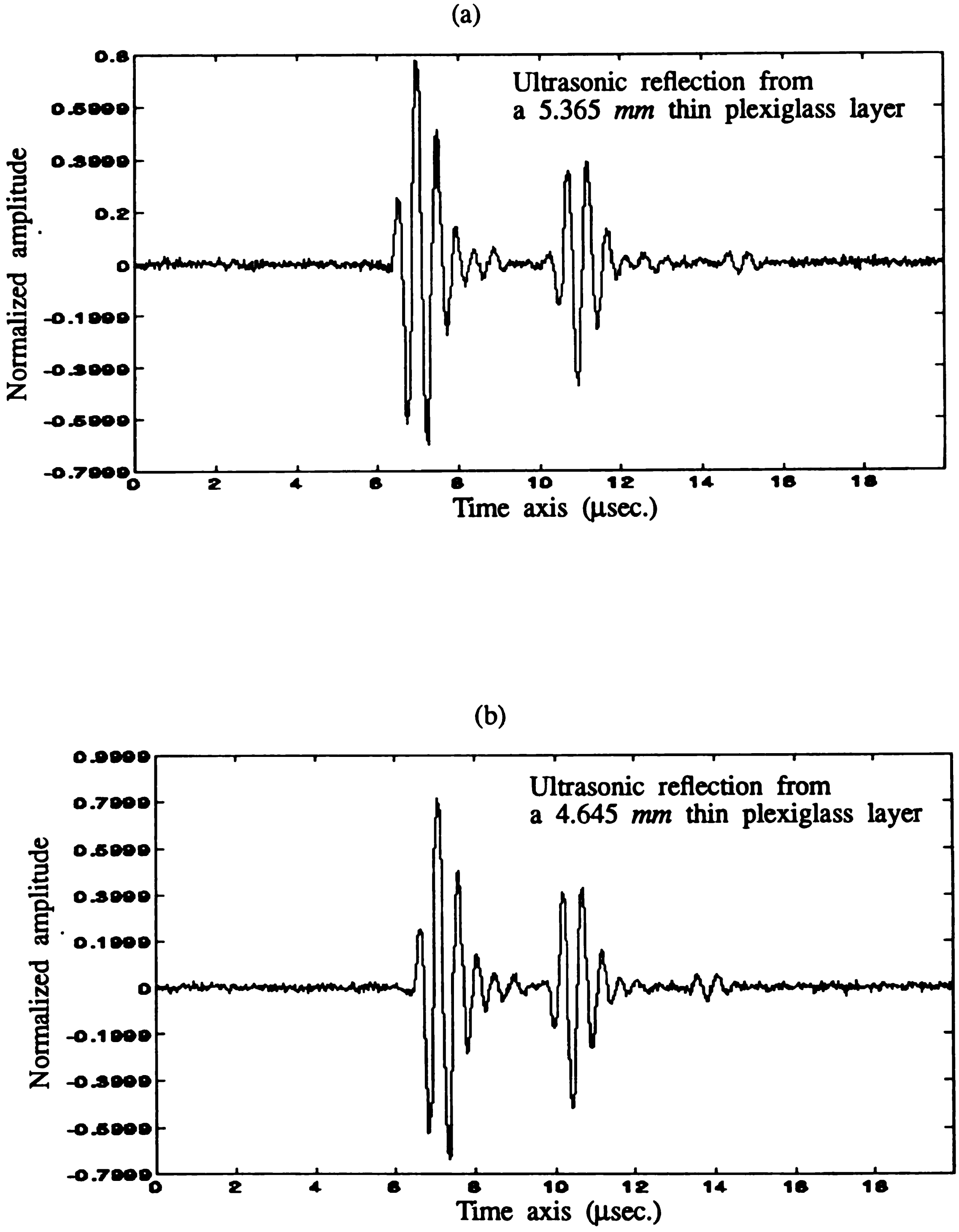

Figure 7.8 : The measured reflection waveform and single-mode best fit of plexiglass layers of different thicknesses : (a) & (c) are 5.365 *mm* and (b) & (d) are 4.645 *mm*. (to be cont'd)

Figure 7.8 (cont'd)

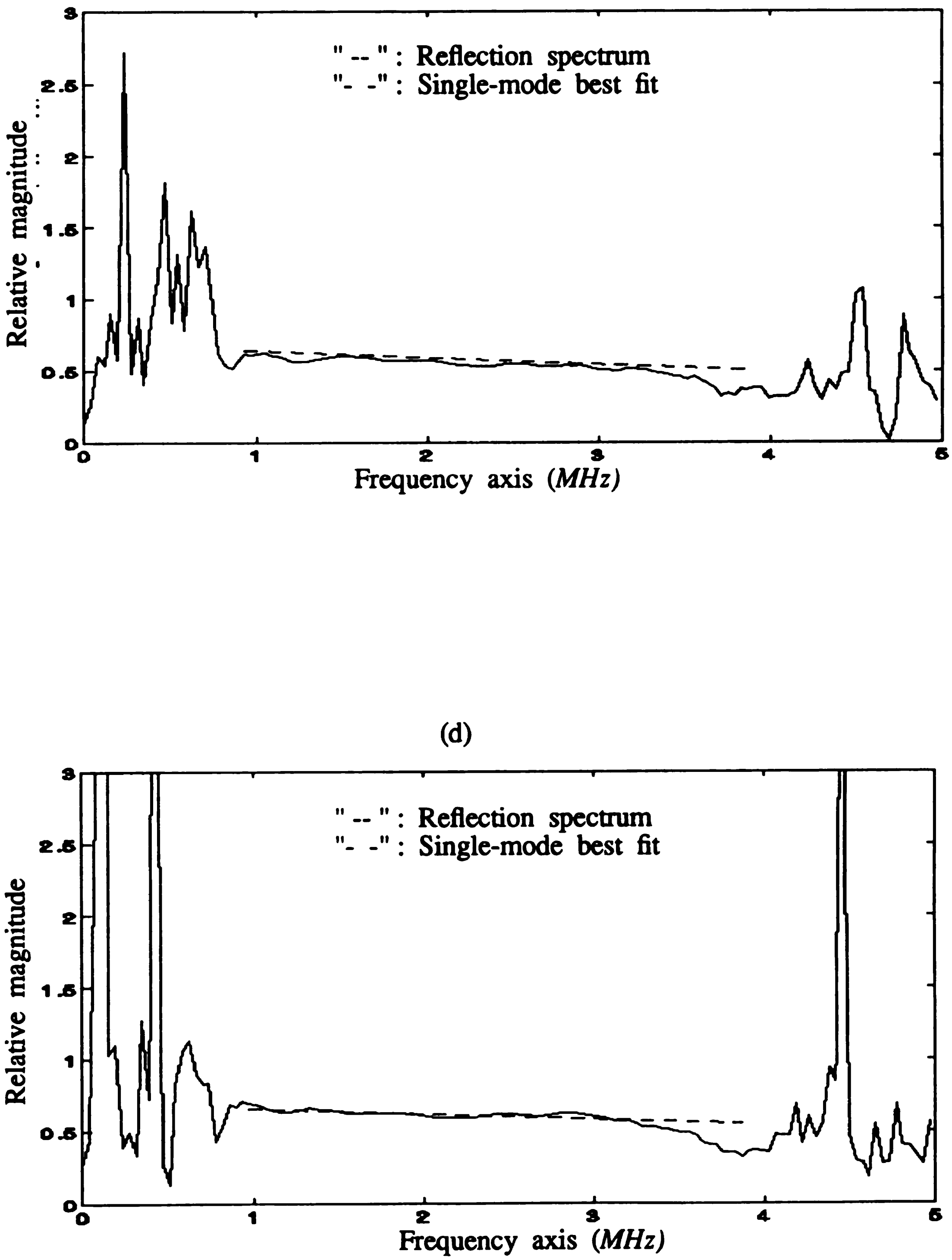

(c)

(d)

Table 7.2 : Acoustic properties of plexiglass layers reconstructed by the SPA method .

Thickness / Feature	11.675 *mm*	5.365 *mm*	4.645 *mm*	1.475 *mm*
Attenuation *(db/MHz-cm)*	.133±.004	.142±.056	.155±.034	.242±.018
Velocity *(m/sec)*	2751±2.57	2726±2.86	2742±3.31	2732±3.94
Reflection coeff .	.356	.312	.322	.291
Char. Impedence (kg/m^2-sec)	$3.162*10^6$	$3.563*10^6$	$3.512*10^6$	$3.632*10^6$

Note : 1). For the purpose of comparison, the attenuation is converted for a transducer having a center frequency of 2.25 *MHz* .

2). The experiments are performed at a temperature of 80 °F.

7.5 Experimental verification of the SPA Reconstruction

With the natural mode representation validated by the results of the previous section, the next step is to verify the reconstruction of the layered structure experimentally. Two different layered structures will be tested.

Figure 7.9a shows the reflected waveform of a solid plexiglass-aluminum structure. The geometry is shown in the same figure. Similarly, Figure 7.9b shows the reflected waveform of the plexiglass-copper structure. The Fourier spectrum of the plexiglas-aluminum response is shown in Figure 7.10a. Three distinct modes are observed in the phase spectrum, as shown in Figure 7.11a. A similar analysis reveals a total of three dominant modes for the plexiglass-copper structure, as shown in Figures 7.10b and 7.11b. The extracted natural modes $(\sigma_n+j\upsilon_n)$ corresponding to each structure have been evaluated by the SPA method, and are indicated in Figures 7.9a and 7.9b.

The experimental results suggest that as long as the echoes from the front and rear of the layer are not overlapping, the first order model is applicable. The transfer function of a given layer can be put strictly in terms of the properties of that layer, rather than the signature of the incident pulse and the characteristics of the measuring device. The transfer function of the n^{th} layer is

$$H_{n,n+1}(\omega) = \frac{U_i(\omega)\left[A_{n+1}e^{j\omega(\upsilon_{n+1}+j\sigma_{n+1})}\right]}{U_i(\omega)\left[A_n e^{j\omega(\upsilon_n+j\sigma_n)}\right]} = \frac{A_{n+1}}{A_n}e^{j\omega(\upsilon_{n,n+1}+j\sigma_{n,n+1})} \tag{7.1}$$

where $U_i(\omega)$ is the incident spectrum and $\upsilon_{n,n+1}+j\sigma_{n,n+1} = (\upsilon_{n+1}+j\sigma_{n+1}) - (\upsilon_n+j\sigma_n)$ is the natural mode of that layer.

For all cases, the SPA method is employed to evaluate material characteristics. The experimental results are summarized in Table 7.4. For the sake of comparison, published values [109, 110] of the material properties are listed in Table 7.3. It can readily be seen that the velocity, reflection coefficient, and characteristic impedance compare favorable with the published data [109, 110]. However, it is noticed that the attenuation constant deviates from the published value by a significant margin. This is possibly due to the scattering of the incident wave at the interfaces and the absorption of the transmitted wave propagating through the layer. Reviewing the results, we observe that

(1) The attenuation factors are approximately linear within the frequency band, $1.5\ MHz < f < 3.0\ MHz$.

(2) The measured velocity of various samples are very close to the published values, with a standard deviation of less than 1.2 % .

(3) The reflection coefficient varies over a wider range, since it is highly influenced by scattering, absorption, and attenuation.

In this chapter, we have tested the SPA algorithm based on natural modes with appropriate arrangement, and have shown that features can be simultaneously evaluated by utilizing a spectral sequence. Comparing the results with published data, this approach seems very promising. For example, the overall standard deviation of the estimated velocity is found to be within a 1.2% error band. The application of this method will be valuable for nondestructive evaluation of materials in industrial applications.

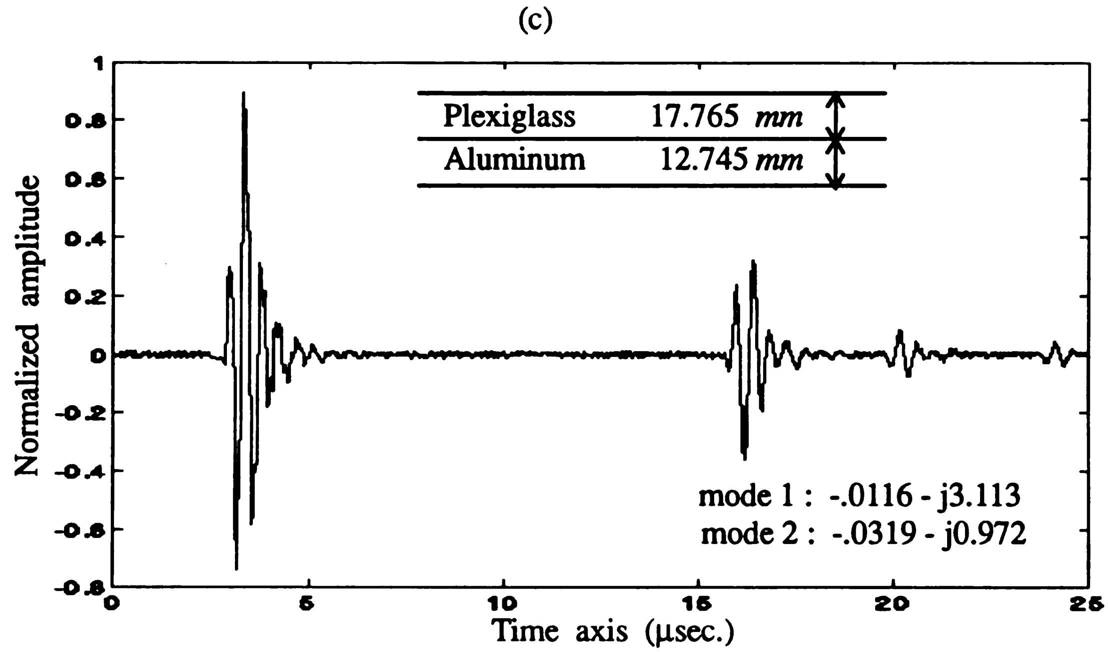

Figure 7.9a : Measured reflection waveform of a plexiglass-aluminum layered model placed perpendicular to the transducer axis.

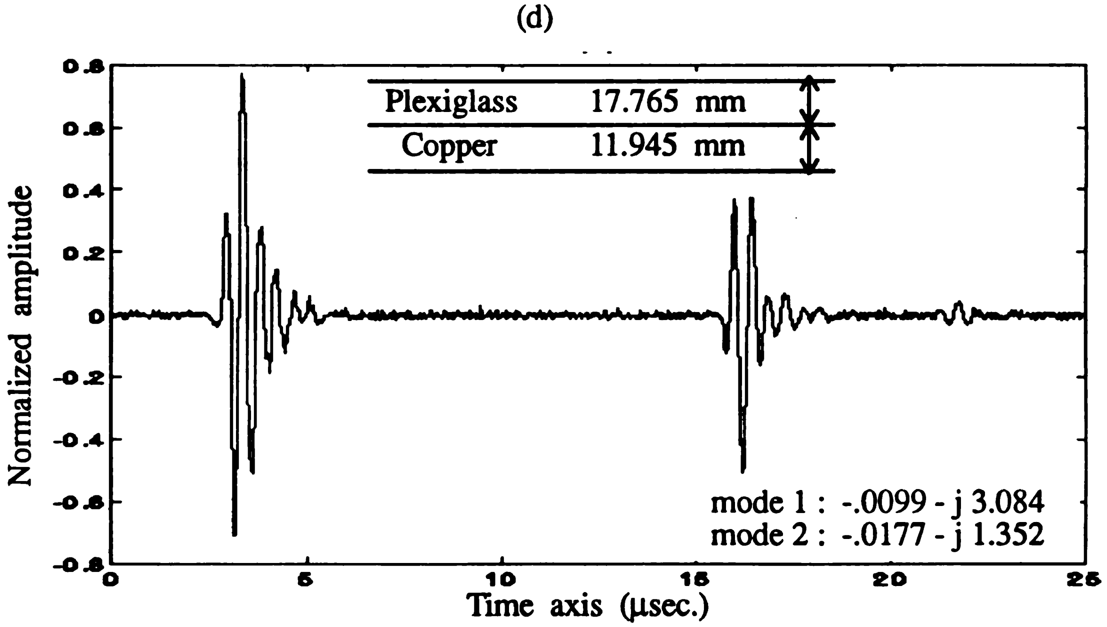

Figure 7.9b : Measured reflection waveform of a plexiglass-copper layered model placed perpendicular to the transducer axis.

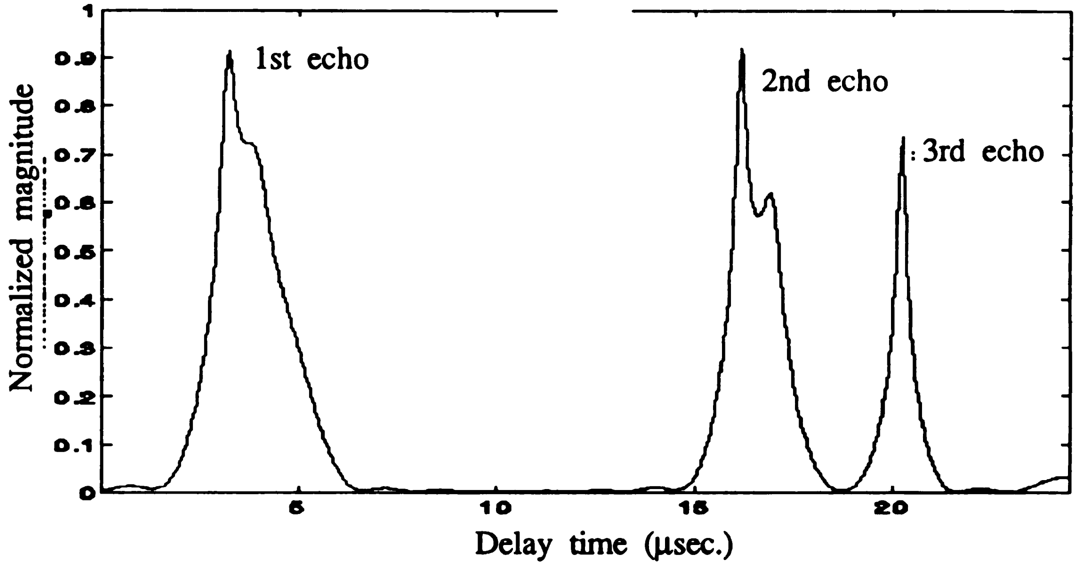

Figure 7.10a : Phase spectrum of the reflection waveform obtained from a plexiglass-aluminum model.

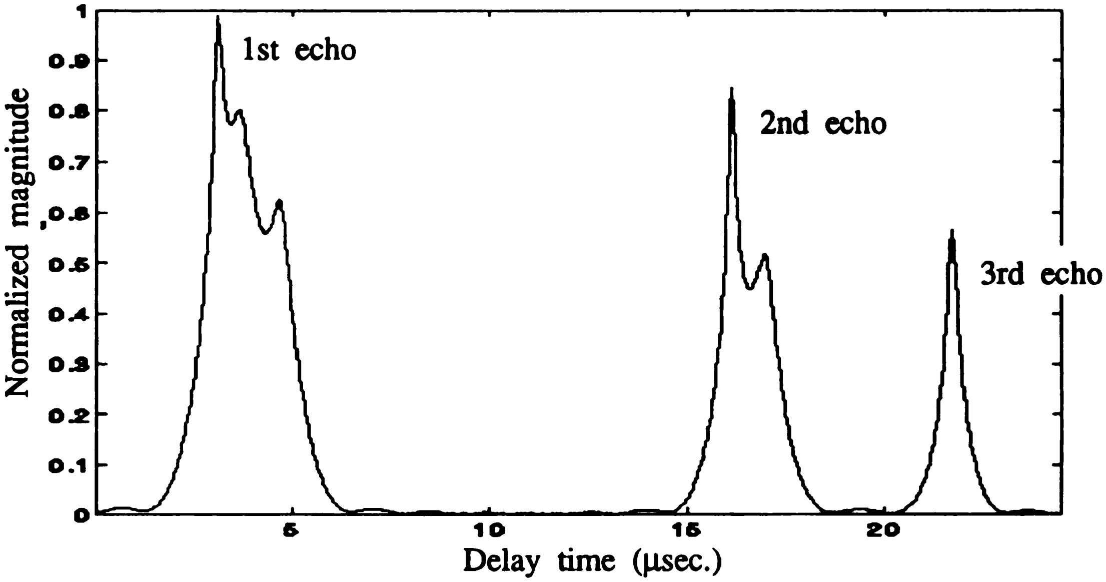

Figure 7.10b : Phase spectrum of the reflection waveform obtained from a plexiglass-copper model.

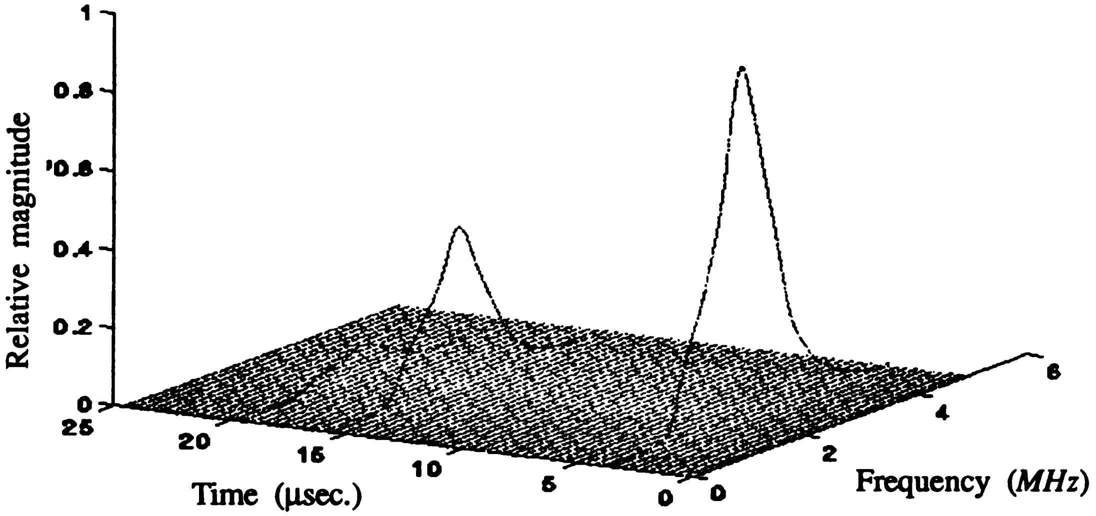

Figure 7.11a : Fourier spectrum of the reflection waveform obtained from a plexiglass-aluminum model.

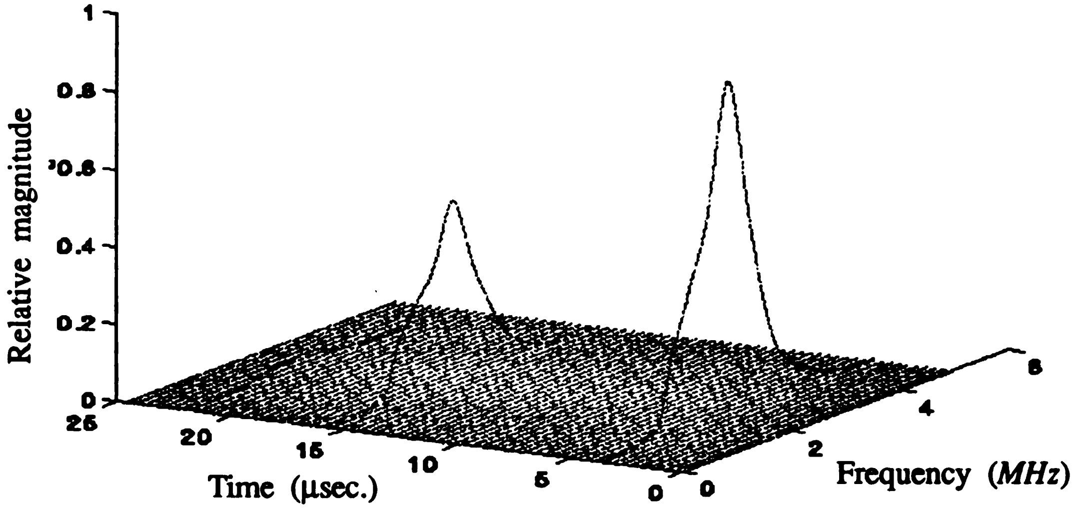

Figure 7.11b : Fourier spectrum of the reflection waveform obtained from a plexiglass-copper model.

Table 7.3 : The acoustical properties of different materials published by Kino [110].

Material / Feature	Aluminum (7075 -T6)	Plexiglass	Copper (70 - 30)
Attenuation *(db / MHz-cm)*	0.38	0.17	—
Velocity *(m / sec)*	6420	2740	4400
Density *(g / cm^3)*	2.71	1.15	8.64
Char. Impedence *(kg / m^2-sec)*	17.33×10^6	3.26×10^6	40.61×10^6

Table 7.4 : Acoustic properties of different materials evaluated by the SPA method.

Material / Feature	Aluminum (7075-T6)	Plexiglass	Copper (70 - 30)
Attenuation *(db / MHz-cm)*	0.443	0.136	0.255
Velocity *(m / sec)*	6425	2761	4338
Char. Impedence *(kg / m^2-sec)*	17.412×10^6	3.221×10^6	37.480×10^6

CHAPTER 8

CONCLUSION

The purpose of this research has been to investigate techniques of evaluating material properties by ultrasonic interrogation. This chapter reviews the state-of-the-art of ultrasonic identification as well as the techniques we have developed here in recent years. Finally, suggestions for future studies are given.

8.1 Summary

There are two major contributions from this thesis work: a proposed theoretical model for ultrasonic field reconstruction, and development of a scheme for layered structure identification.

In Chapter 2, an acoustic wave equation with the presence of scatterer was formulated. Wave solution using the Green's function technique was presented. To generalize the analysis, all distances were expressed in wavelengths and the medium functions were put in terms of the complex refractive index of the inhomogeneous medium. In such a way, the results could easily be adopted for solving other similar problems.

Two approximations, the Born and the Rytov, were used to linearize the wave equation. These two perturbational approximations are very useful since they allow simple inversion algorithms to be derived. Since these approximations play an important role in ultrasonic interrogation, the mathematical limitations of each approximation were reviewed and discussed.

The reconstruction theorem presented in Chapter 3 relates the scattered field measured on a location to the angular spectrum of the medium. This theorem is only true when either the Born or the Rytov approximation is valid. However, the imaging reconstruction research community has shown tremendous interest in this theorem.

The reconstruction theorem was derived by the use of IPM and WTM concepts in this work. Applying both to the reconstruction theorem leads to a simplified relationship between the reflected waveform and the natural modes of a layered structure. The conventional technique of extraction is to decompose the Green's function of the field reflected by a layered structure into plane waves, and then to substitute this result into the integral solution of the wave equation. The new technique of extraction is to consider the reconstruction theorem entirely in the frequency domain. This method results in improved computer implementation and was utilized in Chapter 4 for better estimations of material characteristics.

Other topics pertinent to the SPA technique were discussed as well. Five methods for extracting the natural modes of structures from their measured reflected waveform were presented. These methods were needed to provide the basis for SPA reconstruction routine, where conventional identification is usually unworkable. Only the SPA method was shown to be successful in the presence of random noise.

In addition, several signal processing concerns were examined in Chapter 5. By examining the standard deviation between the structure and the reconstruction, it was concluded that zero padding a waveform would be a way to reduce the interpolation error. On the other hand, using a Hamming window to shape the waveform could severely attenuate the high frequency information and introduces errors.

Chapter 6 present a theoretical analysis of field distribution around and inside an inhomogeneous and arbitrarily shaped target. The dyadic Green's function was used in the evaluation process, and a special arrangement to handle the singularity in the integral equation was also introduced. The results showed that a structure consisting of different materials could produce a local maximum in its field intensity distribution.

In Chapter 7, identification was also carried out using the measured reflected waveform of thin plexiglass plates with different thicknesses. The success of this experimental results provided an empirical verification of the SPA concept. Evaluation of material characteristics of several multi-layer structures were also successfully performed.

8.2 Suggestion for Future Studies

Some topics suggested in this work have not been fully explored, while other ideas have been generated during the course of this work. This section high-lights several of them.

In deriving the Born and the Rytov approximations, it was assumed that the scattered fields were small compared to the incident fields. This says that the structure must be weakly scattered for the ultrasonic identification to hold. If this condition is not met, then the reconstruction will have artifacts. This topic should be pursued further by looking into the limitations of physical dimensions and material properties. It is also possible to extend the analysis by using other approximations.

For better reconstruction, several steps of the SPA schemes could be modified. It is possible to include variable sampling size of the measured reflected response, as well as selection of the dimension of the signal space in SVD application. In the algorithm involving the construction of the PDF, the inclusion of some specified functions might be useful.

Lastly, the most interesting topic might perhaps be the most difficult one. There remains the question as to whether the refraction effect of the reflected field response can be utilized for ultrasonic identification purposes, despite its heavy dependence upon structural aspects. To pursue this topic, one should start out with a simple structure and measure the reflected field response in a 2-D region and see how well it compares with the theoretical prediction. To minimize the system error, it is preferable to exclude the receiving transducer response from the analysis. This requires the accurate positioning of the spatial response from the measured data. To this end, an efficient and accurate deconvolution scheme must be developed.

APPENDICES

APPENDIX A

ORIGINAL PRONY METHOD

If as many data samples are used as there are exponential parameters, then an exact exponential fit to the data may be made. Consider the N-exponential discrete-time function

$$u(l) = \sum_{n=1}^{N} h_n z_n^l \ , \qquad l = 0, 1, \cdots, L-1 \ . \tag{A.1}$$

Note that $u(l)$, rather than $\hat{u}(l)$, has been used because exactly $2N$ complex samples $u(0), \cdots, u(2N)$ are used to fit an exact exponential model to the $2N$ complex parameter $h_1, \cdots, h_N, z_1, \cdots, z_N$. The N equations of Eq. (A.1) for $0 \leq l \leq N-1$ may be expressed in matrix form as

$$\begin{bmatrix} z_1^0 & z_2^0 & \cdots & z_N^0 \\ z_1^1 & z_2^1 & \cdots & z_N^1 \\ \vdots & \vdots & & \vdots \\ z_1^{N-1} & z_2^{N-1} & \cdots & z_N^{N-1} \end{bmatrix} \begin{bmatrix} h_1 \\ h_2 \\ \vdots \\ h_N \end{bmatrix} = \begin{bmatrix} u(0) \\ u(2) \\ \vdots \\ u(N-1) \end{bmatrix} \ . \tag{A.2}$$

The matrix of indexed z elements has a Vandermonde structure. If a method can be found to determine separately the z elements, then Eq. (A.2) represents a set of linear simultaneous equations that can be solved for the unknown vector of complex amplitudes.

First, one could assume the polynomial $\phi(z)$, which has the z_k exponents as its roots, defined as

$$\phi(z) = \prod_{n=1}^{N}(z - z_n) \ . \tag{A.3}$$

Then the products of Eq. (A.3) are expanded into a power series and the polynomial may be represented as the summation

$$\phi(z) = \sum_{n=0}^{N} a_n z^{N-n} \ , \tag{A.4}$$

with complex coefficients $\{a_n \ , n = 0, 1, \cdots, N\}$ such that $a_0 = 1$. After that, one shifts the index on Eq. (A.1) from l to $l - m$ and multiplies it by the parameter a_m to yield

$$a_m u(l-m) = a_m \sum_{n=1}^{N} h_n z_n^{l-m} \ . \tag{A.5}$$

Forming similar products $a_0 u(l), \cdots, a_m u(l-m)$ and summing, it produces

$$\sum_{m=0}^{N} a_m u(l-m) = \sum_{n=1}^{N} h_n \sum_{m=0}^{N} a_m z_n^{l-m} \ , \tag{A.6}$$

which is valid for $N + 1 \leq l \leq 2N$. Substituting $z_n^{l-m} = z_n^{l-N} z_n^{N-m}$, Eq. (A.6) becomes

$$\sum_{m=0}^{N} a_m u(l-m) = \sum_{n=1}^{N} h_n z_n^{l-N} \sum_{m=0}^{N} a_m z_n^{N-m} = 0 \ . \tag{A.7}$$

The right-hand summation in Eq. (A.7) may be recognized as the polynomial defined by Eq. (A.4), evaluated at each of its roots z_n, yielding the zero result indicated. Eq. (A.7) is the linear difference equation whose homogeneous solution is given by Eq. (A.1). The polynomial (A.4) is the characteristic equation associated with this linear difference equation.

The N equations representing the valid values of a_m that satisfy Eq. (A.7) may be expressed as the $N \times N$ matrix equation

$$\begin{bmatrix} u(N-1) & u(N) & \cdots & u(0) \\ u(N) & u(N-1) & \cdots & u(1) \\ \cdot & \cdot & & \cdot \\ \cdot & \cdot & & \cdot \\ \cdot & \cdot & & \cdot \\ u(2N-2) & u(2N-3) & \cdots & u(N-1) \end{bmatrix} \begin{bmatrix} a_1 \\ a_2 \\ \cdot \\ \cdot \\ \cdot \\ a_N \end{bmatrix} = - \begin{bmatrix} u(N) \\ u(N+1) \\ \cdot \\ \cdot \\ \cdot \\ u(2N-1) \end{bmatrix} . \tag{A.8}$$

Eq. (A.8) demonstrates that, with $2N$ complex data samples, it is possible to decouple the h_n and z_n parameters. The complex polynomial coefficients $a_1, \cdots, a_N$, which are functions of only the time-dependent components z_n of the exponential model, form a linear predictive relationship among the time samples.

The Prony procedure to fit N exponentials to $2N$ data samples may now be summarized in three steps. First, the solution of Eq. (A.8) for the polynomial coefficients is obtained. Second, the roots of the polynomial defined by Eq. (A.4) are calculated. Finally, the damping σ_n and phase factor v_n may be determined from the roots z_n using the relationships

$$\sigma_n = \frac{\log|z_n|}{\Delta\omega} \quad MHz^{-1} \tag{A.9}$$

$$v_n = \frac{1}{\Delta\omega} \tan^{-1}\left[\frac{\mathrm{Im}(z_n)}{\mathrm{Re}(z_n)}\right] . \tag{A.10}$$

To complete the Prony procedure, the roots computed in the second step are used to construct the matrix elements of Eq. (A.2), which are solved for the N complex parameters $h_1, \cdots, h_N$. The amplitude A_n and initial phase θ_n may be determined from each h_n parameter with the relationships

$$A_n = |h_n| \tag{A.11}$$

$$\theta_n = \tan^{-1}\left[\frac{\mathrm{Im}(h_n)}{\mathrm{Re}(h_n)}\right] \quad \text{radians} . \tag{A.12}$$

APPENDIX B

DERIVATION OF THE DYADIC GREEN'S FUNCTION IN A SOURCE REGION

If the field point $\vec{r}$ is inside the source region, illuminated in Figure B.1, the integral Eq. (6.2) does not converge. In order to carry out the integration, a small volume surrounding the field point should be excluded. The evaluation of the integral will greatly depend on the shape of this excluded volume. Generally, we can express the displacement field at $\vec{r}$ as

$$\vec{u}(\vec{r}) = PV\int_V \vec{f}_{eq}(\vec{r}\,') \cdot \overleftrightarrow{G}(\vec{r}|\vec{r}\,')dV' + \vec{u}^{\,c}(\vec{r}) \tag{B.1}$$

where $\vec{u}^{\,c}(\vec{r})$ is a correction term which should be added to the integral to yield a correct value for the velocity field at $\vec{r}$. The correction term $\vec{u}^{\,c}(\vec{r})$ is produced by the stress density function $\vec{f}_{eq}(\vec{r})$ and the displacement density function $\eta(\vec{r})$ on the spherical surface of ΔV, which is a differential spherical volume with a radius ε as shown in Figure B.2.

To calculate the $\vec{u}^{\,c}(\vec{r})$, a coordinate system is chosen so that its origin coincides with that of the spatial coordinates and so that $\vec{f}_{eq}(\vec{r})$ is paralleled to the polar axis. Considering that $\vec{f}_{eq}(\vec{r})$ inside ΔV is uniform, we can then write

$$\vec{f}_{eq} = \hat{z}f_{eq} \ . \tag{B.2}$$

By using the continuity equation ($\nabla \cdot \vec{f}_{eq}(\vec{r}) = -\,\omega^2\rho_o\Phi(\vec{r})$), and defining $\eta(\vec{r})\Delta S = \lim_{\varepsilon\to 0}\int_{\Delta V}\Phi(\vec{r}\,')dV'$, one can express $\eta(\vec{r})$ as

$$\eta(\theta) = \frac{f_{eq}\cos\theta}{\omega^2\rho_o} \ . \tag{B.3}$$

The displacement field at the center of ΔV can be expressed in terms of a scalar potential field $\Phi(\vec{r})$ as $\vec{u}^{\,c}(\vec{r}) = -\nabla\Phi(\vec{r})$. If ΔV is small enough, the quasi-static approximation can be used to evaluated Φ as

$$\Phi(\vec{r}) = \frac{1}{\omega^2\rho_o}\int_{\Delta V}\nabla'\cdot\vec{f}_{eq}(\vec{r}\,')\,\frac{exp(-j\vec{k}_o\cdot\Delta\vec{r}\,')}{4\pi|\Delta\vec{r}\,'|}dV' \tag{B.4}$$

$$+\int_{\Delta S}\eta(\theta)\frac{exp(-j\vec{k}_o\cdot\Delta\vec{r}\,')}{4\pi|\Delta\vec{r}\,'|}ds'$$

where $\Delta\vec{r} = \vec{r} - \vec{r}\,'$ is the distance between the source point and the field point, and ΔS is the surface of ΔV. It is evident that the first term of Eq. (B.4) goes to zero as ΔV approaches zero. However, $\nabla\Phi$ can be shown to converge to a finite value as ΔV approaches zero. This implies that $\vec{u}^{\,c}(\vec{r})$ remains a finite value at the center of ΔV. For simplicity, we will evaluate the term $-\nabla\Phi$ for a spherical volume ΔV as follows

$$\vec{u}^{\,c}(\vec{r}) = \frac{-\hat{z}}{4\pi}\lim_{\varepsilon\to 0}\int_{\Delta S}\eta(\theta)\frac{(1+jk_o\varepsilon)}{\varepsilon^2}\,exp(-\,jk_o\varepsilon)\cos\theta\,ds' \ . \tag{B.5}$$

$$= \frac{-\hat{z}}{4\pi}\left[\frac{-f_{eq}}{\omega\rho_o}\right]\lim_{\varepsilon\to 0}\int_0^{2\pi}\int_0^{\pi}\frac{(1+jk_o\varepsilon)}{\varepsilon^2}\,exp(-\,jk_o\varepsilon)$$

$$\cdot\cos^2\theta\,\varepsilon^2\sin\theta\,d\theta\,d\phi = \frac{\vec{f}_{eq}(\vec{r})}{3\omega^2\rho_o} \ .$$

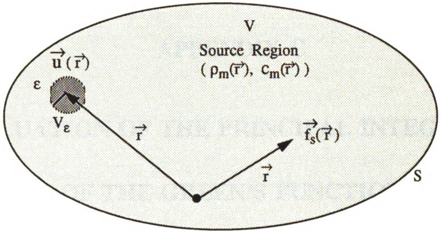

Figure B.1 : A general configuration of a source region problem.

$$\Delta V = \frac{4}{3}\pi a_n^3$$

a_n : Radius of sphere ΔV

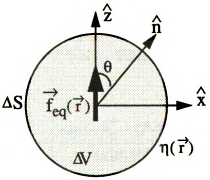

Figure B.2 : Evaluating the displacement density $\eta(\vec{r})$ by using a differential spherical volume ΔV.

APPENDIX C

EVALUATION OF THE PRINCIPAL INTEGRATION OF THE GREEN'S FUNCTION

Using a strategy similar to the one described in Appendix B, we modify V_n as a sphere with the same volume centered at $\vec{r}_n$, shown in Figure B.2. The radius of the sphere is denoted by

$$a_n = \left[\frac{3\Delta V_n}{4\pi}\right]^{1/3} . \tag{C.1}$$

Considering the property of equality : $\nabla'\Phi(\vec{r}|\vec{r}\,') = -\nabla\Phi(\vec{r}|\vec{r}\,')$, Eq. (6.7) can be rewritten as

$$G_{x_p x_q}(\vec{r}_n - \vec{r}\,') = \frac{1}{\omega^2\rho_o}\frac{\partial^2}{\partial x_q'\partial x_p'}\left[\frac{exp(-j\vec{k}_o \cdot (\vec{r} - \vec{r}\,'))}{4\pi|\vec{r} - \vec{r}\,'|}\right] , \tag{C.2}$$

$$p, q = 1, 2, 3 .$$

Therefore, we are allowed to treat the point $\vec{r} = \vec{r}_n$ as the new origin with the transformation of coordinates. Eq. (C.2) then becomes

$$G_{x_p x_q}(\vec{r}_n - \vec{r}\,') = G_{x_p x_q}(\vec{r}\,') = \frac{1}{\omega^2\rho_o}\frac{\partial^2}{\partial x_q'\partial x_p'}\left[\frac{exp(-j\vec{k}_o \cdot \vec{r}\,')}{4\pi|\vec{r}\,'|}\right] , \tag{C.3}$$

$$p, q = 1, 2, 3 .$$

In the spherical coordinates,

$$\frac{\partial^2}{\partial x_q{}'\partial x_p{}'}\left[\cdots\right] = \frac{x_p}{r}\frac{x_q}{r}\frac{d^2}{dr^2}\left[\cdots\right] + \left[\delta_{pq} - \frac{x_p}{r}\frac{x_q}{r}\right]\frac{1}{r}\frac{d}{dr}\left[\cdots\right] \ , \qquad \text{(C.4)}$$

$$p, q = 1, 2, 3 \ .$$

The principal value of the integration becomes

$$PV \int_{V_n} G_{x_p x_q}(\vec{r}_n|\vec{r}\,')dv' = \frac{1}{\omega^2\rho_o}\lim_{\varepsilon\to 0}\int_{\varepsilon}^{a_n} dr \int_0^{2\pi} d\phi \int_0^{\pi} \left\{ \frac{x_p x_q}{r^2} \right. \qquad \text{(C.5)}$$

$$\cdot \frac{d^2}{dr^2}\left[\frac{exp(-j\vec{k}_o\cdot\vec{r})}{4\pi r}\right] + \frac{1}{r}\left[\delta_{pq} - \frac{x_p x_q}{r^2}\right]$$

$$\left. \cdot \frac{d}{dr}\left[\frac{exp(-j\vec{k}_o\cdot\vec{r})}{4\pi r}\right]\right\} r^2 \sin\theta d\theta \ .$$

Carrying out the integration by parts, it becomes

$$PV \int_{V_n} G_{x_p x_q}(\vec{r}_n|\vec{r}\,')dv' = \frac{1}{\omega^2\rho_o}\lim_{\varepsilon\to 0}\left\{\left[r^2\frac{d}{dr}\left[\frac{exp(-j\vec{k}_o\cdot\vec{r})}{4\pi r}\right]\right]_{\varepsilon}^{a_n} \right. \qquad \text{(C.6)}$$

$$\cdot \int_0^{2\pi} d\phi \int_0^{\pi} \frac{x_p x_q}{r^2}\sin\theta d\theta$$

$$+ \int_0^{2\pi} d\phi \int_0^{\pi} \left[\delta_{pq} - 3\frac{x_p x_q}{r^2}\right]\sin\theta\, d\theta$$

$$\left. \cdot \int_{\varepsilon}^{a_n} \frac{d}{dr}\left[\frac{exp(-j\vec{k}_o\cdot\vec{r})}{4\pi r}\right] r\, dr \right\} \ .$$

Although the equation $\lim_{\varepsilon \to 0} \int_{\varepsilon}^{a_n} r \frac{d}{dr}\left[\frac{exp(-j\vec{k}_o \cdot \vec{r})}{4\pi r}\right] dr \to \infty$, it is readily verified that

$$\int_0^{2\pi} d\phi \int_0^{\pi} \left[\delta_{pq} - 3\frac{x_p x_q}{r^2}\right] \sin\theta d\theta = 0 \quad ; \quad p, q = 1, 2, 3 \ , \tag{C.7}$$

and

$$\int_0^{2\pi} d\phi \int_0^{\pi} \frac{x_p x_q}{r^2} \sin\theta d\theta = \frac{4\pi}{3}\delta_{pq} \quad ; \quad p, q = 1, 2, 3 \ . \tag{C.8}$$

Therefore, the Eq. (C.6) becomes

$$PV \int_{V_n} G_{x_p x_q} dV' = \frac{-\delta_{pq}}{\omega^2 \rho_o} \lim_{\varepsilon \to 0} \left\{ \frac{4\pi}{3} \left[r^2 \frac{d}{dr} \left[\frac{exp(-j\vec{k}_o \cdot \vec{r})}{4\pi r} \right] \right]_{\varepsilon}^{a_n} \right\} \tag{C.9}$$

$$\leq \frac{-\delta_{pq}}{3\omega^2 \rho_o} \left[(1 + jk_o a_n) exp(-jk_o a_n) - 1 \right]$$

where $\vec{k}_o \cdot \vec{r} \Big|_{r = a_n} \leq k_o a_n$.

BIBLIOGRAPHY

BIBLIOGRAPHY

[1] C. Gazanhes, J. P. Herault, and K. Stephankis, "Reflection coefficient identification by means of correlation: Applications to layered medium," *J. Acoust. Soc. Amer.*, vol. 69, No. 3, pp. 720-727, Mar. 1981.

[2] M. Cookey, H. J. Trussel, and T. J. Won, "Seismic deconvolution by multi-pulse methods," *IEEE Trans. A.S.S.P.*, vol. 38, No. 1, pp. 156-160, Jan. 1990.

[3] M. Fink, F. Hottier, and J. F. Cardoso, " Ultrasonic signal processing for *in vivo* attenuation measurement : short-time Fourier analysis," *Ultrasonic Imaging*, vol. 5, pp. 117-135, Apr. 1983.

[4] R. Kuc, "Estimating acoustic attenuation from reflected ultrasound signals : Comparison of spectral-shift and spectral-difference approaches," *IEEE Trans. A.S.S.P.*, vol. ASSP-32, No. 1, pp. 1-6, Feb. 1984.

[5] W. Sachse and Y. H. Pao, "On determination of phase and group velocity of dispersive wave in solids," *J. Appl. Phys.*, vol. 49, pp. 4320-4327, Dec. 1978.

[6] T. Pialucha, C. C. H. Guyott, and P. Cawley, "Amplitude spectrum method for the measurement of phase velocity," *Ultrasonic*, vol. 27, pp. 270-279, Sep. 1989.

[7] R. Kumaresan and D. W. Tufts, "Estimation of frequencies of multiple sinusoids making linear predication perform like maximum likelihood," *Proc. IEEE*, vol. 70, No. 9, pp. 975-989, Sep. 1982.

[8] S. W. Ross, "Review and examination of results on uniqueness in inverse problems," *Int. Symp. on Electromagnetic Theory*, , pp. 1026-1030, Aug. 1986.

[9] W. R. Smith, "Mathematical analysis, an inverse problem arising in convective-diffusive flow," *J. Appl. Math.*, vol. 45, No. 3, pp. 225-231, Mar. 1990.

[10] Y. M. Ram and S. G. Braun, "Inverse problem associated with modification of incomplete dynamic systems," *Trans. on ASME*, vol. 58, No. 1, pp. 233-237, Mar. 1991.

[11] J. A. Fawcett, "Inversion of acoustic plane wave reflection coefficients for bottom elastic parameters," *Wave Motion*, vol. 12, No. 5, pp. 451-460, Sep. 1990.

[12] C. A. Balanis, *Advanced engineering electromagnetics*, New York: John Wiley & Sons, 1989.

[13] R. A. Lemons and C. F. Quate, "Acoustic microscopy," chap. 1 in *Physical acoustics: principles and methods*, vol. XIV, pp. 1-92, W. P. Mason and R. N. Thurston, eds., New York: Academic Press, 1979.

[14] R. N. Bracewell, *The Fourier transform and its applications*, 2nd ed., New York: McGraw-Hill, 1978.

[15] W. M. Ewing, W. S. Jardetsky, and F. Press, *Elastic waves in layered media*, New York: McGraw-Hill, 1957.

[16] A. Ishimaru, *Wave propagation and scattering in random media*, New York: Academic Press, 1978.

[17] A. C. Kak, "Tomographic imaging with diffracting and non-diffracting sources," in *Array signal processing*, S. Haykin, ed., Englewood Cliffs, NJ: Prentice Hall, 1984.

[18] P. M. Morse and H. Fesfbach, *Methods of theoretical physics*, New York: McGraw-Hill, 1966.

[19] K. Iwata and R. Nagata, "Calculation of refractive index distribution from interferograms using the Born and Rytov's approximations," *Jap. J. Appl. Phys.*, vol. 14, pp. 1921-1927, 1975.

[20] R. McGowan and R. Kuc, "A direct relation between a signal time series and its unwrapped phase," *IEEE Trans. on A.S.S.P.*, vol. ASSP-30, pp. 719-726, Oct. 1982.

[21] H. Hochstadt, *Integral equations*, New York: John Wiley & Sons, Inc., 1973.

[22] D. Colton and R. Krees, *Integral equation method in scattering theory*, New York: John Wiley & Sons, 1983.

[23] C. A. Balanis, *Antenna theory: analysis and design*, New York: John Wiley & Sons, 1973.

[24] R. G. Newton, *Scattering theory of waves and particles*, New York: McGraw-Hill, 1966.

[25] M. Kareh, M. Soumekh and J. F. Greenleaf, "Signal processing for diffraction tomography," *IEEE Trans. on Sonics and ultrasonics*, vol. SU-31, pp. 230-238, July 1984.

[26] E. M. Kennaugh and D. L. Moffat, "Transient and impulse response approximations," *Proc. IEEE*, pp. 893-901, Aug. 1965.

[27] L. Marin, "Representation of transient scattered fields in terms of free oscillations of bodies," *Proc. IEEE*, pp. 640-641, May 1972.

[28] E. Mese, et. al., "Target identification by mean of Radar," *Microwave Journal*, pp. 85-102, Dec. 1984.

[29] P. H. Johnston and E. I. Madaras, "Modeling the pulse-echo response of a two-dimensional phase-insensitivity array for NDE of layered media," in *Proc. IEEE Ultrason. Symp.*, Chicago, IL, pp 1021-1025, 1988.

[30] T. J. Cavicchi, S. A. Johnson, and W. D. O'Brien, "Application of the sinc basis moment method to the reconstruction of infinite circular cylinders," *IEEE Trans. on U.F.F.C.*, vol. 35, no. 1, pp. 22-33, Jan. 1988.

[31] C. Gazanhes, J. P. Herault, and K. Stephanakis, "Reflection coefficients identification by mean of correlation: application to layered medium," *J. Acoust. Soc. Amer.*, vol. 69, no. 3, pp. 720-727, Mar. 1981.

[32] Y. Lu, J. D. Achenbach, "Effects of random deviations in interface properties on the propagation of ultrasound in thick composites," *J. Acoust. Soc. Amer.*, vol. 90, no. 5, pp. 2576-2585, Nov. 1991.

[33] M. Cookey, H. J. Trussell, and I. J. Won, "Seismic deconvolution by multiple methods," *IEEE Trans. on A.S.S.P.*, vol. 38, no. 1, pp. 156-160, Jan. 1990.

[34] R. Yarlagadda, J. B. Bednar, and T. L. Watt, "Fast algorithms for L_p deconvolution," *IEEE Trans. on A.S.S.P.*, vol. 33, no. 1, pp. 174-181, Jan. 1985.

[35] S. A. Goss, R. L. Johnson, and F. Dunn, "Comprehensive compilation of empirical ultrasonic properties of mammalian tissue," *J. Acoust. Soc. Amer.*, vol. 64, no. 2, pp. 423-457, Feb. 1978.

[36] R. Kuc, "Clinical application of an ultrasound attenuation coefficient estimation technique for liver pathology characterization," *IEEE Trans. on Biomed. Eng.*, vol. BME-27, pp 312-319, June 1980.

[37] K. Sobezyk, *Stochastic wave propagation*, Warsaw, Poland: Elsevier, 1985.

[38] K. Aki and P. Richards, *Quantitative seismology: theory and methods*, San Francisco: W. H. Freeman, 1980.

[39] F. R. DiNapoli and R. L. Deavenport, "Theoretical and numerical Green's function field solution in a plane multilayered medium," *J. Acoust. Soc. Amer.*, vol. 67, no. 1, pp. 92-105, Jan. 1980.

[40] J. W. Goodman, *Introduction to Fourier optics*, 3rd ed., San Francisco: McGraw-Hill, 1968.

[41] T. K. Sarkar, D. D. Weiner, and V. K. Jain, "Some mathematical considerations in dealing with the inverse problems," *IEEE Trans. on Antennas Propagat.*, vol.

AP-19, pp. 373-379, Mar. 1981.

[42] Y. Das and W. M. Boerner, "On Radar target shape estimation using algorithms for reconstruction from projections," *IEEE Trans. on Antennas Propagat.*, vol. AP-26, pp. 274-279, Mar 1978.

[43] H. J. Schmitt, et al., "Calculated and experimental response of thin cylindrical antennas to pulse excitation," *IEEE Trans. on Antennas Propagat.*, vol. AP-14, pp. 120-127, Mar 1966.

[44] C. L. Bennett, "Transient scattering from conducting cylinders," *IEEE Trans. on Antennas Propagat.*, vol. AP-18, pp. 627-633, Sep. 1970.

[45] L. B. Felsen, "Comments on early time SEM," *IEEE Trans. on Antennas Propagat.*, vol. AP-33, pp. 118-119, Jan. 1985.

[46] D. G. Dudley, "Comments on SEM and parametric inverse problem," *IEEE Trans. on Antennas Propagat.*, vol. AP-33, pp. 119-120, Jan. 1985.

[47] M. A. Morgan, "Response to comments regarding SEM representations," *IEEE Trans. on Antennas Propagat.*, vol. AP-33, pp. 120, Jan. 1985.

[48] K. M. Chen and D. Westmoreland, "Impulse response of a conducting cylinder based on SEM," *Proc. IEEE*, vol. 69, pp. 747-750, Jan. 1981.

[49] K. M. Chen, "Radar waveform synthesis for single-mode scattering by a thin cylinder and application for target discrimination," *IEEE Trans. on Antennas Propagat.*, vol. AP-30, pp. 867-880, Sep. 1982.

[50] R. Kuc, *Introduction to digital signal processing*, New York: McGraw-Hill, 1988.

[51] H. P. Bucker, "Comparison of FFT and Prony algorithm for bearing estimation of narrow-band signals in realistic ocean environment," *J. Acoust. Soc. Amer.*, vol. 61, pp. 756-762, Mar. 1977.

[52] M. A. Rahmanand and K. B. Yu, "Improved frequency estimation using total least square approach," in *Proc. IEEE Int. Conf.*, Tokyo, Japan, pp. 1392-1400,

Apr. 1986.

[53] M. P. Hurst and R. Mittra, "Scattering center analysis via Prony's method," *IEEE Trans. on Antennas Propagat.*, vol. AP-35, pp. 986-988, Aug. 1987.

[54] R. Carriére and R. L. Moses, "High resolution Radar target modeling using a modified Prony estimator," *IEEE Trans. on Antennas Propagat.*, vol. AP-40, no. 1, pp. 13-18, Jan. 1992.

[55] R. Kumaresan and D. W. Tufts, "Estimating the parameters of exponential damped sinusoids and pole-zero modeling in noise," *IEEE Trans. on A.S.S.P.*, vol. ASSP-30, pp. 833-840, Dec. 1982.

[56] I. Ziskind and M. Wax, "Maximum likelihood localization of multiple source by alternating projection," *IEEE Trans. on A.S.S.P.*, vol. ASSP-36, no. 10, pp. 1553-1560, Oct. 1988.

[57] H. Yamada, M. Ohmiya, Y. Ogawa, and I. Itoh, "Superresoultion techniques for time-domain measurements with a network analyzer," *IEEE Trans. on A.S.S.P.*, vol. ASSP-39, no. 2, pp. 177-183, Feb. 1991.

[58] Y. Hua and T. K. Sarkar, "Matrix pencil method for estimating parameter of exponentially damped/undamped sinusoids in noise," *IEEE Trans. on A.S.S.P.*, vol. ASSP-38, no. 5, pp. 814-824, May 1990.

[59] Z. A. Marićević, T. K. Sarkar, Y. Hua, and A. R. Djordjević, "Time-domain measurements with the Hewlett-Packard network analyzer - HP 8510 using the matrix pencil method," *Microwave Theory and Technique*, vol. 39, no. 3, pp. 538-547, May 1991.

[60] de Prony, Baron (Gaspard Riche), "Essai expérimental et analytique, etc.," *Paris J. of L'Ecole Polytech.*, Vol. 1, No. 2, pp. 24-76, 1795.

[61] S. L. Marple, Jr., "Spectral line analysis by Pisarenko and Prony methods," in *Proc. of 1979 IEEE Int. Conf.*, Washington, DC, pp. 155-161, 1979.

[62] R. N. McDonough and W. H. Haggins, "Best least square representation of signals by exponentials," *IEEE Trans. on Autom. Control*, vol. AC-13, pp. 408-412, Aug. 1968.

[63] S. L. Marple, Jr., *Digital spectral analysis with application*, Englewood Cliffs, NJ: Prentice-Hall, 1987.

[64] T. J. Shan, M. Wax, and T. Kailath, "On spatial smoothing for direction-of-arrival estimation of coherent signals," *IEEE Trans. on A.S.S.P.*, vol. ASSP-33, no. 4, pp. 806-811, Apr. 1985.

[65] D. W. Tufts and R. Kumaresan, "Estimation of frequencies of multiple sinusoids making linear prediction perform like maximum likelihood," in *Proc. of 1982 IEEE Int. Conf.*, vol. ASSP-70, no. 9, pp. 975-989, Sep. 1982.

[66] W. F. Gabriel, "Using spectral estimation techniques in adaptive processing antenna systems," *NRL-REP. 8920 Naval Res. Lab.*, Washington D.C., Oct. 1985.

[67] R. O. Schmidt, "Multiple emitter location and signal parameters estimation," *IEEE Trans. on Antennas Propagat.*, vol. AP-34, pp. 276-280, Mar. 1986.

[68] D. W. Tufts and R. Kumeresan, "Improve spectral resolution," in *Proc. of IEEE*, vol. 68, no. 3, pp. 419-420, Mar. 1980.

[69] W. H. Press, et. al., *Numerical recipes, the art of scientific computing*, New York: Cambridge University Press., 1986.

[70] R. K. Otnes and L. Enochson, *Applied time series analysis*, New York: John Wiley & Sons, 1978.

[71] M. Zoltowski and F. Haber, "A vector space approach to direction finding in a coherent multi-path environment," *IEEE Trans. on Antennas Propagat.*, vol. AP-34, pp. 1069-1079, Sep. 1986.

[72] R. T. Williams, S. Prasad, A. K. Mahaland, and L. H. Sibyl, "An improved spatial smoothing technique for bearing estimation in a multi-path environment,"

IEEE Trans. on A.S.S.P., vol. 36, pp.425-432, Apr. 1988.

[73] G. E. Forsythe, M. A. Malcolm, and C. B. Molar, *Computer methods for mathematical computations*, Englewood Cliffs, NJ: Prentice-Hall, 1977.

[74] A. W. Bojanczyk, M. Ewerbring, F. T. Luk, and P. V. Dooren, "An accurate product SVD algorithm," in *SVD and Signal Processing II: algorithms, analysis and applications*, R. Vaccaro, ed., Amsterdam: Elsevier Science Publisher, 1991.

[75] R. Kumaresan and D. W. Tufts, "Singular value decomposition and spectral analysis," *Proc. IEEE*, pp. 6.4.1-6.4.12, Aug. 1981.

[76] C. Lanczos, *Applied numerical analysis*, Englewood Cliffs, NJ: Prentice-Hall, 1956.

[77] V. C. Klema and A. T. Lamb, "The singular value decomposition : its computation and some applications," *IEEE Trans. Autom. Control*, AC-25, pp. 164-176, Apr. 1980.

[78] C. Y. King and B. Ho, "Simultaneous measurement of material characteristics of layered structures by a single acoustic interrogation," *IEEE Trans. on Instrument and Measurement*, Oct. 1993. (forthcoming)

[79] S. Haykin, ED., *Advances in spectrum analysis and array processing, Vol. I and II*, Englewood Cliffs, NJ: Prentice-Hall, 1991.

[80] R. Gagliard, *Introduction to communication engineering*, New York: John Wiley & Sons, 1978

[81] P. P. Lele and K. J. Parker, "Temperature distributions in tissues during local hyperthermia by stationary or steered beams of unfocussed or focussed ultrasound," *Brit. J. Cancer Suppl.* , vol. 45, pp. 108-121, 1982.

[82] AIUM (The American Institute of Ultrasound in Medicine), "Bio-effects considerations for the safety of diagnostic ultrasound," *J. Ultrasound Med.*, vol. 7, no. 9, pp. 1-38, 1988.

[83] W. L. Lin, R. B. Roemer, and K. Hynynen, "Theoretical and experimental evaluation of a temperature controller for scanned focussed ultrasound hyperthermia," *Med. Phys*, vol. 17, pp. 615-625, 1990.

[84] B. A. Auld, *Acoustic field and waves in solids: Vol. II*, New York: John Wiley & Sons, 1973.

[85] G. Beylkin and R. Burridge, "Linearized inverse scattering problems in acoustic and elasticity," *Wave Motion*, vol. 12, pp. 15-52, 1990.

[86] L. M. Brekhovskikh, *Waves in layered media*, translated by R. T. Beyer, New York: Academic press, 1980.

[87] D. E. Bray and R. K. Stanley, *Nondestructive evaluation: A tool for design, manufacturing, and service*, New York: McGraw-Hill, 1989.

[88] R. C. Waag, J. P. Astheimer, and G. W. Swartout, "A characterization of wavefront distortion for analysis of ultrasound diffraction measurement made through an inhomogeneous medium," *IEEE Trans. on Sonic & Ultrason.*, vol. 32, no. 1, pp. 30-48, Jan. 1985.

[89] S. M. Rao and B. S. Sridhara, "Acoustic scattering from arbitrarily shaped multiple bodies in half space: method of moment solution," *J. Acoust. Soc. Amer.*, vol. 91, no. 2, pp. 652-657, Feb. 1992.

[90] Y. L. Li, C. H. Liu, and S. J. Franke, "Three dimensional Green's function for wave propagation in a linearly inhomogeneous medium - the exact analytic solution," *J. Acoust. Soc. Amer.*, vol. 87, no. 6, pp. 2285-2291, June, 1990.

[91] E. A. Kraut, "Review of theories of scattering of elastic waves by cracks," *IEEE Trans. Sonics & Ultrason.*, vol. 23, no. 3, pp. 162-167, May 1976.

[92] J. E. Gubernatis, E. Domany, J. A. Krumhansi, and M. Huberman, "Formal aspects of the theory of the scattering of ultrasound by flaws in elastic material," *J. Appl. Phys.*, vol. 48, no. 7, pp. 2804-2811, 1977.

[93] J. E. Gubernatis, E. Domany, J. A. Krumhansi, and M. Huberman, "The Born approximation in the theory of the scattering of elastic waves by flaws," *J. Appl. Phys.*, vol. 48, no. 7, pp. 2812-2819, 1977.

[94] J. U. Tribolet, *Seismic application of homomorphic signal processing*, Englewood Cliffs, NJ: Prentice Hall, 1979.

[95] G. S. Kino, *Acoustic waves: devices, imaging and analog signal processing*, Englewood Cliffs, NJ: Prentice Hall, 1987.

[96] M. Bouchon, "Calculation of complete seismograms for an explosive source in a layered medium," *Geophys.*, vol. 45, no. 2, pp. 197-203, Feb. 1980.

[97] E. J. Aymé-Bellegarda and T. M. Habashy, "Forward ultrasonic scattering from multidimensional solid or fluid inclusions buried in multilayered elastic structures," *IEEE Trans. on U.F.F.C.*, vol. 39, no. 1, pp. 1-10, Jan. 1992.

[98] E. J. Aymé-Bellegarda and T. M. Habashy, "Ultrasonic inverse scattering multidimensional object buried in multilayered elastic background structures," *IEEE Trans. on U.F.F.C.*, vol. 39, no. 1, pp. 11-18, Jan. 1992.

[99] E. J. Aymé-Bellegarda and T. M. Habashy, "Ultrasonic inverse scattering of 2-D objects buried in multilayered elastic background structures," *Proc. IEEE 1990 Ultrason. Symp.*, pp. 845-848, Dec. 1990.

[100] C. Y. King and B. Ho, "The ultrasonic field within an inhomogeneous and arbitrarily shaped scatterer," *IEEE Trans. on U.F.F.C.*, (under review)

[101] B. A. Auld, *Acoustic field and waves in solids: vol. I*, New York: John Wiley & Sons, 1973.

[102] D. Ensminger, *Ultrasonics - fundamentals, technology, and applications*, New York: Marcel Dekker, 1988.

[103] E. J. Aymé-Bellegarda and T. M. Habashy, "Constrained least-squares reconstruction of multidimensional objects buried in inhomogeneous elastic media," in

Proc. IEEE 1991 Int. Conf. A.S.S.P., pp. 2502-2508, May 1991.

[104] S. M. Rao and B. S. Sridhara, "Application of the method of moments to acoustic scattering from arbitrarily shaped rigid models coated with lossless, shear-less materials of arbitrary thickness," *J. Acoust. Soc. Amer.*, vol. 90, no. 3, pp. 1601-1608, Mar. 1990.

[105] Edited by R. Vaccaro, *SVD and signal processing, II: algorithm, analysis and applications*, Amsterdam: Elsevier Science publisher, 1991.

[106] S. A. Goss, R. L. Johnson, and F. Dunn, "Compilation of empirical ultrasonic properties of mammalian tissues, II," *J. Acoust. Soc. Amer.*, vol. 68, pp. 93-108, 1980.

[107] X. B. Fan and K. Hynynen, "The effect of wave reflection and refraction at soft tissue interfaces during ultrasound hyperthermia treatments," *J. Acoust. Soc. Amer.*, vol. 91, no. 3, pp. 1727-1736, Mar. 1992.

[108] T. W. Parks and C. S. Burrus, *Digital filter design*, New York: John Wiley & Sons, 1981.

[109] D. Ensminger, *Ultrasonics: fundamental, technology, and applications*, 2nd ed., New York: Marcel Dekker, 1988.

[110] G. S. Kino, "The application of reciprocity theory to the scattering of acoustic waves by flaws," *J. Appl. Phys.*, vol. 49, no. 6, pp. 3190-3199, 1978.

MICHIGAN STATE UNIV. LIBRARIES
31293008850921